AFRL-SN-WP-TR-2003-1174

SYNTHETIC APERTURE RADAR (SAR) AUTOMATIC TARGET RECOGNITION (ATR) PARAMETRIC STUDY

Kefu Xue, Ph.D.
Sam Sink

Wright State University
Department of Electrical Engineering
3640 Colonel Glenn Highway
Dayton, OH 45435

FEBRUARY 2003

Final Report for 01 September 2001 – 01 January 2003

STINFO FINAL REPORT

SENSORS DIRECTORATE
AIR FORCE RESEARCH LABORATORY
AIR FORCE MATERIEL COMMAND
WRIGHT-PATTERSON AIR FORCE BASE, OH 45433-7320

NOTICE

USING GOVERNMENT DRAWINGS, SPECIFICATIONS, OR OTHER DATA INCLUDED IN THIS DOCUMENT FOR ANY PURPOSE OTHER THAN GOVERNMENT PROCUREMENT DOES NOT IN ANY WAY OBLIGATE THE U.S. GOVERNMENT. THE FACT THAT THE GOVERNMENT FORMULATED OR SUPPLIED THE DRAWINGS, SPECIFICATIONS, OR OTHER DATA DOES NOT LICENSE THE HOLDER OR ANY OTHER PERSON OR CORPORATION; OR CONVEY ANY RIGHTS OR PERMISSION TO MANUFACTURE, USE, OR SELL ANY PATENTED INVENTION THAT MAY RELATE TO THEM.

THIS REPORT HAS BEEN REVIEWED BY THE OFFICE OF PUBLIC AFFAIRS (ASC/PA) AND IS RELEASABLE TO THE NATIONAL TECHNICAL INFORMATION SERVICE (NTIS). AT NTIS, IT WILL BE AVAILABLE TO THE GENERAL PUBLIC, INCLUDING FOREIGN NATIONS.

THIS TECHNICAL REPORT HAS BEEN REVIEWED AND IS APPROVED FOR PUBLICATION.

/s/

JASON B. GREGGA, Capt
Project Engineer
ATR & Fusion Algorithms Branch
Sensor ATR Technology Division

/s/

DALE E. NELSON, Ph.D.
Chief, ATR & Fusion Algorithms Branch
Sensor ATR Technology Division
Sensors Directorate

/s/

DAVID W. CHANDLER
Lieutenant Colonel, USAF
Deputy, Sensor ATR Technology Division
Sensors Directorate

REPORT DOCUMENTATION PAGE

The public reporting burden for this collection of information is estimated to average 1 hour per response, including the time for reviewing instructions, searching existing data sources, searching existing data sources, gathering and maintaining the data needed, and completing and reviewing the collection of information. Send comments regarding this burden estimate or any other aspect of this collection of information, including suggestions for reducing this burden, to Department of Defense, Washington Headquarters Services, Directorate for Information Operations and Reports (0704-0188), 1215 Jefferson Davis Highway, Suite 1204, Arlington, VA 22202-4302. Respondents should be aware that notwithstanding any other provision of law, no person shall be subject to any penalty for failing to comply with a collection of information if it does not display a currently valid OMB control number. **PLEASE DO NOT RETURN YOUR FORM TO THE ABOVE ADDRESS**.

1. REPORT DATE *(DD-MM-YY)*	2. REPORT TYPE	3. DATES COVERED *(From - To)*
February 2003	Final	09/01/2001 – 01/01/2003

4. TITLE AND SUBTITLE
SYNTHETIC APERTURE RADAR (SAR) AUTOMATIC TARGET
RECOGNITION (ATR) PARAMETRIC STUDY

5a. CONTRACT NUMBER
F33615-01-C-1852

5b. GRANT NUMBER

5c. PROGRAM ELEMENT NUMBER
62204F

6. AUTHOR(S)
Kefu Xue, Ph.D.
Sam Sink

5d. PROJECT NUMBER
6095

5e. TASK NUMBER
04

5f. WORK UNIT NUMBER
06

7. PERFORMING ORGANIZATION NAME(S) AND ADDRESS(ES)

Wright State University
Department of Electrical Engineering
3640 Colonel Glenn Highway
Dayton, OH 45435

8. PERFORMING ORGANIZATION REPORT NUMBER

9. SPONSORING/MONITORING AGENCY NAME(S) AND ADDRESS(ES)

Sensors Directorate
Air Force Research Laboratory
Air Force Materiel Command
Wright-Patterson AFB, OH 45433-7320

10. SPONSORING/MONITORING AGENCY ACRONYM(S)
AFRL/SNAT

11. SPONSORING/MONITORING AGENCY REPORT NUMBER(S)
AFRL-SN-WP-TR-2003-1174

12. DISTRIBUTION/AVAILABILITY STATEMENT
Approved for public release; distribution is unlimited.

13. SUPPLEMENTARY NOTES

14. ABSTRACT

SAR ATR is a very complex problem that still has not been mastered. SAR ATR is difficult largely due to the fact that SAR imagery exhibits large variability. SAR imagery is a function of many variables called operating conditions (OCs) that can be subdivided into three large groups. The three main OCs are target, environment, and sensor. Sensor operating conditions deal with the properties of the sensor that have some of the largest effects on the formation of SAR images, including depression angle, squint angle, frequency, PRF, polarization, single/multi-look, sensor abnormalities, noise level, strip versus spot, and resolution. In the development and testing of SAR ATR algorithms to date the effects of sensor OCs have been given very little thought. The ultimate objective of this study is to develop a road map for studying various effects of varying sensor OCs on the performance of SAR ATR algorithms. For achieving this goal, we conducted literature searches to see how much had been done in sensor OC study. We also studied alternative data sources and the ways to generate SAR data related to the variation of sensor OCs to support SAR parametric study. In addition, we allocated and implemented a number of baseline ATR algorithms for the evaluation of their performance under the variation of sensor OCs. Our research has established an experimental paradigm for SAR parametric study.

15. SUBJECT TERMS
Synthetic Aperture Radar (SAR), Automatic Target Recognition (ATR), SAR parametric variations, Sensor Operating Conditions, ATR baseline algorithms

16. SECURITY CLASSIFICATION OF:			17. LIMITATION OF ABSTRACT:	18. NUMBER OF PAGES	19a. NAME OF RESPONSIBLE PERSON (Monitor)
a. REPORT Unclassified	**b. ABSTRACT** Unclassified	**c. THIS PAGE** Unclassified	SAR	110	Jason B. Gregga, Capt.
					19b. TELEPHONE NUMBER *(Include Area Code)* (937) 255-1115 x4386

TABLE OF CONTENTS

Chapter 1
Introduction

Synthetic Aperture Radar (SAR) has become an invaluable information resource for both military and civilian applications. The collection of SAR images by various platforms (e.g. Global Hawk, NASA/JPL AIRSAR, etc.) and various missions for multiple purposes (e.g. reconnaissance, terrain mapping, etc.) has lead to vast amount of data over wide surveillance areas . The pixel–to–eye ratio is simply too high for human analysts to rapidly sift through massive volumes of sensor data and yield engagement decisions quickly and precisely. Effective automatic target recognition (ATR) algorithms to process this growing mountain of information are clearly needed.

SAR ATR is a very complex problem that still has not been mastered. SAR ATR is difficult largely due to the fact that SAR imagery exhibits large variability. SAR imagery is a function of many variables called operating conditions (OC's) that can be subdivided into three large groups. The three main OC's are target, environmental, and sensor. Target operating conditions deal with the properties of the target that can effect the formation of the SAR image and includes but is not limited to configuration, articulation, different target classes, and level of damages. Environmental operating conditions deal with the properties of the environment that can effect the formation of the SAR image and includes but is not limited to layover, obstruction, background, adjacency, camouflage, clutters and weather. Sensor operating conditions deal with the properties of the sensor that can effect the formation of the SAR image and includes but is not limited to depression angle, polarization, frequency, and resolution. In the development and testing of SAR ATR algorithms to date the effects of target, and environmental OC's have been greatly explored.

In 1999, Timothy D. Ross wrote "Variability in SAR images due to sensing arrangement is no less important than that due to target or environmental variability. We have given this little though to date," and three years later little has changed [36] . SAR ATR algorithms generally use MSTAR data to train and test. Unfortunately MSTAR data typically represents only a single point in the sensor OC dimension. All the MSTAR data was collected using the same sensor having the same polarization, frequency, and resolution. The lack of variation among these parameters makes determining their effects on the performance of SAR ATR algorithms using MSTAR data alone impossible [36] . The cost and complication of collecting data with different sensor OCs seems to have kept any real progress in this area. Sensor OC's represent all of the ways that the properties of the radar sensor can affect the outcome of a SAR image. To completely characterize all of the properties of a sensor which has an effect on the outcome of a SAR image would be far too extensive for this one study. However the most important sensor properties can be characterized. The sensor parameters, which have some of the largest effects on the formation of the image, include depression angle, squint angle, frequency, PRF, polarization, single/multi-look, sensor abnormalities, noise level, and strip vs spot.

The ultimate objective of this study is to develop a road map for studying various effects of varying sensor OC's on the performance of SAR ATR algorithms. To achieve this goal,

we proposed first to conduct literature search to see how much had been done in sensor OC condition study. We also proposed to seek alternative sources or ways to generate SAR data related to variations of sensor OC's to support SAR parametric study in the future. In addition, we proposed to allocate and implement a number of baseline ATR algorithms for the evaluation of their performance under the variation of sensor OC's. In this document the results of our work are presented. After a brief introduction of SAR sensor parameters and their functions in various SAR image formation and enhancement algorithms, the results of a literature search done to understand the variations of sensor OC's in ATR performance are presented. Then the results of a literature search done to identity other potential sources of SAR data are presented. In order to establish a SAR parametric study paradigm, we have reviewed a number of ATR algorithms and implemented three baseline ATR algorithms for this purpose. We have also summarized our initial work in using Xpatch to generate SAR data with various sensor OC's. Finally a preliminary experiment is presented that shows the effects of the variation of a selected sensor OC (depression angle) on various SAR ATR baseline algorithms. Our research has also established an experimental paradigm for SAR parametric study.

Chapter 2
SAR Parametric Study Literature Review

The literature search on the SAR ATR and parametric studies covers past fifteen years. This chapter of the report will present the review of the literature search conducted to study sensor OC's and SAR ATR. The simple goal of this research is to understand how the variation of sensor OC's effect SAR ATR algorithms by studying public released research. The literature search in this area turned out to provide little understanding of how variation of sensor OC's affected the performance of SAR ATR algorithms. What little unclassified literature there was on sensor OC's seem to mostly deal with the general problem of how sensor parameter variation effected the formation of SAR imagery. Since almost all SAR ATR algorithms use either the image directly, or features generated from the image, the study of how sensor parameters affect the SAR image should provide valuable insight into the problem. In order to explain all the research papers and their implications on SAR parametric study, we will first briefly review the SAR imaging principle and methods. This brief review serves two purposes one is to let reader know where each sensor parameter fits in SAR image processing and the other is to introduce and unify the various sensor notations that will appear in the rest of the documentation. After the brief review, the research works that address the variations and effects of sensor parameters over SAR images will be explained.

2.1   SAR Image Principle and Processing — a Brief

One of the most important attributes of a radar system is its ability to resolve objects. The determining factor in the resolution of objects in a classical system is the length of the viewing aperture. The method of Synthetic aperture radar is a technique of creating a large aperture by using a very small physical radar and moving it in a straight path taking measurements in every position. How much of the synthetic aperture is used when imaging a scene turns out to be an important sensor parameter. The synthetic aperture can be constructed by either using the entire synthetic aperture to image a small target scene by steering the radar called spotlighting or use the synthetic aperture to image a target scene whose length is about the same as the length of the synthetic aperture called strip map. The spotlight SAR image using the entire synthetic aperture length to image the relatively small target area produces extremely high resolution, compared to strip map SAR. In order to understand the effects of Spot and Strip SAR, the mathematical models representing these respective processes must be developed. The mathematical models that will be developed in the following sections for Spot and Strip map SAR is basically a summation of the basic concepts covered in the book "Synthetic Aperture Radar: Signal Processing with MATLAB Algorithms" [44] .

The mathematical model describing Spotlight SAR will be developed first. The development will go through range imaging, cross range imaging, and finally through the 2-D SAR imaging for the Spotlight case. The general concept of range imaging of an object

is based on the idea of echo location. Echo location is based on the fact if a wave of energy (microwave or sound) is directed towards a series of objects, the objects will tend to reflect back some of that energy towards the sender. The larger objects will tend to reflect back more energy than smaller objects, this property is known as the targets reflectivity, which can also be refereed to as the radar cross section. The reflected waves from the objects further away will take a longer time to reach the receiver than the reflected waves from the closer objects. This property can be used to generate the distance from the target to the radar, which is also called the target range.

2.1.1   Range Imaging

In order to develop all of the mathematical equations for range imaging, we need to develop a model for the system. Suppose we have a set of N targets that are all at the same fixed cross range, but at different ranges. The cross range will be denoted as the variable y and will be parallel to the flight path of the plane. The range will be denoted as the variable x and will be perpendicular to the flight path of the plane. The radar cross section (RCS) for each object will be denoted by the reflectivity variable σ.

The radar will be considered to be at a position fixed such that the boresight of the radar is at the same cross range of the objects. The area of the range domain that the radar illuminates is called the **Radar Swath**. The center of the radar swath is designated by X_c, which can be determined by the center of mass of the target area,

$$X_c = \frac{\sum_n x_n |\sigma_n|^2}{\sum_n |\sigma_n|^2} \tag{2.1}$$

where x_n and σ_n are the position and radar cross section for the nth scatter respectively. The support band of the radar swath is given by $x_n \in [X_c - X_o, \quad X_c + X_o]$. The Radar swath is dictated by the radiation pattern of the individual radar with a target area size of $2X_o$. Using the model above and considering a radar with infinite bandwidth, the ideal target function can now be constructed as

$$f_0(x) = \sum_n \sigma_n \delta(x - x_n) \tag{2.2}$$

where $x = \frac{ct}{2}$ is a linear transform of time (c is wave propagation speed 3×10^8 m/s). Notice that $f_0(\frac{ct}{2})$ has infinitely fine range resolution.

Now lets develop range imaging through the idea of radar frequency variation. First we illuminate the one-dimensional target area with a radar pulse represented by $p(t)$. The echo signal received by the radar can be represented by the function

$$s(t) = \sum_n \sigma_n p(t - \frac{2x_n}{c}) \tag{2.3}$$

where $\frac{2x_n}{c}$ is the amount of time for the radar pulse to travel out to the nth target and back.

Using the fact that we can represent the echoed signal as

$$s(t) = f_0(\frac{ct}{2}) * p(t) \tag{2.4}$$

where $*$ denotes linear convolution.

This is truly a simplified model of the radar problem. The true physics characterizing the scattering of the electromagnetic waves that occur when an object is encountered may point out that this model is useless. It turns out that errors like quantization noise, thermal additive noise, and multiplication noise are larger sources of error.

There are several ways to reconstruct the target function from the received echo signal. The preferred reconstruction method is based on the idea of matched filtering. Match filtering is based on the idea of correlating the received echo with the complex conjugate of the initial transmitted radar pulse. This process is represented by

$$
\begin{aligned}
s_M(t) &= F^{-1}\{S(\omega) \cdot P^*(\omega)\} = s(t) * p^*(-t) \\
&= F^{-1}\{\sum_n \sigma_n P(\omega) \exp(-j\omega\frac{2x_n}{c}) \cdot P^*(\omega)\} \\
&= \sum_n \sigma_n F^{-1}\{|P(\omega)|^2 \exp(-j\omega\frac{2x_n}{c})\} \\
&= \sum_n \sigma_n p_{sf}(t - \frac{2x_n}{c}) = f_0(\frac{ct}{2}) * p_{sf}(t).
\end{aligned}
\tag{2.5}
$$

The point spread function

$$p_{sf}(t - \frac{2x_n}{c}) = F^{-1}\{|P(\omega)|^2 \exp(-j\omega\frac{2x_n}{c})\} \tag{2.6}$$

is dependent on the spectral shape of the transmitted radar signal $P(\omega)$. The convention is to let the power spectrum of a radar pulse $|P(\omega)|^2 = 1$ within its finite region of support given by $\omega \in (\omega_c - \omega_0, \omega_c + \omega_0)$ where ω_c denotes the carrier radian frequency and $2\omega_0$ is the bandwidth. Using these conditions the point-spread function can be represented as

$$
\begin{aligned}
p_{sf}(t) &= F^{-1}\{|P(\omega)|^2\}, \quad \omega \in (\omega_c - \omega_0, \omega_c + \omega_0) \\
&= \frac{\omega_0}{\pi} \operatorname{sin c}(\frac{\omega_0}{\pi}t) \exp(j\omega_c t)
\end{aligned}
\tag{2.7}
$$

where $\operatorname{sinc}(x) = \frac{\sin(\pi x)}{\pi x}$. This means the received echo is simply a delayed scaled version of the transmitted radar signal which is dependent on the position of the target from the radar and the target's range radar cross section with some spreading due to sinc function.

The received echo signal is a band pass signal that is usually converted into a low pass signal before match filtering. This process is known as base band conversion which can be represented as

$$s_b(t) = s(t) \exp(-j\omega_c t) \tag{2.8}$$

5

which gives the final base band matched filtered signal as

$$s_{Mb}(t) = s_b(t) * s_{0b}^*(-t)$$

where $s_{0b}(t) = p(t - \frac{2X_c}{c}) \exp(-j\omega_c t)$ is the base band version of radar pulse function $p(t)$ which is shifted to the right by a time distance corresponding to the center of radar swath X_c. In this way, the correlation peak at $t = 0$ is referred to $x = X_c$. The process of matched filtering is often done in the Fourier domain.

$$
\begin{aligned}
s_{Mb}(t) &= F^{-1}\{S_b(\omega) \cdot S_{0b}^*(\omega)\} \qquad\qquad (2.9)\\
&= \sum_n \sigma_n F^{-1}\{P(\omega + \omega_c) \exp(-j(\omega + \omega_c)\frac{2x_n}{c}) \cdot \\
&\qquad P^*(\omega + \omega_c) \exp(j(\omega + \omega_c)\frac{2X_c}{c})\}\\
&= \sum_n \sigma_n F^{-1}\{|P(\omega + \omega_c)|^2 \exp(-j(\omega + \omega_c)\frac{2(x_n - X_c)}{c}\}\\
&= \sum_n \sigma_n \cdot p_{sf}(t - \frac{2(x_n - X_c)}{c})
\end{aligned}
$$

where the point-spread function is found by using the same convention, $|P(\omega)|^2 = 1$ with $\omega \in (\omega_c - \omega_0, \omega_c + \omega_0)$. Only difference is that $P(\omega + \omega_c)$ is a base band signal now, that is

$$
\begin{aligned}
p_{sf}(t) &= F^{-1}\{|P(\omega)|^2\}, \quad \omega \in (-\omega_0, \omega_0) \qquad\qquad (2.10)\\
&= \frac{\omega_0}{\pi} \sin c(\frac{\omega_0}{\pi} t).
\end{aligned}
$$

The matched filtering signal

$$s_{Mb}(t) = \sum_n \sigma_n \cdot \frac{\omega_0}{\pi} \sin c(\frac{\omega_0}{\pi}(t - \frac{2(x_n - X_c)}{c})) \qquad\qquad (2.11)$$

simply shows a sinc–like blip at the location of a reflector with an amplitude proportional to its RCS and bandwidth of the radar pulse. For example, if we place one unit reflector at $x_1 = Xc - X_0$ and another one at $x_2 = Xc$, the reconstructed matched filtering signal will be

$$S_{Mb} = \frac{\omega_0}{\pi}[\sin c(\frac{\omega_0}{\pi}(t + \frac{2X_0}{c})) + \sin c(\frac{\omega_0}{\pi}t)]. \qquad\qquad (2.12)$$

It shows two sinc-like blip at $t = -\frac{2X_0}{c}$ and $t = 0$ (center of radar swath) respectively. The range resolution is determined by the spread of the point–spread function. Under the same assumption that the power spectrum of radar pulse function $|P(\omega)|^2 = 1$ within its $2\omega_0$ bandwidth, the resolution can be approximated by one half of the main lobe width of the sinc

function, that is the location of the first zero crossing at

$$\frac{\omega_0}{\pi}\frac{2\Delta x}{c} = 1, \text{ i.e. } \Delta x = \frac{c}{2}\frac{\pi}{\omega_0} = \frac{c}{4B_0} \tag{2.13}$$

where B_0 is the bandwidth of the base band radar pulse $p(t)$ in Hz. For a digital radar system, the return radar signal must be sampled with a sampling interval Δt. According to the sampling theory,

$$\Delta t < \frac{1}{2B_0}. \tag{2.14}$$

In reality, B_0 may be just a –3dB cutoff frequency for the radar signal. The actual sampling interval should be much finer to guard against the alaising error. The sampled radar return signal in range unit is called discrete range bins.

$$x_i = \frac{c \cdot t_i}{2} = X_c + (i - \frac{N}{2} - 1)\frac{c \cdot \Delta t}{2}; \text{ for } i = 1, 2, \cdots, N \tag{2.15}$$

where $t_i = T_s + (i - 1) \cdot \Delta t$ is the sample locations in time unit. T_s is the starting sampling time corresponding to the closest location $X_c - X_o$ in the radar swath. For $i = 1$ and $i = N$, it yields

$$x_1 = X_c - \frac{N}{2} \cdot \frac{c \cdot \Delta t}{2} \leq X_c - X_0 \text{ and } x_N = X_c + (\frac{N}{2} - 1) \cdot \frac{c \cdot \Delta t}{2} \geq X_c + X_0 \tag{2.16}$$

respectively. The N samples cover the entire support band of the radar swath $[X_c - X_0, \quad X_c + X_o]$.

There is one draw back with the radar pulse given above. The traditional radar pulse is a direct trade off between power and resolution. If the resolution is increased the power of the radar pulse is decreased and vice versa. In order to get around this difficulty, a linear frequency modulated (LFM) chirp radar pulse is used.

$$p(t) = a(t)\exp(j(\beta t + \alpha t^2)) \tag{2.17}$$

where

$$a(t) = \begin{cases} 1 & \text{for } 0 \leq t \leq T_p \\ 0 & \text{otherwise} \end{cases}.$$

The chirp pulse for the radar signal behaves the same as any other chirp signal. The instantaneous frequency of the chirp pulse is given by

$$\omega(t) = \frac{d}{dt}(\beta t + \alpha t^2) = \beta + 2\alpha t \tag{2.18}$$

where the frequency upsweeps ($\alpha > 0$) from β to $\beta + 2\alpha T_p$ (rad./sec.). The bandwidth of the chirp radar pulse is equal to $2\alpha T_p$. In this case, the carrier frequency of the chirp radar is

considered to be the mid–frequency

$$\omega_c = \beta + \alpha T_p \tag{2.19}$$

and the bandwidth of the base band signal is then $\pm \alpha T_p$. Therefore the Nyquist sampling interval for the chirp radar return signal is $\Delta t \leq \frac{\pi}{\alpha T_p}$. Using the chirp model for the radar signal, the received echo signal (equation 2.3) becomes

$$
\begin{aligned}
s(t) &= \sum_n \sigma_n a(t - \frac{2x_n}{c}) \exp(j(\beta(t - \frac{2x_n}{c}) + \alpha(t - \frac{2x_n}{c})^2)) \\
&= \sum_n \sigma_n a(t - t_n) \exp(j\beta(t - t_n)) \exp(j(\alpha t^2 - 2t_n \alpha t + \alpha t_n{}^2))
\end{aligned}
$$

where $t_n = \frac{2x_n}{c}$.

The reconstruction of objects from a received echo signal using a transmitted chirp signal is done by a process known as pulse compression. Pulse compression is done by using the complex conjugate of the received signal with the phase of the transmitted chirp signal.

$$
\begin{aligned}
s_c(t) &= s^*(t) \cdot \exp(j(\beta t + \alpha t^2)) \tag{2.20} \\
&= \sum_n \sigma_n a^*(t - t_n) \exp(j\beta t_n) \exp(j(2t_n \alpha t - \alpha t_n{}^2)) \\
&= \sum_n \sigma_n a^*(t - t_n) \exp(j(\beta t_n - \alpha t_n{}^2)) \exp(j2t_n \alpha t).
\end{aligned}
$$

The compressed pulse $s_c(t)$ contains three parts for each reflector: a) $\sigma_n a^*(t - t_n)$ is the amplitude of the echo from the nth reflector; b) $\exp(j(\beta t_n - \alpha t_n{}^2))$ is a constant phase delay caused by n^{th} reflector in a second order function; c) $\exp(j2t_n \alpha t)$ is a sinusoid with a frequency proportional to the location of nth reflector. The echoes can be detected by taking the Fourier Transform of the compressed signal $s_c(t)$.

$$S_c(\omega) = \sum_n \sigma_n P_{sf}(\omega - 2t_n\alpha) \exp(j(\beta t_n - \alpha t_n{}^2 - \omega t_n)) \tag{2.21}$$

where

$$P_{sf}(\omega) = F\{a^*(t)\} = T_p \operatorname{sin c}(\frac{\omega T_p}{2\pi}) \tag{2.22}$$

is the point spread function in the frequency domain and T_p is the duration of the chirp pulse in the time domain. For a rectangular pulse function $a(t)$, we can detect the reflect locations from the sinc-like blip at $\omega = \frac{4\alpha x_n}{c}$ in the Fourier spectrum

$$S_c(\omega) = \sum_n \sigma_n T_p \operatorname{sin c}((\omega - \frac{4\alpha x_n}{c})\frac{T_p}{2\pi}) \exp(j(\beta t_n - \alpha t_n{}^2 - \omega t_n)). \tag{2.23}$$

The range resolution for a chirp pulse is again decided by the first zero crossing of the sinc

function from $\omega = 0$

$$\frac{4\alpha\Delta x}{c}\frac{T_p}{2\pi} = 1, \text{ i.e. } \Delta x = \frac{\pi c}{2\alpha T_p} \tag{2.24}$$

in the range axis $x = \frac{c}{4\alpha}\omega$.

2.1.2   Cross Range Imaging

The basic concept behind cross range imaging is the idea of Doppler frequency shift. The concept of Doppler frequency shift can best be understood by an example. Suppose a single frequency pulse is transmitted to a unit reflector with no other clutter. When the echo returns back to the receiver the echoed signal has the same frequency as the transmitted signal. Now if we move the receiver towards the object, the received echo signal will appear to have a higher frequency than the transmitted pulse. If we move the receiver away from the object it will appear as the echoed signal has a lower frequency than the transmitted pulse. This is the concept of Doppler frequency shift. The cross range imaging that is presented here from a mathematical viewpoint is based on wavefront reconstruction. Wavefront reconstruction is the process of inverting the wave equation, which is the Fourier decomposition of a Green's Function. (Spherical phase function.)

In order to develop all of the mathematical equations for cross range imaging, again we need to develop a model for the system. Suppose we have a set of N targets with reflectivity $\sigma_n, \quad n = 1, 2, \cdots, N$ and located at (x_n, y_n) where $x_n \in [X_c - X_0, X_c + X_0]$ is the range value and $y_n \in [Y_c - Y_0, Y_c + Y_0]$ is the cross range value. The value Y_c is center of radar swath in the cross range domain. We assume that all the targets are at a fixed range, e.g. $x_n = X_c$, but at different cross ranges. The position of the radar will be specified by the coordinates $(0, u)$. The variable u, that is in the same direction as the cross range axis y, is called the **synthetic aperture domain** or **slow time domain**. If $Y_c = 0$, for any given radar cross range location u, the cross range value is symmetric to u, $y_n \in [-Y_0, +Y_0]$, which is referred to as the broadside SAR system. Otherwise, it is called a squint mode SAR system. The variable of time t will be called the fast time domain. The variation of u can also be expressed as the aspect angle. The aspect angle is the angle formed between the nth object and the radar at position $(0, u)$, which can be expressed as

$$\theta_n(u) = \arctan(\frac{y_n - u}{x_n}). \tag{2.25}$$

The mathematical model of the received echo can now be generated. Suppose the radar transmits a single frequency pulse

$$p(t) = \exp(j\omega t). \tag{2.26}$$

The distance between the radar at position u and the nth object at (x_n, y_n) is given by

9

$\sqrt{x_n^2 + (y_n - u)^2}$. Now the received echo can be represented as

$$
\begin{aligned}
s(t, u) &= \sum_n \sigma_n p \left(t - \frac{2\sqrt{x_n^2 + (y_n - u)^2}}{c} \right) \\
&= \exp(j\omega t) \sum_n \sigma_n \exp\left(-j2k\sqrt{x_n^2 + (y_n - u)^2} \right)
\end{aligned}
\tag{2.27}
$$

where $k = \frac{\omega}{c}$ (rad./m) is called the wavenumber. As before we can perform fast time base band conversion of the received signal to obtain

$$
\begin{aligned}
s(\omega, u) &= s(t, u) \exp(-j\omega t) \\
&= \sum_n \sigma_n \exp\left(-j2k\sqrt{x_n^2 + (y_n - u)^2} \right) \\
&= \sum_n s_n(\omega, u)
\end{aligned}
\tag{2.28}
$$

where

$$
s_n(\omega, u) = \sigma_n \exp\left(-j2k\sqrt{x_n^2 + (y_n - u)^2} \right)
\tag{2.29}
$$

is the base band echoed signal from each individual target. For a wide band signal $\omega \in [\omega_c - \omega_0, \omega_c + \omega_0]$, the Fourier transform of the base band converted radar echo signal (2.27) can be expressed as

$$
\begin{aligned}
s(\omega, u) &= \int_t s(t, u) \exp(-j\omega_c t) \exp(-j\omega t) dt \\
&= P(\omega - \omega_c) \sum_n \sigma_n \exp\left(-j2k\sqrt{x_n^2 + (y_n - u)^2} \right)
\end{aligned}
\tag{2.30}
$$

or simply

$$
s(\omega, u) = P(\omega) \sum_n \sigma_n \exp\left(-j2k\sqrt{x_n^2 + (y_n - u)^2} \right)
\tag{2.31}
$$

where $P(\omega)$ is the lowpass base band spectrum of the radar pulse. This expression will be used later on when we discuss SAR image algorithms. The reference signal used for matched filtering is only one unit reflector placed at the center of the broadside target area, which is given by the coordinates $(x_n, y_n) = (X_c, 0)$. The base band reference signal can be expressed as

$$
s_0(\omega, u) = \exp\left(-j2k\sqrt{X_c^2 + u^2} \right).
\tag{2.32}
$$

The phase function $\exp\left(-j2k\sqrt{x_n^2 + (y_n - u)^2} \right)$ in equation (2.29) means that the signal $s_n(\omega, u)$ is a phase modulated (PM) signal or also known as a spherical PM signal. Now take

the slow–time Fourier transform of the spherical PM signal with respect to $u \in (-\infty, \infty)$

$$
\begin{aligned}
S_n(\omega, k_u) &= \int_{-\infty}^{\infty} s_n(\omega, u) \exp(-jk_u u) du \qquad (2.33) \\
&= \sigma_n \int_{-\infty}^{\infty} \exp\left(-j2k\sqrt{x_n^2 + (y_n - u)^2} - jk_u u\right) du
\end{aligned}
$$

where k_u (rad./m) represents the spatial frequency domain of the u (m) domain and is also referred to as the **slow-time frequency** or **Doppler domain** (The unit for k_u is frequency (rad./sec) over speed (m/sec.)). This integral can now be evaluated using the method of stationary phase. The evaluation of the integral gives the expression

$$
S_n(\omega, k_u) = \sigma_n \frac{\exp(-j\frac{\pi}{4})}{\sqrt{4k^2 - k_u^2}} \exp\left(-j\sqrt{4k^2 - k_u^2} \cdot x_n - jk_u \cdot y_n\right) \qquad (2.34)
$$

for $k_u \in [-2k, 2k]$ and zero otherwise. $S_n(\omega, k_u)$ has a finite support band width in k_u. In this signal, the term $\frac{\exp(-j\frac{\pi}{4})}{\sqrt{4k^2 - k_u^2}}$ is just a slowly fluctuating amplitude and the phase term gives far more importance in cross-range imaging analysis. We can approximate the term as

$$
S_n(\omega, k_u) = \sigma_n \exp\left(-j\left[\sqrt{4k^2 - k_u^2} \cdot x_n + k_u \cdot y_n\right]\right) \qquad (2.35)
$$

where the phase is a linear function of x_n and y_n as the contrast to a nonlinear function in $s_n(\omega, u)$.

The above derivation is only for an infinite aperture synthetic radar, which in practical applications is impossible. Now lets look at a practical situation where the length of the synthetic aperture is equal to $2L$. This means u can also be expressed as $u \in [-L, L]$. The slow–time Fourier transform becomes

$$
S_n(\omega, k_u) = \int_{-L}^{L} s_n(\omega, u) \exp(-jk_u u) du. \qquad (2.36)
$$

Again the evaluation of the integration yield the same simplified echo signal in the k_u domain (equation 2.35). The only difference is that the finite support band width becomes

$$
\begin{aligned}
k_u &\in [K_{un}(L), K_{un}(-L)] \qquad (2.37) \\
&= [2k\sin(\theta_n(L)), 2k\sin(\theta_n(-L))]
\end{aligned}
$$

where $K_{un}(u)$ is the instantaneous frequency of the PM signal $s_n(\omega, u)$ (2.29) in the u domain. It can be found by

$$
\begin{aligned}
K_{un}(u) &= \frac{\partial}{\partial u}\left(-2k\sqrt{x_n^2 + (y_n - u)^2}\right) \qquad (2.38) \\
&= \frac{2k(y_n - u)}{\sqrt{x_n^2 + (y_n - u)^2}} = 2k\sin(\theta_n(u))
\end{aligned}
$$

11

where $\theta_n(u)$ shown in equation (2.25) is once again the aspect angle of the radar to the nth target. The value of

$$\Omega_n = [2k\sin(\theta_n(L)), 2k\sin(\theta_n(-L))] \tag{2.39}$$

denotes the slow–time Doppler support band of $S_n(\omega, k_u)$ for n^{th} target.

Now let us consider a couple oberservations.. Case 1: if a unit reflector is placed at $(x_n, y_n = 0)$ which is considered a strict boresight target (also $\theta_n(0) = 0$), then the center of the band should be located at $(u = 0)$

$$\Omega_{nc} = K_{un}(0) = 0. \tag{2.40}$$

The band width of $S_n(\omega, k_u)$ in this case is the largest equal to

$$\begin{aligned}\Omega_n &= [2k\sin(\arctan(\frac{-L}{x_n})), 2k\sin(\arctan(\frac{L}{x_n}))] \\ &\approx [-\frac{2kL}{x_n}, \frac{2kL}{x_n}]\end{aligned} \tag{2.41}$$

where L is generally much smaller than x_n. Case 2: for the off boresight or squint targets ($y_n \neq 0$, that is, $\theta_n(0) \neq 0$), the carrier Doppler frequency (also known as the phase center of PM signals) should be

$$\Omega_{nc} \approx K_{un}(0) = 2k\sin(\theta_n(0)) \tag{2.42}$$

and the band width should be approximately

$$|\Omega_n| \approx \frac{4kL}{x_n}\cos^2(\theta_n(0)). \tag{2.43}$$

We can see when $\theta_n(0) = \frac{\pi}{2}$, that is, the target is located at $(x_n, y_n = \infty)$, the band width of $S_n(\omega, k_u)$ for the target is zero. The radar can not see the target. Therefore, for finite aperture SAR, it works best for the targets at or near boresight. The band width of Doppler support band of the squint targets are narrower than those of the boresight targets. It is crucial to recognize that the SAR signal is a bandpass signal centered at $2k\sin(\theta_n(0))$.

The reconstruction of the target function from the received signal is done using the method of matched filtering which is the same method used in the range imaging case. The received echo can now be expressed as

$$\begin{aligned}S(\omega, k_u) &= \sum_n S_n(\omega, k_u) \\ &= \sum_n \sigma_n I_n(\omega, k_u)\exp\left(-j(\sqrt{4k^2 - k_u^2}\cdot x_n + k_u\cdot y_n)\right)\end{aligned} \tag{2.44}$$

where $I_n(\omega, k_u)$ indicates the band width of the slow–time Doppler support band of nth

12

target

$$I_n(\omega, k_u) = \begin{cases} 1 & \text{for } k_u \in \Omega_n = [2k\sin(\theta_n(L)), 2k\sin(\theta_n(-L))] \\ 0 & \text{otherwise} \end{cases} . \qquad (2.45)$$

Same as in equation (2.32), the reference signal for match filtering in Doppler frequency k_u can be found by placing a unit reflector at the center of the broad side of the radar, that is $(x_n, y_n) = (X_c, 0)$. From equation (2.35), it yields

$$S_0(\omega, k_u) = \exp\left(-j\sqrt{4k^2 - k_u^2} \cdot X_c\right) \quad \text{for } k_u \in [-2k, 2k]. \qquad (2.46)$$

To examine the cross range image of the targets, we only pick the targets located at a common range value, say $x_n = X_c$ for $n = 1, 2, \cdots$. The target function, which describes the locations of the targets in the scene, can now be expressed by

$$\begin{aligned} F(k_u) &= S(\omega, k_u) \cdot S_0^*(\omega, k_u) \qquad\qquad\qquad (2.47) \\ &= \exp(-j\sqrt{4k^2 - k_u^2} \cdot X_c) \sum_n \sigma_n I_n(\omega, k_u) \exp\left(-jk_u \cdot y_n\right) \\ &\quad \cdot \exp\left(j\sqrt{4k^2 - k_u^2} \cdot X_c\right) \\ &= \sum_n \sigma_n I_n(\omega, k_u) \exp\left(-jk_u \cdot y_n\right) \end{aligned}$$

which is the same as the match filtering

$$f(y) = s(\omega, u) * s_0^*(\omega, -u)$$

in u domain. The cross range distance y which is in the same domain of u. Now taking the inverse Fourier Transform the equation $F(k_u)$ gives

$$\begin{aligned} f(y) &= \sum_n \sigma_n \cdot F^{-1}\left\{I_n(\omega, k_u) \exp\left(-jk_u \cdot y_n\right)\right\} \\ &= \sum_n \sigma_n \cdot i_n(\omega, y - y_n) \end{aligned}$$

where $i_n(\omega, y)$ is the point spread function for n^{th} target in cross range u. Since $I_n(\omega, k_u)$ is a brick function with width equal to $|\Omega_n|$ in (2.43) and is centered approximately at Ω_{nc} in (2.42),

$$i_n(\omega, y) = \frac{|\Omega_n|}{2\pi} \sin c(\frac{|\Omega_n|}{2\pi} y) \exp(j\Omega_{nc} y). \qquad (2.48)$$

The point spread function for the cross range is dependent on the slow time Doppler frequency bandwidth of the system. The magnitude of the target function can now be

13

expressed as

$$|f(y)| = \sum_n \sigma_n \frac{|\Omega_n|}{2\pi} |\sin c(\frac{|\Omega_n|}{2\pi} y)|. \tag{2.49}$$

The cross range resolution of the SAR can be again measured by the location of first zero crossing (one half of the main lobe) of the sinc function

$$\frac{|\Omega_n|}{2} \Delta_{y_n} = \pi. \tag{2.50}$$

It yields

$$\Delta_{y_n} = \frac{2\pi}{|\Omega_n|} \approx \frac{\lambda \cdot x_n}{4L \cos^2(\theta_n(0))} \tag{2.51}$$

following equation (2.43) and $k = \frac{\omega}{c} = \frac{2\pi}{\lambda}$. The resolution obtained in real systems never approaches this value, so it is customary to multiply this value by a fudge factor between 1 and 2. Comparing with the classical Rayleigh cross range resolution for a finite aperture radar $\frac{R\lambda}{D}$ where R is the range x_n; D is the radar aperture $2L$; and effective wavelength λ is $\frac{\lambda}{2}$ due to the round–trip propagation, Δ_{y_n} will be the same as the Rayleigh resolution for boresight targets ($\theta_n(0) = 0$).

2.1.3   SAR Radiation Pattern

The mathematical models generated so far only take into account the effects of the objects in the imaging scene on the electromagnetic waves of the radar. This is too simplistic for any practical application of radar theory. Any mathematical model to be accurate must take into account the effect of the input/output of the transmitter, the medium with which the electromagnetic waves are propagating through, and the noise effects of the receiver. All three of these effects can be modeled using one linear transfer function called the channel transfer function. The SAR radiation pattern is a measure that identifies the channel effect. To greatly simplify the following discussion, the radar will assumed to be stable (no variation in the radar radiation pattern) and all of the targets in the scene are homogenous.

The first effect to be modeled is the properties of the radiation pattern in the spatial and Fourier domains of the physical antenna itself. First assume that the radar antenna is at a fixed position $(0, u)$. Next assume the antenna absorbs and transmits microwave energy via its surface. The radar transmits a pulse given by

$$p(t) = \exp(j\omega t). \tag{2.52}$$

Now let S represent the contour that defines the surface of the antenna. So to begin modeling, we will assume the physical antenna is centered at a location $(0, u)$ and composed of very small differential elements located at

$$[x_e(l), u + y_e(l)], \quad l \in S. \tag{2.53}$$

14

An arbitrary point in the spatial domain (x, y) will experience radiation from a differential element $[x_e(l), y_e(l)]$ of antenna in transmit mode equal to

$$
\frac{i(l)}{\sqrt{x^2 + y^2}} p \left(t - \frac{\sqrt{[x - x_e(l)]^2 + [y - (u + y_e(l))]^2}}{c} \right) dl \qquad (2.54)
$$

$$
= \frac{i(l)}{r} \exp(j\omega t) \exp(-jk\sqrt{[x - x_e(l)]^2 + [y - u - y_e(l)]^2}) dl
$$

where $r = \sqrt{x^2 + y^2}$ and $i(l)$ is the amplitude function that represents the transmitting strength of that element. This is determined by the antenna manufacturer. The total radiation a point in space will receive from the antenna is simply the sum of all of the elements making up the antenna

$$
h_T(\omega, x, y - u) = \frac{1}{r} \int_{l \in S} i(l) \exp(-jk\sqrt{[x - x_e(l)]^2 + [y - u - y_e(l)]^2}) dl \qquad (2.55)
$$

where $\exp(j\omega t)$ is removed via base band conversion. Note that the phase part of the signal on the right of the equation

$$
\exp(-jk\sqrt{[x - x_e(l)]^2 + [y - u - y_e(l)]^2}) \qquad (2.56)
$$

is a spherical PM signal. Using the previous information on the evaluation of Fourier transform of spherical PM signals (2.29) and (2.35), its Fourier transform with respect to u in Doppler frequency domain k_u becomes

$$
\exp\left(-j \left[\sqrt{k^2 - k_u^2} \cdot (x - x_e(l)) + k_u(y - y_e(l)) \right] \right), \quad k_u \in [-k, k]. \qquad (2.57)
$$

Note the similarity between $y_n - u$ and $(y - y_e(l)) - u$ in equation (2.29) and equation (2.55) respectively. Equation (2.55) can be rewritten as

$$
\begin{aligned}
h_T(\omega, x, y - u) &= \frac{1}{r} \int_{l \in S} i(l) [\int_{-k}^{k} \exp(-j \cdot \\
&\quad \left[\sqrt{k^2 - k_u^2} \cdot (x - x_e(l)) + k_u(y - y_e(l)) \right]) \exp(jk_u u) dk_u] dl \\
&= \int_{-k}^{k} \exp\left(-j \left[\sqrt{k^2 - k_u^2} \cdot x + k_u y \right] \right) \qquad (2.58) \\
&\quad A_T(\omega, k_u) \exp(jk_u u) dk_u
\end{aligned}
$$

where

$$
A_T(\omega, k_u) = \frac{1}{r} \int_{l \in S} i(l) \exp\left(j \left[\sqrt{k^2 - k_u^2} \cdot x_e(l)) + k_u y_e(l) \right] \right) dl \qquad (2.59)
$$

is the radar transmitting amplitude pattern in the slow–time Doppler domain. The evaluation of $A_T(\omega, k_u)$ will depend on the physical attributes (S) of the individual radar and fast–time

frequency ω. From equation (2.58), we can get that the Fourier transform of $h_T(\omega, x, y - u)$ with respect to u is equal to

$$\exp\left(-j\left[\sqrt{k^2 - k_u^2} \cdot x + k_u y\right]\right) A_T(\omega, k_u). \tag{2.60}$$

Using inverse Fourier transform relationship in (2.29) and (2.35), we can have

$$h_T(\omega, x, y - u) = a_T(\omega, x, y - u)\exp\left(-jk\sqrt{x^2 + (y - u)^2}\right) \tag{2.61}$$

where $a_T(\omega, x, y - u)$ is the transmit mode radar radiation amplitude pattern.

The model of the electromagnetic radiation being received by a differential element on the radar from a spatial location (x, y) is the same as the previous model of the transmit. In fact for most radar systems the transmit mode is equal to the receive mode. For an active monostatic physical radar system located at $(0, u)$, the transmit–receive mode radiation pattern is simply the product of the transmit and receive modes

$$h(\omega, x, y - u) = h_T(\omega, x, y - u)h_R(\omega, x, y - u). \tag{2.62}$$

The Fourier Transform of $h(\omega, x, y - u)$ with respect to the slow–time u becomes

$$\exp\left(-j\left[\sqrt{k^2 - k_u^2} \cdot x + k_u y\right]\right) A_T(\omega, k_u) * \tag{2.63}$$
$$\exp\left(-j\left[\sqrt{k^2 - k_u^2} \cdot x + k_u y\right]\right) A_R(\omega, k_u).$$

The convolution becomes a PM signal dominated function and it can be approximated by the value at its phase center (when integrand $= \frac{k_u}{2}$)

$$A_T(\omega, \frac{k_u}{2})A_R(\omega, \frac{k_u}{2})\exp\left(-j\left[\sqrt{4k^2 - k_u^2} \cdot x + k_u y\right]\right). \tag{2.64}$$

In order for the model to be complete, we need to incorporate the effect the target has on the electromagnetic radiation. The coherent SAR. signature target amplitude pattern contains phase and magnitude. The amplitude pattern will vary with the radar pulse frequency and the aspect angle. The SAR radiation pattern for the nth target is given by

$$h_n(\omega, x_n, y_n - u) = h_T(\omega, x_n, y_n - u)a_n(\omega, x_n, y_n - u)h_R(\omega, x_n, y_n - u) \tag{2.65}$$

which is the combination of the effects of the radiation from radar to the target, the target, and radiation from target to radar. The frequency domain representation of the target amplitude function $a_n(\omega, x_n, y_n - u)$ is

$$A_n(2k\sin(\theta_n(u)), \omega) = A_n\left(\frac{2k(y_n - u)}{\sqrt{x_n^2 + (y_n - u)^2}}, \omega\right) \tag{2.66}$$

and it is a scalar function of the physical frequency of the radar and the instantaneous

16

frequency (2.38),

$$k_u = 2k\sin(\theta_n(u)) = \frac{2k(y_n - u)}{\sqrt{x_n^2 + (y_n - u)^2}}, \qquad (2.67)$$

where

$$\theta_n(u) = \arctan\left(\frac{y_n - u}{x_n}\right) \qquad (2.68)$$

is the aspect angle of the nth target with respect to the radar at $(0, u)$. Note that $A_n(\cdot)$ is not the Fourier transform of $a_n(\cdot)$, but a direct mapping of the radiation amplitude information

$$a_n(\omega, x_n, y_n - u) = \frac{1}{r}A_n(2k\sin(\theta_n(u)), \omega) \qquad (2.69)$$

in different scale, where the scale factor $\frac{1}{r}$ is often ignored for notation simplification. For example, in generic spot SAR, the amplitude of radiation pattern of a target at (x_n, y_n) in the synthetic aperture domain u is a rectangular window function

$$a_n(\omega, x_n, y_n - u) = \begin{cases} 1 & \text{for } |u| \leq L \\ 0 & \text{otherwise .} \end{cases} \qquad (2.70)$$

In the slow–time Doppler domain the amplitude function is

$$A_n(\omega, k_u) = \begin{cases} 1 & \text{for } k_u \in \Omega_n = [2k\sin(\theta_n(L)), 2k\sin(\theta_n(-L))] \\ 0 & \text{otherwise.} \end{cases} \qquad (2.71)$$

Therefore, in the Fourier transform domain, we have

$$A_T(\omega, \frac{k_u}{2})A_R(\omega, \frac{k_u}{2})A_n(\omega, k_u)\exp\left(-j\left[\sqrt{4k^2 - k_u^2} \cdot x + k_u y\right]\right) \qquad (2.72)$$

where

- $A_T(\omega, \frac{k_u}{2})A_R(\omega, \frac{k_u}{2})$ is the active radar amplitude pattern;
- $A_n(\omega, k_u)$ is the target amplitude pattern;
- $\exp\left(-j\left[\sqrt{4k^2 - k_u^2} \cdot x + k_u y\right]\right)$ is the phase history indicating target coordinates.

In the spatial domain, we have

$$a_T(\omega, x, y - u)a_R(\omega, x, y - u)a_n(\omega, x_n, y_n - u)\exp\left(-j2k\sqrt{x_n^2 + (y_n - u)^2}\right). \qquad (2.73)$$

The above derivation is done using the assumption that the transmitted and received electromagnetic radiation is a scalar quantity. Unfortunately the received electromagnetic radiation even from a scalar radar pulse will contain both vertical and horizontal components. Multiple polarization radar waves are also often used in the transmitted radar pulse to improve resolution. Fortunately polarized waves can be easily incorporated into our models. For example, let the radar at $(0, u)$ illuminates an arbitrary target at (x_n, y_n) with a polarized

vertical electromagnetic pulse. The amplitude function of the transmit mode of the radar can be represented as

$$a_T^V(\omega, x_n, y_n - u). \tag{2.74}$$

When the target is illumined by the vertically polarized wave, the target will reflect back electromagnetic radiation with both a vertical and a horizontal component. This can be model as one amplitude function which represents vertical mode scatting from a vertically polarized incident wave

$$a_n^{VV}(\omega, x_n, y_n - u) \tag{2.75}$$

and one amplitude function that represents horizontal mode scattering from a vertically polarized incident wave

$$a_n^{VH}(\omega, x_n, y_n - u). \tag{2.76}$$

When the radar is in receive mode, the antenna must record both the horizontal and vertical components of the electromagnetic radiation that can be modeled with the two types of amplitude functions

$$a_R^H(\omega, x_n, y_n - u) \text{ and } a_R^V(\omega, x_n, y_n - u). \tag{2.77}$$

For examples:

$$a_T^V(\omega, x, y - u) a_R^V(\omega, x, y - u) a_n^{VV}(\omega, x_n, y_n - u) \tag{2.78}$$

is the combined amplitude patterns for V mode transmission and V mode reception. And

$$a_T^V(\omega, x, y - u) a_R^H(\omega, x, y - u) a_n^{VH}(\omega, x_n, y_n - u) \tag{2.79}$$

is the combined amplitude patterns for V mode transmission and H mode reception.

2.1.4   The Generic Spot SAR Model

The purpose of this section is to bring together all the concepts covered so far in the previous sections to form a multidimensional (range x, cross–range y, altitude z) SAR image function that represents the targets in the scene. In the generic SAR imaging model, we will develop equations using slant range and cross range parameters (x_s, y)

$$x_s = \sqrt{x^2 + z^2} \tag{2.80}$$

where x is the range and z is the elevation of the aircraft. For the notation simplicity, we just use x for the slant range by considering that the slant plane is also a 2D plane for a fixed aircraft altitude. Again, we assume a collection on N targets randomly positioned and each target with a radar cross section given by σ_n. Each radar cross section will be modeled with an amplitude function, $a_n(\omega, x_n, y_n - u)$ which will vary with radar frequency, the target's relative range and the aspect angle.

The radar is assumed to be on an aircraft and its location will be given by $(0, u)$. The aircraft will also be assumed to be moving at a constant velocity, v_r, which allows the slow time domain to be represented by

$$\tau = \frac{u}{v_r}. \tag{2.81}$$

The pulse repetition interval (PRI) is defined as related to τ by PRI$= \Delta\tau$. This means the sample spacing in the u domain can be expressed by

$$\Delta u = \Delta\tau \cdot v_r = \text{PRI} \cdot v_r = \frac{v_r}{\text{PRF}} \tag{2.82}$$

where PRF stands for pulse repetition frequency.

The radar will illuminate the target area with a large-bandwidth signal $p(t)$. In this development, we consider a SAR system that keeps the same target area illuminated through out the scanning development. The targets in the area will be seen at all antenna locations , that is, $(-\infty < u < \infty)$. The radar radiation is assumed to be omnidirectional. The echoed signal received by the radar from the imaging scene can be represented by

$$s(t, u) = \sum_n \sigma_n p\left(t - \frac{2\sqrt{x_n^2 + (y_n - u)^2}}{c}\right). \tag{2.83}$$

There are two Fourier Transforms that can now be used for our benefit in the development of the rest of the equations. The first is the fast time (t) Fourier Transform of the received base band radar echo signal

$$
\begin{aligned}
s(\omega, u) &= \int_t s(t, u) \exp(-j\omega_c) \exp(-j\omega t) dt \tag{2.84}\\
&= P(\omega) \sum_n \sigma_n \exp\left(-j2k\sqrt{x_n^2 + (y_n - u)^2}\right)
\end{aligned}
$$

where $P(\omega)$ is the lowpass base band Fourier spectrum of the wide band radar signal $p(t)$ (2.31). This shows that the received signal is a linear combination of spherical PM signals and the only difference from equation (2.29) is the wide band radar pulse signal. The second is the Fourier transform with respect to the slow time domain u,

$$S(\omega, k_u) = P(\omega) \sum_n \sigma_n \exp\left(-j(\sqrt{4k^2 - k_u^2} \cdot x_n + k_u \cdot y_n)\right). \tag{2.85}$$

This equation is similar to the received echo in equation (2.44) with an exception of the wide band radar pulse signal.

In order to develop the rest of the equations, we have to define two new functions which are called the SAR spatial frequency transforms:

$$k_x(\omega, k_u) = \sqrt{4k^2 - k_u^2} \qquad \text{(rad./m)} \tag{2.86}$$

19

and

$$k_y(\omega, k_u) = k_u. \tag{2.87}$$

The echoed signal can now be expressed using the new functions as

$$S(\omega, k_u) = P(\omega) \sum_n \sigma_n \exp\left(-j[k_x(\omega, k_u)x_n + k_y(\omega, k_u)y_n]\right). \tag{2.88}$$

The ideal target function to represent the objects in the scene can be modeled by

$$f_0(x, y) = \sum_n \sigma_n \delta(x - x_n, y - y_n) \tag{2.89}$$

and its 2D Fourier transform to (k_x, k_y) domain

$$F_0(k_x, k_y) = \sum_n \sigma_n \exp(-j[k_x x_n + k_y y_n]). \tag{2.90}$$

The received signal can now be represented as

$$S(\omega, k_u) = P(\omega)F_0(k_x(\omega, k_u), k_y(\omega, k_u)). \tag{2.91}$$

There are several ways to reconstruct the target function (SAR imaging) from received echo signal. We will discuss three of the common SAR wavefront digital reconstruction algorithms developed in the late 1980's: fast–time matched filtering, range stacking and back projection.

The development presented so far does have a significant practical problem that must be solved before it can be used in practical SAR imaging algorithm. The problem arises from the fact that the mapping of the data from the (ω, k_u) domain to the (k_x, k_y) domain is nonlinear. This means after mapping received echo $S(\omega, k_u)$ to the (k_x, k_y) domain, the data for the function $F_0(k_x, k_y)$ is unevenly spaced, which will cause the object function $f_0(x, y)$ to be an inaccurate representation of the scene. We start with some assumptions that there are N samples in fast time $t_n = n\Delta t$ so as in its frequency domain

$$k_n = n\frac{\Delta\omega}{c} = n\frac{2\pi}{cN\Delta t} \tag{2.92}$$

and M synthetic aperture (slow–time) samplings of the SAR signal $S(\omega, u)$, which give a sampling internal Δu in the u domain. After the slow–time FFT of $S(\omega, u)$, there are M samples of $S(\omega, k_u)$ with the sampling interval $\frac{2\pi}{M\Delta u}$, that is

$$k_{um} = m\Delta k_u = m\frac{2\pi}{M\Delta u}. \tag{2.93}$$

Since $k_y(\omega, k_u) = k_u$ is a direct mapping, the discrete values of k_y are

$$k_{ynm} = k_{um}. \tag{2.94}$$

20

The discrete values of k_x are given by

$$k_{xnm} = \sqrt{4k_n^2 - k_{um}^2}. \tag{2.95}$$

The nonlinear transform and the rounding in the calculation cause uneven samples in k_{xnm} and errors in the locations of targets. But it can be corrected by interpolation.

2.1.4.1   Fast–time Matched Filtering – an interpolation based digital reconstruction method The reconstructed target function using matched filtering in Fourier transform domain can be expressed as

$$
\begin{aligned}
F(k_x(\omega, k_u), k_y(\omega, k_u)) &= S(\omega, k_u) P^*(\omega) \\
&= |P(\omega)|^2 \sum_n \sigma_n \exp\left(-j[k_x x_n + k_y y_n]\right)
\end{aligned} \tag{2.96}
$$

where $k_u \in [-2k, 2k]$ and $\omega \in [\omega_c - \omega_0, \omega_c + \omega_0]$. Before interpolation can be done, the function must under go the conversion from a bandpass signal to a lowpass signal

$$F_b(k_x(\omega, k_u), k_y(\omega, k_u)) = F(k_x, k_y) \exp(jk_x X_c) \tag{2.97}$$

by using the reference target function of a unit reflector at $(X_c, 0)$ for a broadside SAR system. Or

$$F_b(k_x(\omega, k_u), k_y(\omega, k_u)) = F(k_x, k_y) \exp(jk_x X_c + jk_u Y_c) \tag{2.98}$$

for the unit reflector at (X_c, Y_c) in a squint mode SAR. The conversion process will make the target function $f(x, y)$, that is inverse Fourier transform of $F_b(k_x, k_y)$, to be centered at the origin $(x, y) = (0, 0)$.

The interpolation is to create accurate samples of the function $F_b(k_x, k_y)$. Since only the variable k_x experienced a nonlinear transform (2.95), the interpolation is only performed over the k_x domain.

$$F_b(k_x, k_y) = \sum_{k_{xnm}} F_b(k_{xnm}, k_{ynm}) J_m(n, \Delta\omega) h(k_x - k_{xnm}) \tag{2.99}$$

where

$$
\begin{aligned}
J_m(n, \Delta\omega) &= \frac{dk_x(\omega, k_u)}{d\omega} = \frac{d\sqrt{4k^2 - k_u^2}}{d\omega} \\
&= \frac{4k}{c\sqrt{4k^2 - k_{um}^2}}
\end{aligned} \tag{2.100}
$$

is the Jacobian derivative of transformation from $k = \frac{\omega}{c}$ to k_x. The function $h(k_x - k_{xnm})$ is any cardinal functions that can be a windowed sinc function or a cubic B–spline function. For any given evenly spaced sample location $k_x = n\Delta k_x$ the function $F_b(k_x, k_y)$ is interpolated from the uneven spaced samples of $F_b(k_{xnm}, k_{ynm})$ where the sampling interval must

satisfy

$$\Delta k_x \leq \frac{\pi}{X_0} \qquad \text{(rad./m)}. \tag{2.101}$$

Since the length of the target area $(-X_0, X_0)$ is $2X_0$, then the resolution in Fourier domain, k_x, should be $\frac{2\pi}{2X_0}$. The target function can be reconstructed by using inverse FFT of the interpolated $F_b(k_x, k_y)$ with even spaced samples.

$$f(x, y) = \sum_n \sum_m F_b(n\Delta k_x, m\Delta k_y) \exp\left[j\left(xn\frac{2\pi}{N} + ym\frac{2\pi}{M}\right)\right] \tag{2.102}$$

where $\Delta k_y = \Delta k_u$.

In real implementation, the Jacobian function in the equation is often ignored due to its nature of slow fluctuation in the amplitude.

2.1.4.2   Range Stacking Equation (2.98) shows the result of fast time matched filtering and base band conversion with respect to the reference point $(x, y) = (X_c, Y_c)$. In theory, the target function can be recovered by 2–dimensional Fourier transform.

$$
\begin{aligned}
f(x, y) &= \int_{k_y} \int_{k_x} F_b(k_x, k_y) \exp(j[k_x \cdot x + k_y \cdot y]) dk_x dk_y \tag{2.103} \\
&= \int_{k_u} \int_{\omega} \left[S(\omega, k_u) P^*(\omega) \exp(j\sqrt{4k^2 - k_u^2} X_c + jk_u Y_c) \right] \tag{2.104} \\
&\quad \exp(j[\sqrt{4k^2 - k_u^2} \cdot x + k_u \cdot y]) J(\omega, k_u) d\omega dk_u
\end{aligned}
$$

where equation (2.104) is the map from (k_x, k_y) to (ω, k_u) for the expression (2.103). For the same reason, the amplitude function $J(\omega, k_u)$ can be ignored. At this time, let us only consider the target function at the reference range bin $x = x_i$. Equation (2.104) can be written as

$$
\begin{aligned}
f(x_i, y) &= \int_{k_u} \int_{\omega} \left[S(\omega, k_u) P^*(\omega) \exp(j\sqrt{4k^2 - k_u^2}(X_c + x_i) + jk_u Y_c) \right] \tag{2.105} \\
&\quad d\omega \exp(jk_u \cdot y) dk_u.
\end{aligned}
$$

In the above equation, the expression inside of the square brackets can be considered as the received signal $S(\omega, k_u)$ (2.85) being processed by a fast-time matched filter with a reference signal at the range bin x_i. The reference signal used in the matched filter can be found by placing a unit reflector at $(x, y) = (X_c + x_i, Y_c)$. From equation (2.85), the reference signal can be expressed as

$$S_{0i}(\omega, k_u) = P(\omega) \exp\left(-j(\sqrt{4k^2 - k_u^2} \cdot (X_c + x_i) + k_u \cdot Y_c)\right). \tag{2.106}$$

We now have the target function in the Fourier domain.

$$F_b(\omega, k_u) = S(\omega, k_u) S_{0i}^*(\omega, k_u). \tag{2.107}$$

Therefore, the target function for the reference range bin (x_i, y) can be expressed by

$$f(x_i, y) = \int_{k_u} \left[\int_\omega F_b(\omega, k_u) d\omega \right] \exp(jk_u \cdot y) dk_u \tag{2.108}$$

where the signal inside the square brackets is the integral (sum) of the fast-time matched filtering result over the fast time frequency at the range bin x_i. After that the target signal at one range bin, x_i, can be reconstructed by inverse Fourier transform with respect to k_u. There is also an alternative algorithm for Range stacking, where the integrations of ω and k_u are switched, but the results end up the same. However, the alternative algorithm is more computational intensive in practical implementation. After repeating the process (2.108) for $x_i \in (-X_0, X_0)$, we can put the target functions, $f(x_i, y)$, at all the range bins together to form a 2–dimensional SAR image. Since the actual implementation is all done in (ω, k_u) domain, there is no interpolation involved and thus there are no truncation errors either.

2.1.4.3   Back Projection In spot SAR mode, the radar antenna at all different locations $(0, u)$ sees target area. In order to form a SAR image, the energy reflected from the same target from different antenna locations must be coherently added together at the same image location. In the previous two sections, for the fast time matched filtering method, the coherent adding is realized by correlate received radar signal to a reference function of a unit reflector at $(0, 0)$ (scene center) for each antenna location $(0, u)$. In the range stacking method, the coherent adding is realized by correlate the received radar signal to a reference function of a unit reflector at range bins $(x_i, 0)$ (center of each range bin). Time Domain Correlation (TDC) reconstruction method is another reconstruction method based on the formation of the SAR image function by correlating received radar signal with a reference function of a unit reflector at the spatial points (x_i, y_j). That is

$$f(x_i, y_i) = \int_u \int_t s(t, u) p^* \left[t - \frac{2\sqrt{x_i^2 + (y_j - u)^2}}{c} \right] dt du \tag{2.109}$$

where $s(t, u)$ is the measured radar signal in the (t, u) domain as in equation (2.27). TDC reconstructing is basically a method that correlates the received SAR signal with each point (x_i, y_j) in the space of the target function. TDC is the measure of the reflectivity at each point in space. In equation (2.109), the term

$$\int_t s(t, u) p^* \left[t - \frac{2\sqrt{x_i^2 + (y_j - u)^2}}{c} \right] dt \tag{2.110}$$

can be considered to be the fast–time matched filtered signal

$$\begin{aligned} s_M(t, u) &= s(t.u) * p^*(-t) \\ &= \int_\tau s(\tau, u) p^*(t + \tau) d\tau \end{aligned} \tag{2.111}$$

at $t = -\frac{2\sqrt{x_i^2 + (y_j - u)^2}}{c}$. Equation (2.109) can be written as

$$f(x_i, y_j) = \int_u s_M \left(-\frac{2\sqrt{x_i^2 + (y_j - u)^2}}{c}, u \right) du. \qquad (2.112)$$

This is the equation known as the back projection SAR reconstruction. The target function $f(x, y)$ is reconstructed at each given grid point (x_i, y_j) by coherently adding up all the data from the matched filtering results in the fast time domains which correspond to the given point for all radar antenna locations, u.

2.1.5   The Spot SAR model — Practical Considerations

In the spot mode, the radar beam is steered towards the center of spotlighted target area (X_c, Y_c) as contrast to the assumption in the generic radar model there is no radar beam steering. Since the center is always on the broadside line at all slow–time radar location value u, the broadside angle for the radar location $(0, u)$ can be defined as

$$\theta_u = \tan^{-1}\left(\frac{Y_c - u}{X_c} \right) \qquad (2.113)$$

which varies as the antenna moves along the slow–time value u. If we create a scene center coordinate system by shifting and rotation, then we have

$$\begin{pmatrix} x_{\theta_u} \\ y_{\theta_u} \end{pmatrix} = \begin{pmatrix} \cos(\theta_u) & \sin(\theta_u) \\ -\sin(\theta_u) & \cos(\theta_u) \end{pmatrix} \begin{pmatrix} x - X_c \\ y - Y_c \end{pmatrix}. \qquad (2.114)$$

$(x_{\theta_u}, y_{\theta_u})$ coordinates vary with respect to the antenna location u. The change of the distance

$$R_c = \sqrt{X_c^2 + (Y_c - u)^2}, \qquad (Y_c - u) \le 2L$$

from the radar antenna to the scene center will cause the change of radar footprint $[-X_0, X_0]$ and $[-Y_0, Y_0]$. In practice, the radar footprint change is ignored due the fact that synthetic aperture length $2L$ in the cross range u is much smaller than the range in x where $(Y_c - u) = 2L$ only when the squint angle is zero. In the new scene centered coordinates $(x_{\theta_u}, y_{\theta_u})$, the target area is always in the broadside of the radar antenna. Similar to the equation (2.66), now we have the beam–steered radiation pattern amplitude function for a target location (x, y) inside the spotlighted target area

$$\begin{aligned} a(\omega, x, y, u) &\approx A\left(\frac{2k(y_{\theta_u} - 0)}{\sqrt{x_{\theta_u}^2 - (y_{\theta_u} - 0)^2}}, \omega \right) \qquad (2.115) \\ &= A\left(\frac{2k\left[(y - Y_c)\cos(\theta_u) - (x - X_c)\sin(\theta_u) \right]}{r}, \omega \right) \end{aligned}$$

where r is the distance from the antenna location to the target. Note the function is

24

$a(\omega, x, y, u)$ instead of $a(\omega, x, y - u)$, since y and u are now independent variables. The received fast–time Fourier transform of radar signal in the spotlighted area become

$$s(\omega, u) = P(\omega) \sum_n a_n(\omega, x, y - u) a(\omega, x, y, u) \tag{2.116}$$

$$\exp\left(-j2k\sqrt{x_n^2 + (y_n - u)^2}\right)$$

where $a_n(\cdot)$ is the amplitude pattern of nth target. In the slow–time Fourier transform domain, we have

$$S(\omega, k_u) = P(\omega) \sum_n A_n(\omega, k_u) A(\omega, k_u, x_n, y_n) I_n(\omega, k_u) \tag{2.117}$$

$$\exp\left[-j\left(\sqrt{4k^2 - k_u^2} \cdot x_n + k_u \cdot y_n\right)\right].$$

The difference from the generic spot SAR model is the spatial varying function $A(\omega, k_u, x_n, y_n)$ which will smear the target function and blur the image. It becomes worse when the phase variation of the radiation pattern amplitude function $A(\omega, k_u, x_n, y_n)$ is large. To remove the smearing effects, a shift varying filter (in slow–time domain u) $A^*(\omega, k_u, x_n, y_n)$ must be applied to remove the phase variations when $A(\omega, k_u, x_n, y_n)$ is not a real or of small phase variations. In the case that radar footprint $2X_0$, $2Y_0$ and synthetic aperture length $2L$ are much smaller than the radar range R_c, the shift varying filter can be approximated as follows using the invariant squint angle θ_c

$$A(\omega, k_u, x_n, y_n) \approx A\left(\frac{2k\left[(y - Y_c)\cos(\theta_c) - (x - X_c)\sin(\theta_c)\right]}{r}, \omega\right) \tag{2.118}$$

Furthermore, in narrow bandwidth spot SAR system, k can be approximated by the wavenumber $k_c = \frac{\omega_c}{c}$ at the carrier frequency.. The invariant filter (2.118) can be further simplified a weighting function (in slow–time domain u) according to the target location (x, y),

$$A(\omega, k_u, x_n, y_n) \approx A\left(\frac{2k_c\left[(y - Y_c)\cos(\theta_c) - (x - X_c)\sin(\theta_c)\right]}{r}, \omega\right). \tag{2.119}$$

2.1.6   The Stripmap SAR model

Although Spot and Stripmap SAR use many of the same concepts, stripmap SAR introduces constraints that must be taken into account before the SAR system can make maximum use of the information collected. The largest constraint for the Stripmap SAR is how to deal with each target being "visible" to only a small part of the synthetic aperture instead of the full aperture in the Spotlight case. The range coordinates of the SAR image will stay constant in the Stripmap SAR image, but the cross range coordinates will fluctuate. If we assume the radar radiation pattern which models the channel effect of a given radar (antenna, receiver,

propagation medium) is given by

$$h(\omega, x, y - u) = a\left(\omega, x, y - u\right)\exp\left(-j2k\sqrt{x^2 + (y - u)^2}\right) \qquad (2.120)$$

where all the values in the equation are the same as for the spotlight case. Now if we assume that the radar used has either a planar or hyperbolic shape, the radar pulse will expand from the radar into a cone shape. The half beam width B can be defined as

$$B = r\sin(\phi_d) \qquad (2.121)$$

with a far field approximation of

$$B = x\tan(\phi_d) \qquad (2.122)$$

where ϕ_d is the diverging angle, which is dependent on the geometrical shape of the radar or more precisely

$$\phi_d = \begin{cases} \arcsin\left(\frac{\lambda}{D_y}\right) & \text{for a Plannr radar} \\ \arctan\left(\frac{D_y}{2X_f}\right) & \text{for a Hyperbolic radar} \end{cases} \qquad (2.123)$$

where D_y is the diameter of the radar in the cross range direction and X_f is the focal range of the Hyperbolic radar. For the nth reflector located at the coordinates (x, y) in the image scene, the reflector is observable by the radar at the synthetic aperture domain

$$u \in [y - B, y + B]. \qquad (2.124)$$

If the target area of interest is $[-Y_0, Y_0]$ in the cross range and the synthetic aperture interval is $[-L, L]$ that includes the target area of interest, that is, $L = Y_0 + B$, then the effective radiated target area in the cross range becomes $[-(L + B), (L + B)]$. Since the half beam width B varies as the range value x changes, the synthetic aperture interval and radiated area are also changing with respect to the range value x. Now as with the Spotlight case, the return echo can be written as

$$s(\omega, u) = P(\omega)\sum_n a_n\left(\omega, x_n, y_n - u\right)a\left(\omega, x_n, y_n - u\right) \qquad (2.125)$$

$$\exp\left(-j2k\sqrt{x_n^2 + (y_n - u)^2}\right)$$

where all values are the same as defined before. As mentioned before, the nth reflector can only be observed by the radar at the synthetic aperture positions within $u \in [y_n - B_n, y_n + B_n]$ where $B_n = x_n\tan(\phi_d)$. Instead of referencing the location of the nth reflector with the image coordinates (x, y), we can give the location of the nth reflector in terms of the aspect angle. The aspect angle that the nth reflector makes with the radar can be written as a function of the radar position u as

$$\theta_n(u) = \arctan\left(\frac{y_n - u}{x_n}\right). \qquad (2.126)$$

Now we can determine the interval of the aspect angle that the nth reflector is observed by the synthetic aperture, which is given by

$$[\theta_n(y_n + B_n), \theta_n(y_n - B_n)] = \left[-\arctan\left(\frac{B_n}{x_n}\right), \arctan\left(\frac{B_n}{x_n}\right)\right] = [-\phi_d, \phi_d]. \quad (2.127)$$

The result is now only dependent of the radar parameter ϕ_d and independent of the reflector location. Performing the slow–time Fourier transform of $s(\omega, u)$ yields

$$S\left(\omega, k_u\right) = P(\omega) \sum_n A_n\left(\omega, k_u\right) A\left(\omega, k_n\right) \exp\left[-j\left(k_x x_n + k_y y_n\right)\right] \quad (2.128)$$

where $k_x = \sqrt{4k^2 - k_u^2}$ and $k_y = k_u$. The support band for ω is

$$[\omega_{\min}, \omega_{\max}] = [\omega_c - \omega_0, \omega_c + \omega_0] \quad (2.129)$$

and for k_u is $[-2k\sin(\phi_d), 2k\sin(\phi_d)]$. In other words, the **angular slow-time Doppler** ϕ takes range

$$\phi = \arcsin\left(\frac{k_u}{2k}\right) \in [-\phi_d, \phi_d]. \quad (2.130)$$

The target function can now be reconstructed using fast time and slow time match filtering

$$\begin{aligned} F(k_x, k_y) &= P^*(\omega)A^*\left(\omega, k_n\right) S\left(\omega, k_u\right) \quad (2.131) \\ &= |P(\omega)A\left(\omega, k_n\right)|^2 \sum_n A_n\left(\omega, k_u\right) \exp\left[-j\left(k_x x_n + k_y y_n\right)\right] \end{aligned}$$

and then the target function can be reconstructed using 2-D inverse Fourier transform with respect to k_x and k_y

$$f(x, y) = \sum_n f_n(x - x_n, y - y_n) \quad (2.132)$$

where

$$f_n(x, y) = \int_{k_x} \int_{k_y} |P(\omega)A\left(\omega, k_n\right)|^2 A_n\left(\omega, k_u\right) \exp\left[-j(k_x x + k_y y)\right]. \quad (2.133)$$

The resolution of a stripmap SAR system is dependent upon the bandwidth and geometric shape of the radar. Since the reconstructed target function is developed from inverse Fourier transform, the bandwidth of $|P(\omega)A\left(\omega, k_n\right)|^2 A_n\left(\omega, k_u\right)$ in (k_x, k_y) domain sets the resolution in (x, y). Lets assume the system uses planar radar.

$$k_x = \sqrt{4k^2 - k_u^2} = \sqrt{4k^2 - 4k^2 \sin^2(\phi)} = 2k\cos(\phi) \quad (2.134)$$

The bandwidth of the SAR image in the k_x domain is then given by $B_x = k_{x\max} - k_{x\min}$

where

$$k_{x\,\min} = 2k_{\min}\cos(\phi_d) \qquad \text{and} \qquad k_{x\,\max} = 2k_{\max}, \quad \text{at } \phi = 0. \tag{2.135}$$

The bandwidth in the $k_y = k_u$ domain for a planar radar is given by $B_y = \frac{8\pi}{D_y}$, where

$$
\begin{aligned}
k_u &\in [-2k\sin(\phi_d), 2k\sin(\phi_d)] \\
&\in \left[-2k\frac{\lambda}{D_y}, 2k\frac{\lambda}{D_y}\right] = \left[-\frac{4\pi}{D_y}, \frac{4\pi}{D_y}\right].
\end{aligned} \tag{2.136}
$$

Assuming the amplitude fluctuation is small, using the entire rectangular support area B_x by B_y, the 2–D inverse Fourier transform will produce the target function as a separable 2-D sinc function

$$\sin c\left(\frac{B_x x}{2\pi}\right)\sin c\left(\frac{B_y y}{2\pi}\right). \tag{2.137}$$

If half of the main lobe (first zero crossing) is used to represent the resolution width, the two–dimensional resolution cell in the target domain (x, y) is

$$
\begin{aligned}
\Delta x &= \frac{2\pi}{B_x} = \frac{2\pi}{2\left[\frac{\omega_{\max}}{c} - \frac{\omega_{\min}}{c}\cos(\phi_d)\right]} \approx \frac{\pi c}{2\omega_0}, \\
\Delta y &= \frac{2\pi}{B_y} = \frac{D_y}{4}.
\end{aligned} \tag{2.138}
$$

Since $\cos(\phi_d)$ is less than one, the actual theoretical resolution is better than the approximation. For the resolution in y domain, a more conservative value $\Delta y = \frac{D_y}{2}$ is often used. Similarly, for a hyperbolic antenna, from the divergence angle (2.123) and k_u bandwidth (2.136), we have

$$B_y = 4k_c\sin(\phi_d) = \frac{2\pi}{\lambda_c}4\sin(\phi_d) \tag{2.139}$$

where the $k_c = \frac{\omega_c}{c}$ is the wave number corresponding to the carry frequency of the radar. Thus the resolution for a hyperbolic radar in y domain becomes

$$
\begin{aligned}
\Delta y &= \frac{2\pi}{B_y} = \frac{\lambda_c}{4\sin(\phi_d)} \\
\text{or} &\approx \frac{\lambda_c}{2\sin(\phi_d)}
\end{aligned} \tag{2.140}
$$

for a more conservative estimation.

2.1.6.1 Slow–time Compression Slow–time compression is used in both spot and stripmap SAR for digital spotlighting and enhancing the reconstructed radar images. The slow-time compression technique is based on Fresnel approximation that assumes a narrow

28

bandwidth for the SAR system. The approximation is developed for far field assumption that

$$(y_n - u) \ll X_c \qquad \text{and} \qquad |x_n - X_c| \approx X_c \qquad (2.141)$$

in other words

$$\sqrt{x_n^2 + (y_n - u)^2} \approx X_c. \qquad (2.142)$$

Using the Taylor series expansion of the distance of the nth target to the radar at the position $(0, u)$ and dropping the higher order terms, we have

$$\sqrt{x_n^2 + (y_n - u)^2} \approx x_n + \frac{(y_n - u)^2}{2X_c}. \qquad (2.143)$$

It leads to the Fresnel approximation of the SAR spherical PM signal

$$\exp\left(-j2k\sqrt{x_n^2 + (y_n - u)^2}\right) \approx \exp\left(-j2kx_n - j\frac{k(y_n - u)^2}{X_c}\right) \qquad (2.144)$$

From the definition of instantaneous frequency of the spherical PM signal (2.38), we have

$$K_{un}(u) = \frac{\partial\left(-2k\sqrt{x_n^2 + (y_n - u)^2}\right)}{\partial u} \approx \frac{2k(y_n - u)}{X_c}. \qquad (2.145)$$

Considering the reference signal from a unit reflector at $(X_c, 0)$ for broadside target, it yields

$$s_0(\omega, u) = \exp\left(-j2k\sqrt{X_c^2 + u^2}\right) \approx \exp\left(-j2kX_c - j\frac{ku^2}{X_c}\right) \qquad (2.146)$$

with an instantaneous frequency equal to

$$K_{u0}(u) \approx -\frac{2ku}{X_c}. \qquad (2.147)$$

The slow–time compression is realized by the slow–time matched filtering

$$
\begin{aligned}
s_{nc}(\omega, u) &= s_n(\omega, u)s_0^*(\omega, u) \\
&\approx \sigma_n \exp\left(-j2kx_n - j\frac{k(y_n - u)^2}{X_c}\right)\exp\left(-j2kX_c - j\frac{ku^2}{X_c}\right) \\
&\approx \sigma_n \exp\left[-j2k(x_n - X_c)\right]\exp\left(j\frac{2ky_n}{X_c}u\right)
\end{aligned}
\qquad (2.148)
$$

where the phase term is approximated as $K_{un}(u) - K_{u0}(u)$ by ignoring a small constant phase term $-\frac{ky_n}{X_c}$ under the far field assumption. For the finite synthetic aperture

$u \in [-L, L]$, the slow–time compressed signal in Doppler k_u domain becomes

$$S_{nc}(\omega.k_u) \approx \sigma_n \exp\left[-j2k(x_n - X_c)\right] \frac{2L}{\pi} \operatorname{sinc}\left[\frac{L}{\pi}\left(k_u - \frac{2ky_n}{X_c}\right)\right]. \qquad (2.149)$$

The target appears as a sinc-like blip at

$$k_u = \frac{2ky_n}{X_c} \qquad (2.150)$$

which leads to the target cross–range location in slow–time domain at range X_c

$$y_n = \frac{X_c k_u}{2k}. \qquad (2.151)$$

The half of the main lobe of the sinc function yields the Doppler support bandwidth of the slow–time compressed signal is $\frac{2\pi}{L}$, that is

$$k_u \in \Omega_{nc} = \left[\frac{2ky_n}{X_c} - \frac{\pi}{L}, \frac{2ky_n}{X_c} + \frac{\pi}{L}\right]. \qquad (2.152)$$

The Doppler support bandwidth of the uncompressed signal $S_n(\omega.k_u)$ is

$$\begin{aligned} \Omega_n &= [2k\sin(\theta_n(L)), 2k\sin(\theta_n(-L)] \qquad &(2.153)\\ &\approx \left[\frac{2k(y_n - L)}{X_c}, \frac{2k(y_n + L)}{X_c}\right]. \end{aligned}$$

If all the targets $y_n \in [-Y_0, Y_0]$ are considered, the Doppler bandwidth of slow–time compressed signal becomes $\frac{4kY_0}{X_c} = \frac{8\pi Y_0}{\lambda X_c}$, that is

$$k_u \in \Omega_c \approx \left[-\frac{2kY_0}{X_c}, \frac{2kY_0}{X_c}\right] = \left[-\frac{4\pi Y_0}{\lambda X_c}, \frac{4\pi Y_0}{\lambda X_c}\right]. \qquad (2.154)$$

For the uncompressed signal, we have the Doppler bandwidth equal to $\frac{4k(Y_0+L)}{X_c} = \frac{8\pi(Y_0+L)}{\lambda X_c}$, that is

$$\begin{aligned} k_u &\in \Omega \approx \left[-\frac{2k(Y_0 + L)}{X_c}, \frac{2k(Y_0 + L)}{X_c}\right] \qquad &(2.155)\\ &= \left[-\frac{4\pi(Y_0 + L)}{\lambda X_c}, \frac{4\pi(Y_0 + L)}{\lambda X_c}\right]. \end{aligned}$$

This leads to the restrictions on slow–time sampling interval

$$\Delta u_c \leq \frac{2\pi}{B_{\Omega_c}} = \frac{\lambda X_c}{4Y_0} \qquad \text{and} \qquad \Delta u \leq \frac{2\pi}{B_\Omega} = \frac{\lambda X_c}{4(Y_0 + L)} \qquad (2.156)$$

for the slow–time compressed signal and uncompressed signal respectively. We can see that the sampling interval restriction for the slow–time compressed signal is much easier such that

Δu_c can be greater than Δu. From the definition of $\Delta u = \frac{v_r}{\text{PRF}}$, we can have the following two desirable outcomes that PRF can be reduced or the carrier speed can be increased, if Δu_c is used to sample the slow–time compressed signal. The slow–time Nyquist rates also indicate that a larger illuminated ($2Y_0$) target area and longer ($2L$) synthetic aperture require finer sampling interval..

For the squint case, the scene center is located at (X_c, Y_c), therefore, we have

$$r_n = \sqrt{x_n^2 + y_n^2} \qquad \text{and} \qquad R_c = \sqrt{X_c^2 + Y_c^2} \tag{2.157}$$

to represent the distance from radar location $u = 0$ to the nth target and scene center respectively. Then, similarly, we have the slow–time compressed signal

$$
\begin{aligned}
s_c(\omega, u) &= s(\omega, u) s_0^*(\omega, u) \\
&\approx \sum_n \sigma_n \exp\left[-j2k(r_n - R_c)\right] \exp\left(j\frac{2k\cos(\theta_c)(y_n - Y_c)}{R_c}u\right)
\end{aligned} \tag{2.158}
$$

where $\theta_c = \arctan\left(\frac{Y_c}{X_c}\right)$ is the squint angle. The reference signal is

$$s_0(\omega, u) = \exp\left(-j2k\sqrt{X_c^2 + (Y_c - u)^2}\right). \tag{2.159}$$

The slow–time compressed signal in Doppler k_u domain becomes

$$S_c(\omega.k_u) \approx \sum_n \sigma_n \exp\left[-j2k(r_n - R_c)\right]\frac{2L}{\pi}\sin c\left[\frac{L}{\pi}\left(k_u - \frac{2k\cos(\theta_c)(y_n - Y_c)}{R_c}\right)\right]. \tag{2.160}$$

The sinc–like blip for the nth target is now located at

$$k_u = \frac{2k\cos(\theta_c)(y_n - Y_c)}{R_c} = \frac{2k\cos^2(\theta_c)(y_n - Y_c)}{X_c} \tag{2.161}$$

and its scale transform in cross–range domain is

$$y_n = \frac{k_u R_c}{2k\cos(\theta_c)} + Y_c \tag{2.162}$$

which can be reduced to the broadside result (2.151) when $Y_c = 0$. Substituting the $y_n \in [Y_c - Y_0, Y_c + Y_0]$ into equation (2.161), the compressed slow–time Doppler support band becomes

$$k_u \in \Omega_c \approx \left[-\frac{2kY_0\cos(\theta_c)}{R_c}, \frac{2kY_0\cos(\theta_c)}{R_c}\right] \tag{2.163}$$

where half of the main lobe, $\frac{\pi}{L}$, of the sinc function is ignored. Therefore, the sampling

31

interval in the cross–range domain must satisfy

$$\Delta u_c \leq \frac{2\pi}{B_{\Omega_c}} = \frac{\lambda R_c}{4Y_0 \cos(\theta_c)} \tag{2.164}$$

which is less restrictive than the one for uncompressed signal in the cross–range

$$\Delta u \leq \frac{2\pi}{B_{\Omega}} = \frac{\lambda R_c}{4(Y_0 + L) \cos(\theta_c)}. \tag{2.165}$$

However, this is not true in stripmap SAR. Under the assumption that the scene center is at $(X_c, 0)$ (broadside), $|u| \ll X_c$ and the nth target at (x_n, y_n) can only be observed by the radar at the locations within synthetic aperture interval $u \in [y_n - B_n, y_n + B_n]$ where $B_n = x_n \tan \phi_d$, the slow–time compressed signal stripmap SAR signal becomes

$$S_c(\omega.k_u) \approx \sum_n \sigma_n \exp\left[-j2k(r_n - X_c)\right] \frac{2B_n}{\pi} \operatorname{sinc}\left[\frac{B_n}{\pi}\left(k_u - \frac{2ky_n}{r_n}\right)\right] \tag{2.166}$$

where Fresnel approximations of radar signal

$$\begin{aligned} \sqrt{x_n^2 + (y_n - u)^2} &= \sqrt{x_n^2 + y_n^2 - 2y_n u + u^2} \\ &\approx r_n + \frac{u^2 - 2y_n u}{2r_n} \end{aligned} \tag{2.167}$$

and reference signal

$$\sqrt{X_c^2 + u^2} \approx X_c + \frac{u^2}{2r_n} \tag{2.168}$$

are used. Compared with equation (2.160), L is replaced by B_n due to the change of synthetic aperture interval length. For each target, the main lobe width of the sinc–like function yields

$$k_{un} \in \Omega_{nc} = \left[\frac{2ky_n}{r_n} - \frac{\pi}{B_n}, \frac{2ky_n}{r_n} + \frac{\pi}{B_n}\right]. \tag{2.169}$$

If we consider the entire observable target area for the radar locations

$$u \in [-L, L] = [-(Y_0 + B), (Y_0 + B)], \tag{2.170}$$

the bandwidth of the slow–time compressed signal $S_c(\omega.k_u)$ becomes

$$k_u \in \Omega_c = \left[-\frac{2kY_0}{r_{\min}} - \frac{2kB}{r_{\min}}, \frac{2kY_0}{r_{\min}} + \frac{2kB}{r_{\min}}\right] \tag{2.171}$$

where $\frac{\pi}{B_n}$ is ignored. The support band Ω_c depends on the type of radar and its bandwidth and beamwidth. A conservative estimation of the slow–time Doppler bandwidth of the

compressed stripmap SAR signal can be formed as

$$k_u \in \Omega_c = [-2k\sin\theta_{0\_\max} - 4k\sin\phi_d, 2k\sin\theta_{0\_\max} + 4k\sin\phi_d] \qquad (2.172)$$

where

$$\theta_{0\_\max} = \arctan\left(\frac{Y_0}{x_{\min}}\right) \qquad (2.173)$$

is the maximum aspect angle of the target area for the radar at $u = 0$. Since

$$\phi_d = \arctan\left(\frac{B_n}{x_n}\right) \qquad (2.174)$$

is the beam divergence angle, then a conservative estimation

$$\frac{B}{r_{\min}} \approx 2\sin\phi_d \qquad (2.175)$$

is used for $r_{\min}$ in the equation. Compared with the slow–time Doppler support band of the uncompressed SAR signal $S(\omega.k_u)$,

$$k_u \in \Omega = [-2k\sin\phi_d, 2k\sin\phi_d] \qquad (2.176)$$

the slow–time compressed SAR signal has a wider bandwidth. Therefore, the Nyquist sampling restriction of the slow–time compressed SAR signal,

$$\Delta u_c < \frac{\pi}{2k_{\max}\sin\theta_{0\_\max} + 4k_{\max}\sin\phi_d} = \frac{\lambda_{\min}}{4\sin\theta_{0\_\max} + 8\sin\phi_d}, \qquad (2.177)$$

is more tighter than the uncompressed SAR signal

$$\Delta u < \frac{\pi}{2k_{\max}\sin\phi_d} = \frac{\lambda_{\min}}{4\sin\phi_d}. \qquad (2.178)$$

In stripmap mode, even the sampled uncompressed SAR signal $S(\omega.k_u)$ does not have aliasing error, it must be upsampled prior to applying slow–time compression.

2.1.6.2   Digital Spotlighting In order to complete the stripmap image method, we need to understand the technique referred to as digital spotlighting. Digital spotlighting is to restrict the return radar signature within a specific target area. In the previous discussion, we decide the Nyquist sampling interval based on the main lobe bandwidth of the radar radiation pattern. The returned energy from the side lobes of the radiation pattern is considered to be small. However, the side lobe energy will appear as aliasing error in the signal. The digital spotlighting will suppress the radar energy outside the desired target area, such as the energy from side lobes, to reduce aliasing error.

Under the assumption of narrow–beamwidth and narrow swath, that is $r_n \approx R_c$, we have the slow–time compressed SAR signal (2.160) for a squint target area in the last section. Equation (2.161) shows the location of the sinc–like blip for the nth target. The digital

spotlighting is to suppress the SAR signal of the targets that are outside a desired target area, say

$$y \in [Y_c - Y_0, Y_c + Y_0] \qquad \text{and} \qquad x \in [X_c - X_0, X_c + X_0]. \tag{2.179}$$

The implementation of range (x) and cross–range (y) gating is usually done in (t, k_u) domain using polar format processing. Considering the slow–time compressed signal shifted to scene center (X_c, Y_c),

$$
\begin{aligned}
s_c(\omega, u) &= s(\omega, u) s_0^*(\omega, u) \\
&= P(\omega) \sum_n \sigma_n \exp\left[-j2k\sqrt{(X_c + x_n)^2 + (Y_c + y_n - u)^2}\right] \quad (2.180) \\
&\quad P^*(\omega) \exp\left[j2k\sqrt{X_c^2 + (Y_c - u)^2}\right].
\end{aligned}
$$

The following approximation is used in the polar format processing.

$$
\begin{aligned}
\sqrt{(X_c + x_n)^2 + (Y_c + y_n - u)^2} &= \sqrt{X_c^2 + 2X_c x_n + x_n^2 + y_n^2 + 2y_n(Y_c - u) + (Y_c - u)^2} \\
&= \sqrt{X_c^2 + (Y_c - u)^2} + \cos\theta_0(u) x_n + \\
&\quad \sin\theta_0(u) y_n + \cdots \\
&\approx \sqrt{X_c^2 + (Y_c - u)^2} + \cos\theta_0(u) x_n + \qquad (2.181) \\
&\quad \sin\theta_0(u) y_n
\end{aligned}
$$

where the high order terms are ignored and

$$\theta_0(u) = \arctan\left(\frac{Y_c - u}{X_c}\right) \tag{2.182}$$

is the aspect angle of the radar at location u with respect to the center of target area. Using the approximation, equation (2.180) can be simplified as the target function in (k_x, k_y) domain,

$$
\begin{aligned}
s_c(\omega, u) &\approx |P(\omega)|^2 \sum_n \sigma_n \exp\left[-j2k\cos\theta_0(u) x_n - j2k\sin\theta_0(u) y_n\right] \\
&\approx |P(\omega)|^2 \sum_n \sigma_n \exp\left[-jk_x(\omega, u) x_n - jk_y(\omega, u) y_n\right] \qquad (2.183) \\
&= F(k_x, k_y)
\end{aligned}
$$

where

$$k_x(\omega, u) = 2k\cos\theta_0(u) \qquad \text{and} \qquad k_y(\omega, u) = 2k\sin\theta_0(u) \tag{2.184}$$

are the polar function mapping from (ω, u) to (k_x, k_y).

In narrow beamwidth situation, $u \ll R_c$, the aspect angle can be simplified as a linear

34

function of u,

$$
\begin{aligned}
\theta_0(u) &= \arctan\left(\frac{Y_c - u}{X_c}\right) \approx \arctan\left(\frac{Y_c}{X_c}\right) - \frac{u}{X_c} \\
&\approx \theta_c - \frac{\cos\theta_c}{R_c}u.
\end{aligned} \tag{2.185}
$$

The polar function mapping (2.184) in narrow beamwidth becomes

$$
\begin{aligned}
k_x(\omega, u) &= 2k\cos\left(\theta_c - \frac{\cos\theta_c}{R_c}u\right) \\
&= 2k\left[\cos\theta_c\cos\left(\frac{\cos\theta_c}{R_c}u\right) + \sin\theta_c\sin\left(\frac{\cos\theta_c}{R_c}u\right)\right] \\
&\approx 2k\cos\theta_c \qquad \text{(independent of u)}
\end{aligned} \tag{2.186}
$$

and

$$
\begin{aligned}
k_y(\omega, u) &= 2k\sin\left(\theta_c - \frac{\cos\theta_c}{R_c}u\right) \\
&= 2k\left[\sin\theta_c\cos\left(\frac{\cos\theta_c}{R_c}u\right) - \cos\theta_c\sin\left(\frac{\cos\theta_c}{R_c}u\right)\right] \\
&\approx 2k\left[\sin\theta_c - \frac{\cos^2\theta_c}{R_c}u\right]. \qquad \text{(linear function of u)}
\end{aligned} \tag{2.187}
$$

In the case of narrow beamwidth and narrow bandwidth, that is $|k - k_c| \ll k_c$ (k_c is the wavenumber at the carrier frequency), the polar function mapping can be further simplified by $k \approx k_c$ in some of the terms with smaller quantities

$$
k_x(\omega) \approx 2k\cos\theta_c = \frac{2\cos\theta_c}{c}\omega, \qquad k_x \leftarrow \omega \tag{2.188}
$$

and

$$
k_y(u) \approx 2k_c\left[\sin\theta_c - \frac{\cos^2\theta_c}{R_c}u\right], \qquad k_y \leftarrow u \tag{2.189}
$$

where squint angle θ_c is assumed to be much smaller than 1 (near–broadside case). The polar function mapping becomes simple linear scale mapping from $s_c(\omega, u)$ to $F(k_x, k_y)$ without the need of interpolation. The target function reconstruction can be realized by simply performing two dimensional inverse Fourier transform of the slow–time compressed signal $s_c(\omega, u) = F(k_x, k_y)$. We shall notice that the approximation can cause some of the geometric distortion in the reconstructed target function.

In a more accurate analysis of polar format processing, the location of nth target is expressed in a polar spatial coordinates $[\theta_n(0), r_n]$ where $\theta_n(0)$ is the aspect angle from the radar at $u = 0$ to the nth target and r_n is the distance from the radar to the target. The target

located at $[\theta_n(0), r_n]$ should appear at

$$t_n \approx \frac{2r_n}{c} \qquad \text{and} \qquad k_{un} \approx 2k_c \sin\left[\theta_n(0) - \theta_c\right] \tag{2.190}$$

in the polar format processed data (2.183) at the (t, k_u) domain. Since

$$x_n = r_n \cos\theta_n(0) \qquad \text{and} \qquad y_n = r_n \sin\theta_n(0), \tag{2.191}$$

then we have

$$x_n = \frac{ct_n}{2} \cos\left[\phi_n + \theta_c\right] \qquad \text{and} \qquad y_n = \frac{ct_n}{2} \sin\left[\phi_n + \theta_c\right] \tag{2.192}$$

where

$$\phi_n = \arcsin\left(\frac{k_{un}}{2k_c}\right) = \theta_n(0) - \theta_c \tag{2.193}$$

is the angular slow–time Doppler. Therefore, a two–dimensional Fourier transform of the polar format processed data $s_c(\omega, u)$ to (t, k_u) domain can be used for geometric correction, motion compensation and digital spotlighting. Note $\omega \to t$ is the inverse Fourier transform and $u \to k_u$ is the slow–time Fourier transform.

The digital spotlighting the desired target area (2.179) can be realized by a digital spotlight filter in (t, k_u) domain

$$W(t, k_u) = \begin{cases} 1 & \text{for } |x - X_c| < X_0 \ \& \ |y - Y_c| < Y_0 \\ 0 & \text{other wise} \end{cases} \tag{2.194}$$

where

$$x = \frac{ct}{2} \cos\left[\phi + \theta_c\right] \qquad \text{and} \qquad y = \frac{ct}{2} \sin\left[\phi + \theta_c\right] \tag{2.195}$$

where $\phi = \arcsin(\frac{k_u}{2k_c})$ is the angular slow–time Doppler at the carrier frequency (narrow–bandwidth assumption). For wide–bandwidth SAR system, one–dimensional interpolation has to be used for the mapping of $\phi = \arcsin(\frac{k_u}{2k})$ from k_u domain to ϕ domain. The digital spotlighted slow–time compressed signal can be obtained by following processes.

$$\text{I). } f_d(t, k_u) = W(t, k_u)\mathcal{F}_{\omega \to t; u \to k_u}\left\{s_c(\omega, u)\right\} \qquad \text{spotlight filter} \tag{2.196}$$

$$\text{II). } S_{cd}(\omega, k_u) = \mathcal{F}_{t \to \omega}\left\{f_d(t, k_u)\right\} \qquad \text{spotlighted in } (\omega, k_u) \tag{2.197}$$

$$\text{III). } s_{cd}(\omega, u) = \mathcal{F}^{-1}_{k_u \to u}\left\{S_{cd}(\omega, k_u)\right\} \qquad \text{digital spotlighted} \tag{2.198}$$

Between the process II). (2.197) and III). (2.198), an optional zero padding in the k_u domain can be applied to up–sample the data from the sampling interval Δu_c to a finer sampling interval Δu.

2.1.6.3   Subaperture Digital Spotlighting The above discussion of full aperture digital spotlighting is based on the assumptions in (2.190). We assume the radial distance r_n from the nth target to the radar located at the center of synthetic aperture $u = 0$ to be the constant radial distance for all the radar locations $u \in [-L, L]$. The fast–time of arrival t_n would be different for a large synthetic aperture. This problem can be addressed by dividing the entire aperture $2L$ into N subapertures of length $2L_s$ such as

$$[Y_i - L_s, Y_i - L_s] \qquad \text{and} \qquad Y_i = (2i - 1)L_s - L \tag{2.199}$$

where $i = 1, 2, \cdots, N$. The center of target area for the ith subaperture is located at

$$(X_c, Y_c + Y_i) \tag{2.200}$$

and the squint angle

$$\theta_{ci} = \arctan\left(\frac{Y_c + Y_i}{X_c}\right). \tag{2.201}$$

Now the fast–time of arrival for each subaperture can be approximated as constant within each subaperture

$$t_{ni} \approx \frac{2\sqrt{x_n^2 + (y_n + Y_i)^2}}{c} \tag{2.202}$$

The digital spotlighting process step I). (2.196) is performed only within each subaperture

$$\text{I).} \; f_{di}(t, k_u) = W_i(t, k_u)\mathcal{F}_{\omega \to t; u \to k_u}\left\{s_c(\omega, u)\right\}; \qquad u \in [Y_i - L_s, Y_i - L_s] \tag{2.203}$$

where the spotlight filter for i^{th} subaperture is

$$W_i(t, k_u) = \begin{cases} 1 & \text{for } |x - X_c| < X_0 \; \& \; |y - Y_c - Y_i| < Y_0 \\ 0 & \text{other wise} \end{cases} \tag{2.204}$$

and

$$x = \frac{ct}{2}\cos\left[\phi + \theta_{ci}\right] \qquad \text{and} \qquad y = \frac{ct}{2}\sin\left[\phi + \theta_{ci}\right]. \tag{2.205}$$

Followed by step II). (2.197) and step III). (2.198) with zero–padding if necessary. The N subapertures of digital spotlighted SAR data are then appended to each other for form $s_{cd}(\omega, u)$ for SAR imaging. The smaller subaperture $2L_s$ improves the estimation of fast–time of arrival. The proper subaperture length $2L_s$ should be about 100th of the slow–time Doppler support band of the compressed SAR signal $s_c(\omega, u)$ in (2.163). That is

$$\frac{\pi}{L_s} \approx \frac{2k_{\min}Y_0 \cos(\theta_c)}{100 \cdot R_c} \tag{2.206}$$

and

$$L_s \approx \frac{25R_c\lambda_{\max}}{Y_0 \cos(\theta_c)}. \tag{2.207}$$

37

For a planar radar, the slow–time Doppler support band of the compressed SAR signal is about $\frac{8\pi}{D_y}$ (2.136) which leads to

$$\frac{\pi}{L_s} \approx \frac{4\pi}{100 D_y} \qquad \text{and} \qquad L_s \approx 25 D_y. \tag{2.208}$$

In stripmap SAR imaging, both full aperture or subaperture digital spotlighting can be applied. However, there are two reasons to use subaperture: the first one is to provide an accurate digital spotlight filter and the second one is the relax the Nyquist sampling restriction for the slow–time compressed SAR signal, such that

$$\Delta u_c \approx \Delta u = \frac{\lambda_{\min}}{4 \sin \phi_d}. \tag{2.209}$$

There is no need for interpolation before slow–time compression. In stripmap mode, the broadside SAR is often used, that is $Y_c = 0$. The center of target area for the ith subaperture is located at

$$(X_c, Y_i) \tag{2.210}$$

and the squint angle

$$\theta_{ci} = \arctan\left(\frac{Y_i}{X_c}\right). \tag{2.211}$$

The digital spotlighting process step I). (2.203) is exactly the same only with slightly changed spotlight filter for i^{th} subaperture

$$W_i(t, k_u) = \begin{cases} 1 & \text{for } |x - X_c| < X_0 \ \& \ |y - Y_i| < Y_0 \\ 0 & \text{other wise} \end{cases} \tag{2.212}$$

and

$$x = \frac{ct}{2} \cos[\phi + \theta_{ci}] \qquad \text{and} \qquad y = \frac{ct}{2} \sin[\phi + \theta_{ci}]. \tag{2.213}$$

If the full aperture digital spotlight is used, up–sampling must be performed on SAR signal $s(\omega, u)$ before slow–time compression.

2.1.6.4   Stripmap Imaging Algorithm To summarize the discussion of stripmap imaging method, a eight–step strip SAR imaging algorithm is presented here.

Step 1: Perform discrete fast–time matched filtering of the received signal such as

$$s_M(t, u) = s(t, u) * p_0^*(-t) \tag{2.214}$$

where $p_0(t) = p(t - T_c)$ is echo signal from a unit reflector at the center $(X_c, 0)$ of range swath which is invariant for the stripmap SAR. And $T_c = \frac{2X_c}{c}$ is referred to as the reference fast–time point. We need to decide the fast–time sampling duration of the radar signal

$t \in [T_{start}, T_{end}]$ where

$$T_{start} = \frac{2r_{\min}}{c}, \qquad T_{end} = \frac{2r_{\max}}{c} + T_p. \tag{2.215}$$

$[r_{\min}, r_{\max}]$ is the SAR range gate which defines closest and farthest radial distance of the radar swath. T_p is radar pulse width. We know the range gate is function of radar frequency

$$\omega \in [\omega_{\min}, \omega_{\max}] = [\omega_c - \omega_0, \omega_c + \omega_0]. \tag{2.216}$$

The largest radar range swath equal to $[X_c - X_{0\,\max}, X_c + X_{0\,\max}]$ where $X_{0\,\max} \approx \frac{\lambda_{\max} X_c}{D_x}$ occurs at the lowest fast–time frequency ($\frac{2\pi}{\lambda_{\max}} = k_{\min}$) and D_x is the effective diameter of a planar radar. Therefore, the range gate can be decided as

$$r_{\min} = X_c - X_{0\,\max}, \qquad r_{\max} = \sqrt{(X_c + X_{0\,\max})^2 + B_{\max}^2} \tag{2.217}$$

where $B_{\max} \approx \frac{(X_c + X_{0\,\max})\lambda_{\max}}{D_y}$ is the maximum half–width cross–range beamwidth for a planar radar with an effective diameter D_y. The fast–time sampling interval must satisfy the Nyquist sampling rate $\Delta t \leq \frac{\pi}{\omega_0}$ for a radar bandwidth $2\omega_0$. Therefore, the (even) number of discrete range bins is equal to

$$N = 2 \left\lceil \frac{T_{end} - T_{start}}{2\Delta t} \right\rceil. \tag{2.218}$$

The reference fast–time point depending on the range swath is often selected as

$$T_c = \frac{T_{end} - T_{start}}{2}. \tag{2.219}$$

Therefore, the matched filter result, $s_M(t, u)$, has $\frac{N}{2} + 1$ samples corresponding to the reference fast–time point T_c.

Step 2: Perform the fast–time and slow–time processing. The fast–time processing is to apply Fourier transform

$$s(\omega, u) = \mathcal{F}_{t \rightarrow \omega} \{s_M(t, u)\}. \tag{2.220}$$

The slow–time processing include digital spotlighting and slow–time compression. If

$$T_{end} - T_{start} < \frac{4X_0}{c \cdot \cos \theta_{\max}}$$

where $\theta_{\max} = \arctan\left(\frac{Y_c + Y_0 + L}{X_c - X_0}\right)$ is the largest slow–time Doppler frequency, then zero–padding must be performed such that the data length is at least equal to $N\Delta t = \frac{4X_0}{c \cdot \cos \theta_{\max}}$ before the Fourier transform (2.220) from t to ω. This zero–padding is to make sure there are no aliasing errors (sufficient frequency resolution) in ω so as in k_x domains. If full aperture digital spotlighting of the data is expected, the data must be first up–sampled from Δu to

Δu_c before performing slow–time compression

$$s_c(\omega, u) = s(\omega, u)s_0^*(\omega, u). \tag{2.221}$$

Then either perform full aperture digital spotlighting (2.196) or subaperture digital spotlighting (2.203) followed by procedures (2.197) and (2.198) to produce $s_{cd}(\omega, u)$ a slow–time compressed and digital spotlighted SAR signal. In the case that the size of the target area in the cross–range is greater than the length of the synthetic aperture, that is $Y_0 > L$, zero–padding $s_c(\omega, u)$ in the cross–range to $u \in [-Y_0, Y_0]$ is required before digital spotlight filter (2.196) or (2.203). This zero–padding is to guarantee sufficient frequency resolution in k_u domain without aliasing errors. Perform slow–time decompression with down sampling if up–sampling was applied before for full aperture digital spotlighting to produce

$$s_d(\omega, u) = s_{cd}(\omega, u)s_0(\omega, u). \tag{2.222}$$

$s_d(\omega, u)$ is a digital spotlighting enhanced version of SAR signal $s(\omega, u)$.

Step 3: Perform Fourier transform of $s_d(\omega, u)$ in cross–range u, it yields

$$S_d(\omega, k_u) = \mathcal{F}_{u \to k_u} \{s_d(\omega, u)\}. \tag{2.223}$$

It is a discrete version of digital spotlighted SAR signal $S_d(\omega_n, k_{um})$.

Step 4: In the case of $Y_0 < L$ (in most of case $L = Y_0 + B$), subsampling in Doppler domain k_u can be performed to reduce the computational burden and data size. That is because the data sampling space (resolution) in $\Delta k_u = \frac{\pi}{L}$ due to $u \in [-L, L]$. However, the actual target area in cross–range is $u \in [-Y_0, Y_0]$. The Nyquist sampling restriction is $\Delta k_u \leq \frac{\pi}{Y_0}$. Therefore, if $L = 2Y_0$, then we can subsample by 2 (skip a sample) in k_u domain.

Step 5: As said in "Step 1", $s_M(t, u)$ has $\frac{N}{2} + 1$ samples and the first sample corresponding to the reference fast–time point T_c. However, the definition of DFT assumes that the first sample is at $t = 0$ which causes a data shift $t + T_c$. We need to correct this by a phase delay

$$S_d(\omega, k_u) \exp(-j\omega T_c) \tag{2.224}$$

such that the data is shifted back to actual $t = 0$ in fast–time domain.

Step 6: Perform base band conversion of the target area to obtain the target function

$$F(k_x, k_y) = S_d(\omega, k_u) \exp(-j\omega T_c) \exp(j\sqrt{4k^2 - k_u^2} \cdot X_c \tag{2.225}$$

where $k_x = \sqrt{4k^2 - k_u^2}$ and $k_y = k_u$ in discrete samples

$$k_{xmn} = \sqrt{4k_n^2 - k_{um}^2} \qquad \text{and} \qquad k_{ymn} = k_{um}. \tag{2.226}$$

This nonlinear transformation converts the sampled SAR signal from an evenly spaced sampling domain (ω_n, k_{um}) to an unevenly spaced sampling domain (k_{xmn}, k_{ymn}).

Step 7: Perform spatial frequency interpolation to form a uniform grid in the following spatial frequency support regions:

$$
\begin{aligned}
k_x &\in [k_{x\min} = \min\{k_{xmn}\}, k_{x\max} = \max\{k_{xmn}\}] \quad \text{and} \\
k_y &\in [k_{y\min} = \min\{k_{ymn}\}, k_{y\max} = \max\{k_{ymn}\}].
\end{aligned}
$$

Then the uniform grid spacing are decided according to the radar footprint $2X_0$ by $2Y_0$ such that

$$
\Delta k_x = \frac{\pi}{X_0} \quad \text{and} \quad \Delta k_y = \frac{\pi}{Y_0}. \tag{2.227}
$$

The total numbers of samples to be interpolated equal to

$$
N_x = 2 \left\lceil \frac{k_{x\max} - k_{x\min}}{2\Delta k_x} \right\rceil \quad \text{and} \quad N_y = 2 \left\lceil \frac{k_{y\max} - k_{y\min}}{2\Delta k_y} \right\rceil. \tag{2.228}
$$

Now perform spatial frequency interpolation algorithm using the unevenly spaced data points $F(k_{xmn}, k_{ymn})$ to form an evenly sampled $F(k_x, k_y)$ over the N_x by N_y uniform grid.

Step 8: Take the 2-D inverse discrete Fourier transform of the spatial frequency interpolated target spectrum $F(k_x, k_y)$ to yield a target function

$$
f(x, y) = \mathcal{F}^{-1}_{k_x, k_y \to x, y} (F(k_x, k_y)) \tag{2.229}
$$

which is evenly sampled with the following uniform sampling interval

$$
\Delta_x = \frac{2\pi}{N_x \Delta k_x} = \frac{2X_0}{N_x} \quad \text{and} \quad \Delta_y = \frac{2\pi}{N_y \Delta k_y} = \frac{2Y_0}{N_y}. \tag{2.230}
$$

2.1.7   Motion Compensation

All of the target function reconstruction algorithms presented assumes that the radar-carrying vehicle maintains a constant velocity and maintains a constant linear motion path within only a few wavelengths of the radar signal. These nonlinear motion components (also called motion errors) cause "fuzziness" in the SAR image, which must be compensated for in order to arrive at the optimal image. Motion compensation is usually done in two stages: first using global positioning system (GPS), and second using in scene targets.

The first step in the development of the motion compensation equations is the modeling of the motion errors. The motion errors in the range x and cross–range y domain can be represented as

$$
[x_e(u), u + y_e(u)]. \tag{2.231}
$$

Now if we place a unit reflector at (x_n, y_n), the received SAR signal with motion error

becomes

$$s_n(\omega, u) = \exp\left[-j2k\sqrt{(x_n - x_e(u))^2 + (y_n - u - y_e(u))^2}\right] \qquad (2.232)$$

as contrast to the case without motion error $s_n(\omega, u) = \exp\left[-j2k\sqrt{x_n^2 + (y_n - u)^2}\right]$.
Now we can rewrite the equation

$$s_n(\omega, u) = a_{en}(\omega, x_n, y_n - u) \exp\left[-j2k\sqrt{x_n^2 + (y_n - u)^2}\right] \qquad (2.233)$$

where

$$a_{en}(\omega, x_n, y_n - u) = \exp\left[-j2kr_{en}(u)\right] \qquad (2.234)$$

is called the motion phase error function and

$$r_{en}(u) = \sqrt{x_n^2 + (y_n - u)^2} - \sqrt{(x_n - x_e(u))^2 + (y_n - u - y_e(u))^2} \qquad (2.235)$$

is called the radial error for the nth target. Now if the fluctuations of the motion phase
error function are much smaller than the error free SAR signal, we can model the phase
error function of the signal as a filter in the spatial frequency domain (k_x, k_y). This can be
represented as

$$\begin{aligned} H_{en}(k_x, k_y) &= a_{en}(\omega, x_n, y_n - u) \qquad (2.236) \\ &= \exp\left[-j2kr_{en}(u)\right] \end{aligned}$$

where $2k = \sqrt{k_x^2 + k_y^2}$ and $u = y_n - \frac{k_y}{k_x}x_n$. If a GPS sensor is placed with the radar system,
an estimate of the vehicle trajectory can be made and from this information, the motion error
can be estimated.

The image created using the GPS based motion compensation may still have motion
errors because of the in accuracy of the GPS system. The second step is to further refine
the motion compensation using in scene targets. Suppose there exists a distinct target (say a
fiducial reflector or a communication tower) in the imaging scene. The SAR image signature
(peak) of the distinct in–scene target can be identified at location (x_l, y_l). If we extract the
SAR signature as $h_{el}(x, y)$ from the scene, that is to shifted it by $(-x_l, -y_l)$. Since we know
there is motion phase error included in this SAR signature, the extracted feature now only
contains radial error in the phase (2.235). The two–dimensional Fourier transform

$$H_{en}(k_x, k_y) = F_{x,y \to k_x, k_y}\{h_{el}(x, y)\} \qquad (2.237)$$

forms motion error filter function for the in–scene target. In a narrow beamwidth case, the
radial motion error for the in–scene target can be approximated by

$$r_{en}(u) \approx x_e(u)\cos\theta_c + y_e(u)\sin\theta_c \qquad (2.238)$$

42

where θ_c is the average target squint angle. For stripmap case, usually $\theta_c = 0$, then $r_{en}(u) \approx x_e(u)$. That shows the motion error is spatially invariant in the scene. Therefore, the in–scene target motion compensation for the narrow beamwidth radar can be realized by

$$f(x, y) = \mathcal{F}^{-1}_{k_x, k_y \to x, y} \left\{ F(k_x, k_y) H^*_{el}(k_x, k_y) \right\}. \tag{2.239}$$

2.2   Prior Works in SAR Parametric Study Reviewed

In this section, we will outline the past research related to SAR parametric and automatic target recognition (ATR) study. The field of SAR and ATR are relatively new. We found most of the works are in the past decade. From the brief summary of the SAR imaging algorithms, we can see there are many variations in SAR imaging technology from type of radar, radar parameters to approximation methods. Some of the key radar parameter variations also known as sensor operating conditions (OC's) include

1.   Type of radar antenna which has influence on parameters like divergence angle (beamwidth), radiation pattern, resolution, radar footprint, etc.
2.   Radar frequencies and bandwidth which also has influence on parameters of resolution, radiation pattern, radar footprints, etc.
3.   Antenna polarization
4.   Depression (elevation) angle
5.   Squint angle
6.   Synthetic aperture length
7.   Pulse Repetition Frequency (PRF)
8.   Target function reconstruction algorithms based on different approximation methods
9.   Image enhancement technologies such as digital spotlighting, motion compensations and others
10.   Radar waveforms such as pulse, chirp and white noise.
11.   Noises

Any combinations of those SAR parameter variations can have significant impact on the appearance, resolution, contrast, signature locations and geometric distortions in SAR image. However, there were no prior systematic research to address how those sensor parameter variations would affect the performance of ATR algorithms either qualitatively nor quantitatively. In two–dimensional image based SAR ATR algorithms, the database is build around the same collection of data. The training data set and testing data set are from the same data acquisition platform. There are no variations of sensor OC's in either data set collections or ATR algorithms development and testing. For example, in MSTAR data, the only sensor variation is a collection of data sets in two different depression angles. It is difficult and expensive to collect data sets that cover a broad aspects of sensor operating conditions. In addition, the existing image ATR algorithms never have to face the data from different SAR sensor platforms with different sensor OC's. The same target under the same

target OC's and the environmental OC's will appear significantly different in SAR images with different variations of sensor OC's. In our literature review, we have collected any research papers that covers the studies on one or more sensor parameters. The studies of sensor parameters that we reviewed cover not only ATR but also in image formation. We will organize our review according to particular sensor parameters and its influence on ATR or image formation. As we stated earlier, not all the sensor parameters are addressed by prior research.

2.2.1   Frequency

The frequencies used in the radar pulse is one of the sensor parameters that has the largest effect on SAR image formation. The frequency of the electromagnetic radiation used by the radar affects the scattering of the wave by the object and the penetration of the radar wave.

The wavelength of the excitation, which is equal to the inverse of the frequency of the radar wave, determines several of the scattering characteristics of the target. Radar imagery is principally separated from optical imagery by the frequency of the radiation used for imaging. For a complex object, a physical feature of that object will only be visible if the size of the feature is larger than the wavelength used to image it. Since radar generally operates at lower frequency than optical systems, many of the details of a complex object that appear in an optical image will be blurred by the radar pulse to the level below perception in the image. Lower frequencies used in the radar pulse have the advantage of being able to penetrate several mediums. Low frequency radar has been developed to image objects in vegetation (FOliage PENetrating radar or FOPEN) and image objects underground. (Ground PENetrating radar or GPEN)

The Foliage penetrating radar use UHF and VHF frequencies along with ultra wide bandwidth (UWB) and ultra wide angle signal properties which dramatically changes the phenomenology observed compared to traditional SAR. The speckle observed in traditional SAR images is greatly reduced in FOPEN SAR image due to the increase in the wavelength of the radiation that causes one dominant scatter to be imaged per cell. The man made targets also change in appearance in the image because of the increased in the wavelength of the radiation used. The dominant target return is generally from the entire body of the target and has the effect that the radar cross section (RCS) of the target is more strongly a function of its orientation [3] .

Experiments were conducted by the Army Research Lab that demonstrated the ability of FOPEN radar to detect a complex target such as vehicle and canonical shapes in heavy foliage [20] . The experiment was limited due to the fact only one vehicle was used, and a comparison of the results with traditional SAR frequencies was not made. The Army Research Lab also demonstrated that lower frequencies (130-330 MHz) could provide sufficient ground penetration to detect buried (6 inches) antitank mines (M-20) where the tradition X band SAR was unable to detect the mines [17] . The experiments did show however, that the lower frequencies used for ground penetration decreased resolution enough that the buried smaller anti-personnel mines (Valmara 69) went undetected. The second experiment was of limited benefit to SAR ATR research because complex targets were not

used and hence impossible to access the effects of classification with frequency.

The best illustration of the differences of SAR imagery with frequency is the development of the model representing a conventional size trihedral at traditional SAR frequency vs SAR radar operating at FOPEN or GPEN radar frequency. The conventional sized trihedral are important in SAR imagery because they are used in the calibration of SAR systems and many complex targets can be approximated as a sum of trihedral and dihedral scatters.

For traditional SAR frequencies which include X, C, and L bands (in GHz range) the mathematical model developed to represent the conventional sized trihedral are based on the geometric theory of diffraction (GTD) [15] . The GTD allows the representation of a complex object as the sum of individual scattering centers (SC's). The GTD says if the wavelength of the radar radiation is small relative to the extent of the object, then the reflected radiation can be well approximated as contributions from electrically isolated scattering centers.

Now lets outline the mathematical model developed by Gerry, et. al. in 1999 [15] , which will provide representation of an object scattering center using frequency and aspect angle of the radar and parameters of the target. The radar position will be defined by the aspect angle ϕ, which is defined counterclockwise from the x (range) axis. The mathematical model will not only use GTD but will also assume far zone backscattering of the radar wave, which means the incident radar wave, will assume to be planar when it reaches the target. For developing the mathematical model using the GTD under the far zone backscattered field assumption, we need to make three more assumptions.

The first assumption is that the received radar wave of a far field scattering center (SC) shows linear phase dependence, that is the phase of a SC at a given aspect angle is only a function of the position of the SC. The assumption has the affect of excluding the effect of disperse scattering mechanism such creeping waves and resonant cavities. The backscattered radiation for the nth scattered can be defined as

$$E_n^s(k, \phi) = S_n(k, \phi) \exp \left[j2k(\vec{r}_e \cdot \vec{r}_n) \right] \tag{2.240}$$

where $k = \frac{\omega}{c}$ is the wave number and $\vec{r}_e$ is the unit vector in the direction of scattering field as well as $\vec{r}_n = (x_n, y_n)$ is the position of nth SC (target) projected to the image plane. In the development of this and all other equations, the term $\exp(j\omega t)$ is assumed in the equation and is suppressed for convenience.

The second assumption is that the amplitude of the received radar wave depends on frequency. This assumption is govern by the high frequency approximation given by GTD. Using the above assumption, and a conservation of energy argument, it can be shown that the amplitude of the backscattered radiation as function of frequency for many different types of geometries can be approximated as

$$(jk)^\alpha \tag{2.241}$$

when $\alpha = 1$ for flat plates at broadside or dihedral; $\alpha = \frac{1}{2}$ for singly curved surface reflection; $\alpha = 0$ for point, sphere, or straight edge; $\alpha = -\frac{1}{2}$ for edge diffraction; and $\alpha = -1$ for corner diffraction.

The last assumption is that the amplitude dependence of the received radar wave on aspect angle can be characterized either as spatially distributed or localized. A localized SC, which includes trihedral corners and edge diffraction, can be assumed to be a point source in space with slowly varying amplitude as the aspect angle changes. The slowly varying SC's can be modeled with a damped exponential. Using some physical insight a mathematical model was developed and can be written as

$$S_n(f, \phi) = A_n \exp\left(-\omega\gamma_n \sin\phi\right) \tag{2.242}$$

where γ_n is an empirical quantity with no physical interpretation. Distributed SC's, which include dihedrals, and cylinders, can be assumed to vary with aspect angle approximately equal to the sinc function. A distributed SC can be represented as

$$S_n(f, \phi) = A_n \operatorname{sinc}\left(\frac{\omega}{c} L_n \sin(\phi - \phi_n)\right) \tag{2.243}$$

where L_n is the length and ϕ_n is the orientation angle of the scatter. Combing the two types of scattering mechanisms form the complete model for an individual scattering center and can be written as

$$
\begin{aligned}
E_n^s(k, \phi) \;=\; & A_n \cdot \left(j\frac{\omega}{\omega_c}\right)^{\alpha_n} \operatorname{sinc}\left(\frac{\omega}{c} L_n \sin(\phi - \phi_n)\right) \exp\left(-\omega\gamma_n \sin\phi\right) \\
& \exp\left[j\frac{2\omega}{c}(x_n \cos\phi + y_n \sin\phi)\right]
\end{aligned} \tag{2.244}
$$

where $L_n = 0$ if the SC is localized and $\gamma_n = 0$ if the SC is distributed. The total radar return is simply the summation of the individual SC for the total of P scattering centers

$$E^s(k, \phi) = \sum_{n=1}^{P} E_n^s(k, \phi). \tag{2.245}$$

Now for convenience, we shall take the mathematical model from the frequency aspect domain to the image domain using the 2-D inverse Fourier transform. This can be done in four steps. The first step in the transformation is to use some approximations to simplify the amplitude dependence functions by using the approximation

$$k^{\alpha_n} \approx \exp(-\omega r_n) \tag{2.246}$$

where r_n is an estimated damping factor. Then we let the term j^{α_n} be included in the complex amplitude A_n. The second step involves changing the polar coordinates of the model into Cartesian coordinates using the transform

$$\omega_x = \omega\cos\phi \qquad \text{and} \qquad \omega_y = \omega\sin\phi. \tag{2.247}$$

The transformation assumes the data is sufficiently narrow bandwidth that simple interpolation to rectangle grid is possible or in other words with small angle spans, $\omega r_n \approx \omega_x r_n$. The third step involves using window functions in the frequency and aspect

angle domain to suppress side lobes (similar to the digital spotlighting). The window functions are assumed separable and can be written as

$$W(\omega_x, \omega_y) = W_x(\omega_x)W_y(\omega_y) \tag{2.248}$$

where

$$W_x(\omega_x) = \sum_{p=1}^{P} B^x(p) \exp(j\omega_x p)$$

$$W_y(\omega_y) = \sum_{q=1}^{Q} B^y(q) \exp(j\omega_y q)$$

are the window functions which can be Hamming, Taylor, or rectangular functions. The last step in the transformation is using the 2-D inverse Fourier transform to move into the image domain

$$
e_n^s(t_x, t_y) = \int_{\omega_{x1}}^{\omega_{x2}} \int_{\omega_{y1}}^{\omega_{y2}} A_n \sum_{p=1}^{P} \sum_{q=1}^{Q} B^x(p) B^y(q) \operatorname{sinc}\left(\frac{L_n \cos \phi_n}{c}(\omega_y - \omega_x \tan \phi_n)\right)
$$
$$
\exp\left(\omega_y[-\gamma_n + j(\frac{2y_n}{c} + q + t_y)]\right)
$$
$$
\exp\left(\omega_x[-r_n + j(\frac{2x_n}{c} + p + t_x)]\right) d\omega_x d\omega_y \tag{2.249}
$$

where ω_{x1} and ω_{x2} are first and last frequencies of ω_x and likewise for ω_y. Now the equation can be solved for a trihedral using the fact that the trihedral is a localized scatter, that is $L_n = 0$,

$$
e_n^s(t_x, t_y) = A_n \sum_{p=1}^{P} \sum_{q=1}^{Q} B^x(p) B^y(q) \exp\left(\omega_{yc}[-\gamma_n + j(\frac{2y_n}{c} + q + t_y)]\right)
$$
$$
\cdot \exp\left(\omega_{xc}[-r_n + j(\frac{2x_n}{c} + p + t_x)]\right)
$$
$$
\cdot \operatorname{sinh} c\left(\frac{\Omega_x}{2}[-r_n + j(\frac{2x_n}{c} + p + t_x)]\right)
$$
$$
\cdot \operatorname{sinh} c\left(\frac{\Omega_y}{2}[-\gamma_n + j(\frac{2y_n}{c} + q + t_y)]\right) \tag{2.250}
$$

where

$$
\Omega_x = \omega_{x2} - \omega_{x1} \quad \text{and} \quad \Omega_y = \omega_{y2} - \omega_{y1}
$$
$$
\omega_{xc} = \frac{\omega_{x2} + \omega_{x1}}{2} \quad \text{and} \quad \omega_{yc} = \frac{\omega_{y2} + \omega_{y1}}{2}
$$

$$\mathrm{sinh\,c}(x) \quad = \quad \frac{\sinh(x)}{x}.$$

Although the above model provides results that agree very well for data collected at traditional SAR frequencies, the model quickly diverges when the data is collected using FOPEN and GPEN radar frequencies. The FOPEN and GPEN radars operate at frequencies in the VHF or low UHF ranges (MHz range) and use a wide-bandwidth radar pulse to achieve the desired resolution at the lower frequencies. The model just developed which serves as a basis for multiple SAR ATR algorithms makes use of the narrow frequency bands and the small wavelength of the radar wave to image the conventional size trihedral. Neither of these assumptions are true for the FOPEN or GPEN cases. The conventional size trihedral can no longer be modeled using the GTD. The received radar pulse must be modeled using numerical algorithms such as method of moments (MOM). The modeling of the trihedral is further complicated by the fact that the wavelength of the VHF and low UHF radiation is so large compared to conventional sized trihedral that the ground–air interference can no longer be separated from the individual trihedral. This should also provide major problems with complex objects consisting of multiple interfering structures.

The development of the mathematical model for the received radiation from a conventional size trihedral begins with some nasty electromagnetic equations [14] . Lets begin by writing the equation for the electric field in spatial location $r = (x, y, z)$ produced by a surface current at a different spatial location $r' = (x', y', z')$ as follows:

$$E(r) = \left[-j\omega\mu(r)I + \frac{1}{j\omega\varepsilon(r)}\nabla\nabla \right] \cdot \int_{S'} G(r, r')J(r')dS' \qquad (2.251)$$

where $E(r)$ is the electric field at spatial location r, $J(r')$ is the surface currents produced at r', I is the unit dyadic, $\mu(r)$ is the permeability, $\varepsilon(r)$ is the permittivity of the inhomogeneous background, and $G(r, r')$ represents the dyadic Green's function for the background medium. Now lets assume the 3-D trihedral is a perfect electric conductor (PEC) and also assume far zone backscattering. The electric currents induced on the surface of a PEC trihedral can be solved by MOM techniques. In the case of the electric field in free space, the following simplifications can be made:

$$\mu(r) = \mu_0, \quad \varepsilon(r) = \varepsilon_0$$

and

$$G(r, r') = (xx + yy + zz)\frac{\exp(-jk_0|r - r'|)}{4\pi|r - r'|}. \qquad (2.252)$$

Then a triangular patch discretization of $J(r')$ is performed. The nonzero elements of $G(r, r')$ can now be represented as a Sommerfield integral, which has the form

$$f(\xi, z, z') = \frac{1}{2\pi} \int_0^\infty \hat{f}(k_p, z, z')J_0(k_p\xi)k_p dk_p$$

where $\xi = \sqrt{(x - x')^2 + (y - y')^2 + (z - z')^2}$. The developed equation has the solution

48

kernels, which in themselves are highly oscillatory. The numerical solution of the equation can be formed using the Weyl identity, which is

$$\frac{\exp(-jkR)}{4\pi R} = \frac{1}{2\pi} \int_0^\infty \frac{1}{j2k_z} \exp[-jk_z h(z, z')] J_0(k_p \xi) k_p dk_p \qquad (2.253)$$

where

$$k = \sqrt{k_p^2 + k_z^2} \quad \text{and} \quad R = \sqrt{(x - x')^2 + (y - y')^2 + h^2(z - z')}.$$

Now assume the soil can be represented as a general layered medium, so we can approximately evaluate the integral for a source observed in layer i by

$$\begin{aligned}
\hat{f}(k_p, z, z') &= \frac{\exp\left[-jk_{zi} g(z, z')\right]}{j2k_{zi}} \hat{h}(k_p) \qquad (2.254) \\
&= \frac{\exp\left[-jk_{zi} g(z, z')\right]}{j2k_{zi}} \left[\lim_{k_p \to \infty} \hat{h}(k_p) + \sum_{m=1}^{M} a_m \exp(-k_{zi} b_m) \right]
\end{aligned}$$

where a_m and b_m are estimated along appropriate line in complex k_{zi} plane using Prony's method. The above method is applied separately for each components of the Green's function dyadic. Then by placing (2.254) into the Sommerfield equation in terms of sum of components where each component can be integrated in closed form.

The problem of SAR ATR using FOPEN frequencies has been preliminarily attacked using simple scattering physics [2] . The approach uses computational electromagnetic algorithms to generate signatures and match filter banks to span the target space. The FOPEN SAR ATR problem posses special problems due to the fact that at FOPEN frequencies objects are made up of few scatters which vary usually with angle or polarization.

The first stage of the algorithm by Mark R. Allen in 1996 deals with the detection of man–made targets from clutter. The initial detection stage models all man–made targets as a long principle dihedral formed between the side of target and the ground. The radar response of a dihedral at FOPEN is a single narrow peak in azimuth angle whose power varies according quadratic function of frequency with polarization response of $HH = VV$ and zero cross polarization. The result of this is a line segment in the SAR image whose length is proportional to the physical length of the object. The phase of this line will be a bi-linear function whose slope depends on the relative orientation of the radar to the target. Non-man made objects, such as tree trunks, are modeled as lossy vertical cylinders, which has an RCS that is a uniformly distributed function in azimuth angle. The assumption causes the trees to appear as point like responses in the SAR images. The stage is performed by the matched filter image formation (MFIF) subunit. MFIF uses matched filters constructed from computational electromagnetics spanning various azimuth angles to search each pixel in the test image.

The second stage is formed by the complex spatial matched filtering (CSMF) subunit. The second stage uses the same model as the first stage but is designed to match all pixels in the image corresponding to the target rather than one pixel at a time. The CSMF subunit uses

the computational electromagnetic calculated signatures from various dihedrals at various orientations. The actual identification is performed through a successive level of recognition using greatest likelihood test. The process so far has only been presented in theory with no published testing of the algorithm using real or simulated data.

There are several more papers dealing with SAR imaging formation, enhancement and modeling with ultra–wide bandwidth FOPEN radar signal [32] [35] [42] and [45] . In the sense of parametric study, those paper address the problems and modeling techniques associated with radar signals in large frequency variation (wide bandwidth and very low frequency). Mostly, we just view them as other type of radar signal. However, the changing in modeling and imaging formation techniques discussed in those paper can help as understanding the effects of frequency variation. There is another set of paper collections dealing with target detections using ultra–wide bandwidth (UWB) FOPEN radar [7] [23] [34] and [47] . Those papers discussed detection of targets in foliage or under ground using UWB radar. Those papers utilizing the frequency variation to detect targets, however none of them addressing the ATR problems. In conclusion, we have not found any research paper to deal with ATR performance under the influence of radar frequency variation. However, some of the paper discussed affects of frequency variation in image formation that may have some indirect link to the performance of an image based ATR algorithms.

2.2.2   Polarization

Another sensor parameter which has an enormous effect on the SAR image, is the polarization used for the radar pulse. The polarization of the electromagnetic radiation used by the radar affects how the geometry of the object will scatter back the radiation from the radar.

The polarization of the radar pulse as well as the received wave can take on numerous forms. The radar system for MSTAR uses HH polarization, which means the transmitted radar wave is horizontally polarized and the receiver radar will record reflected horizontally polarized radiation. A SAR system can be set up to use HH, HV, VH, VV, or even a combination of polarizations. The use of multiple polarizations clearly has a beneficial effect on SAR ATR systems by increasing the amount of information that the radar receives from the scene. When all polarizations are used to form the image, the object in the imaging scene become clearer, and the edges become sharper because the data from HH and HV polarizations, for example, fill in the areas of objects and edges that do not register in the VV polarized data. The potential benefits of using data with multiple polarizations seem to be striking but largely ignored in the published SAR ATR literature.

The mathematical modeling of polarization seems to always attack the problem by using the general equations and vectorizing them to include multiple polarizations. The mathematical models developed earlier for Spot and Strip SAR can be modified to include multiple polarizations by simply using matrices and vector in the pervious equations with the justification that the equations were developed without knowledge of the polarization used. So defining one equation as HH polarization, a second equation for VV polarization can be defined with the same form because polarization was never mention as a parameter.

The biggest and most complete work that was found in the public SAR ATR literature using polarization was from Lincoln Laboratory. Lincoln Laboratory used their SAR ATR algorithm to evaluate targets imaged at a single HH polarization verses targets imaged using three polarizations (HH, HV, VV) [30] . The three polarizations were combined using a Polarimetric whitening Filter (PWF). The PWF uses a polarimetric method to reduce large amount of speckle in the image that is cause by the coherent nature of the imaging process while maintaining resolution of the image [29] .

The PWF process begins with the mathematical modeling of the polarimetric radar return from clutter. The polarimetric radar measurement vector can be represented as

$$Y = \begin{pmatrix} HH \\ HV \\ VV \end{pmatrix} = \begin{pmatrix} HH_i + jHH_q \\ HV_i + jHV_q \\ VV_i + jVV_q \end{pmatrix} \tag{2.255}$$

where for example HH_i and HH_q are the in-phase and quadrature components of the received complex HH signal. The return model assumes a non-Gaussian product clutter model [29] . The assumption implies Y is the product of a complex Gaussian vector X that represents the speckle and a spatially varying texture variable g, which gives

$$Y = \sqrt{g} \cdot X. \tag{2.256}$$

The probability density function of the x is given by

$$f(X) = \frac{1}{\pi^3 |\Sigma|} \exp\left(-X^\dagger \Sigma^{-1} X\right) \tag{2.257}$$

where Σ is the polarization covariance matrix and X has zero mean. The covariance matrices used in the development were defined as

$$\Sigma = \sigma_{HH} \begin{pmatrix} 1 & 0 & \rho\sqrt{\gamma} \\ 0 & \varepsilon & 0 \\ \rho^*\sqrt{\gamma} & 0 & \gamma \end{pmatrix} \tag{2.258}$$

where

$$\sigma_{HH} = E\left\{|HH|^2\right\} \quad \text{and} \quad \varepsilon = \frac{E\left\{|HV|^2\right\}}{E\left\{|HH|^2\right\}}$$

$$\gamma = \frac{E\left\{|VV|^2\right\}}{E\left\{|HH|^2\right\}} \quad \text{and} \quad \rho = \frac{E\left\{HH \cdot VV\right\}}{\sqrt{E\left\{|HH|^2\right\} \cdot E\left\{|VV|^2\right\}}}.$$

The product multiplier g used in the development of the PWF is modeled as a gamma distributed random variable. Although the authors mentioned the possibility of using log normal or Weibul distributions, the use of the Weibul distribution would have probably bettered the results. The probability density function (pdf) of the product multiplier with a

gamma distribution is given by

$$f_G(g) = \frac{1}{\bar{g}} \left(\frac{g}{\bar{g}}\right)^{\nu-1} \frac{1}{\Gamma(\nu)} \exp\left(\frac{-g}{\bar{g}}\right) \tag{2.259}$$

where $\bar{g} \cdot \nu = E\{g\}$ and $\bar{g}^2 \cdot \nu(\nu+1) = E\{g^2\}$. The gamma distribution assumption causes the pdf of the return vector to become a modified Bessel function or more specifically a K–distribution function that represented by

$$f(Y) = \frac{2}{\pi^3 \bar{g}^\nu \Gamma(\nu)|\Sigma|} \cdot \frac{K_{3-\nu}\left(2\sqrt{\frac{Y^\dagger \Sigma^{-1} Y}{\bar{g}}}\right)}{\left(\bar{g} Y^\dagger \Sigma^{-1} Y\right)^{\frac{(3-\nu)}{2}}}. \tag{2.260}$$

Now that Y has been developed, the return vector must be processed to get maximum pixel intensity while minimizing speckle. The speckle can be measured as the ratio of the standard deviation of the image pixel intensities to the mean of the intensities, that is

$$\frac{s}{m} = \frac{\text{st. dev. of } y}{\text{mean of } y} \tag{2.261}$$

where y is a random variable represents pixel intensity. So we need to find a process (A) that can construct the best image possible from the three polarized images collected. In other words we want to construct the image from the quadratic

$$y = Y^\dagger A Y = g X^\dagger A X \tag{2.262}$$

where A is a weighting matrix assumed to be Hermitian symmetric and positive definite. The determination of A involves the minimization of $\frac{s}{m}$ for a given mean value of the pixel intensity. The solution to this is based on the following derived relations

$$E\left\{X^\dagger A X\right\} = tr\left(\Sigma \cdot A\right) = \sum_{i=1}^{3} \lambda_i \tag{2.263}$$

$$Var\left\{X^\dagger A X\right\} = tr\left(\Sigma \cdot A\right)^2 = \sum_{i=1}^{3} \lambda_i^2 \tag{2.264}$$

where $E\{\cdot\}$ is the expectant value, $Var\{\cdot\}$ is the variance and $\lambda_i, i = 1, 2, 3.$ are the eigenvalues of the matrix $\Sigma \cdot A$. Combining equations (2.261), (2.262), (2.263), and (2.264) gives

$$\left(\frac{s}{m}\right)^2 = \frac{Var\{y\}}{E^2\{y\}} = \frac{\nu+1}{\nu} \cdot \frac{\sum_{i=1}^{3} \lambda_i^2}{\left(\sum_{i=1}^{3} \lambda_i\right)^2} + \frac{1}{\nu}. \tag{2.265}$$

52

Since ν is constant, we can minimize the ratio by minimizing the term

$$\frac{\sum_{i=1}^{3} \lambda_i^2}{\left(\sum_{i=1}^{3} \lambda_i\right)^2}. \tag{2.266}$$

Now if we assume eigenvalues $\lambda^T = [\lambda_1, \lambda_2, \lambda_3]$ is a minimized solution, then so is $\alpha\lambda^T$ which means we can achieve minimization by minimizing the numerator with the constraint that the denominator is equal to one. The numerator can now be minimized using a Largrange multiplier β, that is, to minimize the following function of λ:

$$f(\lambda) = \sum_{i=1}^{3} \lambda_i^2 + \beta \left(1 - \left(\sum_{i=1}^{3} \lambda_i\right)^2\right). \tag{2.267}$$

The minimization can be accomplished by taking the partial derivative of $f(\lambda)$ with respect to λ_i and setting them equal to zero

$$\frac{\partial f(\lambda)}{\partial \lambda_i} = 2\lambda_i - 2\beta \sum_{i=1}^{3} \lambda_i = 0, \quad \text{for } i = 1, 2, 3. \tag{2.268}$$

The minimizing solutions are

$$\lambda_i = \beta \cdot \sum_{i=1}^{3} \lambda_i, \quad \text{for } i = 1, 2, 3. \tag{2.269}$$

that implies $\lambda_1 = \lambda_2 = \lambda_3$. This means the weighting matrix A^* should be chosen such that the eigenvalues of matrix $\Sigma \cdot A$ are equal which implies the minimizing solution is

$$A^* = \Sigma^{-1}. \tag{2.270}$$

The whitening process can now be represented as

$$W = \Sigma^{-\frac{1}{2}} Y = \sqrt{g}\Sigma^{-\frac{1}{2}} X \tag{2.271}$$

where W has elements which are independent complex random variables and their covariance matrix is an identity matrix. The single image is formed and the optimal solution is obtained by simply noncoherently summing the powers of W. The entire process can be thought as converting the received data (HH, HV, VV) to the new basis given by

$$W^T = \left[HH \qquad \frac{HV}{\sqrt{\varepsilon}} \qquad \frac{VV - \rho^*\sqrt{\gamma}HH}{\sqrt{\gamma(1 - |\rho|^2)}} \right] \tag{2.272}$$

and then summing up the three new components in the new basis to form the image

$$y = W^2(1) + W^2(2) + W^2(3). \tag{2.273}$$

Lincoln Laboratory used PWF in testing their algorithm with different polarizations [30] . The data consisted of two vehicles (Howitzer and a Tank) and clutter data consisting of no targets imaged with HH polarization and using multiple polarizations combined into a single image with PWF. The PWF data resulted in a slight increase in tank identification and decrease in tank mis–identification.. The PWF data showed a large increase in the correct identification of the Howitzer while decreasing the mis–identified Howitzers. The most stunning effect was the 90% decrease in clutter being misidentified as targets. Although only two targets were used, the results were very interesting. The technique should provide an increase in all SAR ATR algorithms, which use the SAR image or features derived from the SAR image identification.

A new and developing area of research into polarization and ATR is the exploration in choosing the best transmit and receive polarization states for each target to improve identification [40] . The use of different polarizations states for each target class can provide maximum separate on target classes and maximize the performance of ATR algorithm.

The mathematical model describing the polarizations is first developed [40] . An arbitrary electromagnetic wave can be completely characterized by specifying its wavelength, phase, amplitude and polarization. We will assume the electric and magnetic components of the wave are perpendicular to direction of propagation, and the tip of the electric field vector E will trace out an ellipse in a plane whose geometrical properties are given by ellipticity $\mathcal{X}$ whose value is equal to the angle between the major axis and a line joining the points on the ellipse of the major and minor axis, and the ellipse orientation angle Ψ whose value is equal to the angle between the major axis and the horizontal axis. The polarization of an EM wave can also be represented using stokes vector

$$F = \begin{pmatrix} I_0 \\ Q \\ U \\ V \end{pmatrix} = \begin{pmatrix} I_0 \\ I_0 \cos(2\Psi)\cos(2\mathcal{X}) \\ I_0 \sin(2\Psi)\cos(2\mathcal{X}) \\ I_0 \sin(2\mathcal{X}) \end{pmatrix} \tag{2.274}$$

where I_0 is the intensity of the wave. The values Q, V, U are called stoke parameters and are related by

$$I_0^2 = Q^2 + V^2 + U^2. \tag{2.275}$$

The response of a target from an incident radar wave can be represented by the polarimetric scattering matrix

$$\begin{pmatrix} E_{sh} \\ E_{sv} \end{pmatrix} = \begin{pmatrix} S_{hh} & S_{hv} \\ S_{vh} & S_{vv} \end{pmatrix} \begin{pmatrix} E_{ih} \\ E_{iv} \end{pmatrix} \tag{2.276}$$

where E_s and E_i are the scattering and incident waves respectively. S matrix is the scattering coefficients for a given orientation of transmitting and receiving. The knowledge of the scattering matrix allows the calculation of the response of the target to any incident polarization wave. Instead of limiting ourselves to only horizontal and vertical polarization, we can use the technique of polarization synthesis to model the response of the target to signals with polarization specified by $\mathcal{X}$ and Ψ. This can be done by the use of a Mueller

Matrix

$$M = RWR^{-1} \tag{2.277}$$

where W is a complex matrix

$$W = \begin{pmatrix} S_{vv}^* S_{vv} & S_{vh}^* S_{vh} & S_{vh}^* S_{vv} & S_{vv}^* S_{vh} \\ S_{hv}^* S_{hv} & S_{hh}^* S_{hh} & S_{hh}^* S_{hv} & S_{hv}^* S_{hh} \\ S_{hv}^* S_{vv} & S_{hh}^* S_{vh} & S_{hh}^* S_{vv} & S_{hv}^* S_{vh} \\ S_{vv}^* S_{hv} & S_{vh}^* S_{hh} & S_{vh}^* S_{hv} & S_{vv}^* S_{hh} \end{pmatrix}. \tag{2.278}$$

In which, S_{tr} are the complex scattering coefficients defined in (2.276), t denotes transmit orientation and r denotes the received orientation. And the complex matrix

$$R = \begin{pmatrix} 1 & 1 & 0 & 0 \\ 1 & -1 & 0 & 0 \\ 0 & 0 & 1 & 1 \\ 0 & 0 & -j & j \end{pmatrix}. \tag{2.279}$$

With the Mueller matrix, the radar cross section (RCS) for any scatter at any polarization can be expressed as

$$\Sigma_{rt} = 4\pi F_r \pi F_t. \tag{2.280}$$

Using the above equations, it should be possible to pick the polarization that will produce the largest separation between two given test objects. The problem can be stated as seeking the feature vector x which maximizes the distance $J(f)$ between elements of c classes. The distance is defined as

$$J(f) = \frac{1}{2} \sum_{i=1}^{c} P_i \sum_{j=1}^{c} P_j \frac{1}{n_i n_j} \sum_{k=1}^{n_i} \sum_{l=1}^{n_j} \delta(f_{ik}, f_{jl}) \tag{2.281}$$

where $\delta(f_{ik}, f_{jl})$ is the distance between two feature vectors f_{ik} and f_{jl} from classes w_i and w_j respectively. n_i and n_j are the numbers of training patterns in classes w_i and w_j respectively. P_i and P_j are their corresponding prior class probabilities which can be estimated by the frequency of occurrence

$$P_i \approx \frac{n_i}{n}. \tag{2.282}$$

The general approach is to find a polarization which will maximize the distance between the targets of separate classes and at the same time minimize the distance for the targets within class. For a target class model in polarization orientation angles $(\mathcal{X}, \Psi)$, the angles can change from 0 to 2π. For reducing the computational burden, 8 levels of quantization for each angle are used. Therefore, there are 64 samples in each target class model for all the polarization orientations. For each target class with n samples, the total number of distances needed to be computed is $\frac{n(n-1)}{2}$. For c number of classes, the number is quickly leads

to a vary high computational burden: $\frac{c \cdot n(c \cdot n - 1)}{2}$ distance calculations and searching the minimum and maximum results.

The works in [29] , [30] , and [40] show the applications of using polarization to enhance the appearance of SAR image and to classify/recognizing target. There are couple more works using polarization in detecting target [59] and [41] . In conclusion, RCS's of scatters at different transmit and received polarization orientations show great variations depending on the geometric shape of targets. It should have great impact on the performance of image based ATR algorithms. However, the research in this area is very limited.

2.2.3   Squint

Compared with SAR in broadside mode, SAR in squint modes produces variations in phase, range migration, Doppler centroid, and azimuth bandwidth. Those variations must be taken care of in the imaging formation algorithms for best performance. The changes in squint angle will certainly produce variations in SAR images and in the performance of ATR. There are many variations, that some of the basic ones have been explained in the brief section, in squint mode SAR imaging processing algorithms. However, there are no prior work to address the change of image quality or ATR performance due to the squint angle variation. We did come across several interesting papers. The work in [9] has compared a number of squint image algorithms under the narrow–bamdwidth and narrow–beamwidth assumptions. Their results show that at a larger squint angle, their more efficient real–time SAR imaging algorithms only produce a slight degradation (in azimuth resolution) compared with conventional stripmap SAR at a large squint angle. Sun etc. [48] developed a new approach to process high squint SAR imagery referred to as time varying step transform (TVST) algorithm. Compared with conventional squint angle imaging algorithm, the TVST algorithm produces SAR images with higher azimuth resolution at the large squint angles of $30°, 40°, 60°$. It also ensures the SAR image has uniform resolution and uniform distribution in azimuth independent of the chirp rate variation of the radar signal. The good performance of TVST algorithm comes with a price of slightly increased computational load. Another related work [12] proposed a new conical geometric reference system to solve the data focus problem when there are slight instability in squint angle ($< 5°$) during data acquisition.

The work developed by Hanle [16] address the mathematically model of the affects of squint angle on the polarimetric response of targets. The collection of data in squint mode causes variation in the polarimetric response of targets, which need to be taken into account for maximum SAR ATR performance. An Antenna manufactured to transmit and receive vertical and horizontal polarized waves at broadside will produce polarized wave that vary differently and are in some cases non-orthogonal at off broadside directions. Let the matrix M represent the measured matrix of a target off broadside and more specifically

$$M = A_r \cdot Z \cdot A_t \tag{2.283}$$

where Z is the target polarization response at broadside, A_r is the antenna transformation matrix modeling receiving, and A_t is the antenna transformation matrix modeling transmitting. Now if we assume the use of a monostatic radar and that the transmit and

receive orientations are the same, the following simplification can be made $A = A_r = A_t$. For the development of the rest of the mathematical equations, we note that the matrix A can be represented by a directional projection matrix F, a gain factor d^2, and a supplemental matrix. The supplemental matrix is a function of the squint angle β, azimuth angle (divergence angle) α, depression angle γ, and elevation angle ε. The variables can be shown to have the following relations:

$$\sin \beta = \sin \alpha \cos \varepsilon \quad \text{and} \quad \gamma = -\varepsilon. \tag{2.284}$$

The gain factor is defined by

$$d^2 = \cos \theta = \cos \alpha \cos \varepsilon \cos \delta + \sin \varepsilon \sin \delta \tag{2.285}$$

where θ is the off broadside angle and δ is the angle between the antenna horizon to the broadside. The polarimetric matrix of the return from broadside using a uniformly emitting planar array with well-matched elements can be represented by

$$F = \begin{pmatrix} a_h & b_v \\ -b_h & a_v \end{pmatrix} = \begin{pmatrix} a_v & b_v \\ -b_v & a_v \end{pmatrix} \begin{pmatrix} a_d & 0 \\ -b_d & 1 \end{pmatrix} \tag{2.286}$$

where

$$b_h = \frac{1}{\sqrt{1 + o_h^{-2}}} \quad \text{and} \quad b_v = \frac{1}{\sqrt{1 + o_v^{-2}}}$$

$$a_h = \sqrt{1 - b_h^2} \quad \text{and} \quad a_v = \sqrt{1 - b_v^2}$$

with $o_h = \tan \alpha \sin \varepsilon$ and $o_v = \tan \alpha \sin \delta$. The projection matrix can incorporate squint angle effects through the introduction of the rotation matrix in (2.286)

$$\begin{pmatrix} a_d & 0 \\ -b_d & 1 \end{pmatrix}$$

where $a_d = a_h a_v + b_h b_v$ and $b_d = b_h a_v - a_h b_v$. Now we can recover the target matrix Z from the measurement M by the polarization matrix A which is formed by the projection matrix F and a few other parameters.

$$M_c = A^{-T} M A^{-1} \approx Z \tag{2.287}$$

2.2.4   Depression Angle

Depression angle is the sensor parameter that determines how the electromagnetic scattering from the three–dimensional object will project to the two–dimensional SAR image plane. The variation of depression angle has dramatic effects on the appearance of real targets in the SAR image. The depression angle is defined as the angle between the radar and the image plane. Since in most of SAR imaging algorithms the signal processing is performed on a slant

plane, the depression angle is assumed to be fixed at a given angle. Variation of depression angle is probably the most widely studied of all of the sensor parameters. Some image based SAR ATR algorithm published has performance evaluation run on the data collected from different depression angle. All of the ATR algorithms showed significant degradations in performance when depression angle was changed. However, due to the limited availability of data on different depression angles. For example, the MSATR database only have data sets with two different depression angles. There are no systematic study of depression angle variations to quantify the level of degradation in ATR performance.

2.2.5   Motion Compensation

In order to form high-resolution SAR images, the radar system must correctly integrate the coherent radar returns at each synthetic aperture position. The success of this process relies on compensating the system to account for all possible cases of phase variation except those caused by the imaged scene. Phase error can be introduced through the movement of the sensor on the collection platform by more than a wavelength from the ideal trajectory or from the change in propagation effects of turbulence in the troposphere or ionosphere [10] . Although a number of motion compensation algorithms have been introduced, all of them deal with either keeping better track the position of the sensor or using the collected data itself to estimate phase error [54] . Sensor platform motion compensation algorithm is also referred to as auto focus algorithm. A more detailed discussion of trajectory deviations in sensor platform can be found in [11] .

The Phase Gradient Auto focus (PGA) is currently one of the most widely used motion compensation scheme that uses the data collected to estimate the phase error [54] . The PGA algorithm offers near diffraction–limited restoration, independence of phase error order, immune to high background clutter, and without the need of bright isolated point like reflectors. The PGA algorithm relays the redundancy of the phase error information in the image to generate an estimate of the phase error.

The PGA technique can be divided into four main steps: 1) circular shift; 2) windowing; 3) phase gradient estimation; 4) iterative correction. The PGA algorithm begins with the complex phase degraded SAR image and the phase degradation is independent of the scene content and the image formation process. In fact the only assumption made is that the phase is coherent over the entire image scene. The range compressed phase history domain data can be expressed as

$$F_n(u) = |F_n(u)| \exp\left[j\phi_n(u) + j\phi_\varepsilon(u)\right] \tag{2.288}$$

where n is the nth range bin, u is the position of the synthetic aperture (cross–range), $|F_n(u)|$ is the magnitude, $\phi_n(u)$ is the phase and $\phi_\varepsilon(u)$ is the uncompensated phase error. It is shown that the uncompensated phase error is only a function of aperture position independent of range. It means the uncompensated phase error is common to all range bins and independent of n. Now we can use azimuth compression so that each line of image data is a sum given by

$$\mathcal{F}_{u \to k_u}\left\{F_n(u)\right\} = \sum_m h(k_u) * a_{m,n} S(k_u - k_{um,n}) \tag{2.289}$$

58

where $h(k_u) = \mathcal{F}_{u \to k_u} \{\exp[j\phi_\varepsilon(u)]\}$ is the Fourier Transform of the phase error function, $*$ denotes convolution and $a_{m,n}S(k_u - k_{um,n})$ is the impulse response of the imaged scene.

The first step of the PGA algorithm is to select the strongest scatter a_n in each range bin and shift it to the origin of the Doppler domain k_u. The shifting operation is carried out using a circular buffer where samples shifted off one edge of the range bin is replaced on the opposite edge of the range bin. The process has the effect of removing the frequency offset due to the target k_{un}. The process has the added benefits of improving the signal to noise ratio, aligning regions with subtle contrast changes, and improving the phase estimation of high clutter scenes.

The second step of the PGA algorithm involves windowing the circularly shifted data. The windowing process maintains the degraded point spread function of the dominate scatter in each range bin while removing data unnecessary to phase estimation. The size of the window used to process the information is an important parameter of the algorithm. Auto window sizing makes use of the fact that scatter in each range bin undergoes the identical blurring which means an estimate of the blur can be obtained by averaging the blur over all range bins using

$$s(k_u) = \sum_n |f_n(k_u)|^2 \qquad (2.290)$$

where $f_n(k_u)$ is the circular shifted image data at n^{th} range bin. The function $s(k_u)$ will be maximum at $k_u = 0$ (due to the circular shift) and plateau approximately W in the width of the window. The exact width of the window can be chosen by using automatic amplitude threshold over function $s(k_u)$ with some added safety factor, say plus 50% in width. Since the change of amplitude shape of function $s(k_u)$ reflects the convergence of the iterative focusing correction process, the auto window sizing threshold can be used to evaluation of the speed of convergence of the algorithm.

The third step of the PGA algorithm involves phase gradient estimation. Let $g_n(k_u)$ be the shifted and windowed image data. The Fourier transform of $g_n(k_u)$ is

$$G_n(u) = F_{k_u \to u} \{g_n(k_u)\} = |G_n(u)| \exp[j\theta_n(u) + j\phi_\varepsilon(u)] \qquad (2.291)$$

where $\theta_n(k_u)$ is the scatter dependent phase function for each bin. Now an estimate of the phase error can be generated using the fact that for an arbitrary complex valued function

$$x(u) = |x(u)| \exp[j\psi(u)], \qquad (2.292)$$

the derivative of the function is equal to

$$\frac{dx(u)}{du} = \frac{\text{Im}\{x^*(u)\dot{x}(u)\}}{|x(u)|^2}. \qquad (2.293)$$

Therefore, the weighted least squares estimate of the gradient of the phase error function is

$$\dot{\phi}(u) = \frac{\sum_n \text{Im}\{G_n^*(u)\dot{G}_n(u)\}}{\sum_n |G_n(u)|^2} \qquad (2.294)$$

$$= \quad \dot{\phi}_\varepsilon(u) + \frac{\sum_n |G_n(u)|^2 \dot{\theta}_n(u)}{\sum_n |G_n(u)|^2}$$

The estimated phase error $\phi(u)$ can be obtained by the integral of the estimated gradient function $\dot{\phi}(u)$. The phase error can be removed by simple multiplication of the phase error by $\exp[-j\phi_\varepsilon(u)]$.

The fourth step is simply continuing the phase estimation and correction process until a suitable compensation has been reached. Although the PGA technique is computationally intensive, PGA provides the best overall results.

The PGA algorithm has recently been extended to correct two–dimensional (2–D) phase error [55] . In most cases, 2–D phase error can not be completely corrected by autofocusing algorithms which corrects the phase error in one–dimension (1–D) separately. The PGA algorithm however, can be extended to 2–D to deal with 2–D phase error. The 2–D PGA maintains all of the same advantages as the 1–D case while becoming more robust to the type of error the algorithm can handle.

Phase Retrieval is a second motion compensation method that works directly with the raw data [19] . Phase Retrieval has been designed to deal with 2–D motion error instead motion instability being dependent only on azimuth co-ordinate (1-D) and high frequency error instead of simply low frequency error modeled such as a polynomial. PGA does not generally deal with either error well.

"AutoClean" (Autofocus via Clean) [1] is another newly developed motion compensation algorithm which is mainly for inverse SAR (ISAR) autofocus. The authors claim it performs similarly as PGA algorithm. However, it is slightly better than PGA algorithm for ISAR data where the range migration correction is not available.

Another area of motion compensation is for UWB FOPEN stripmap SAR [8] . The paper surveyed motion compensation algorithms for widebeam SAR data and developed a improved version of motion compensation algorithm for UWB stripmap SAR. The algorithm aimed to deal with the required variations in motion compensation as the function of azimuth beam angle (divergence angle) which is very wide for UWB FOPEN stripmap SAR.

2.2.6   Noise

The noise content of the images used for training and testing has large effects on the performance of SAR ATR algorithms. There are multiple causes of noise in a SAR image and all sources of noise can never be eliminated. Noise in a SAR image must be accounted for in order to maximize the performance of any ATR algorithm. The best way to understand the effects of noise on SAR ATR algorithms is to develop the mathematical model representing noise in the SAR image. We found one prior work [22] that investigated the influence of noise to the performance of a template–based SAR ATR algorithm.

The noise present in a SAR image has been shown to be multiplicative in nature. The SAR image can be thought as being a combination of radiation reflected energy $S_{t.\theta}$ from the desired target type t at a certain azimuth pose angle θ and noise w which is a zero–mean

Gaussian independent identically distributed random variable

$$I(m, n) = S_{t.\theta}(m, n) + w(m, n). \tag{2.295}$$

Although there have been multiple distributions proposed for $w(m, n)$, the mean is always approximately proportional to standard deviation, that is

$$\sqrt{E\left\{[I(m, n) - E\{I(m, n)\}]^2\right\}} = C \cdot E\{I(m, n)\} = C \cdot S_{t.\theta}(m, n) \tag{2.296}$$

where $C = \sqrt{E\{w^2\} - 1}$ which depends on the shape of the distribution chosen. The noise in SAR images has been shown to best fit a Weibull distribution that is approximately Rayleigh. A Rayleigh distribution arises from diffuse scattering, which comes about from a large number of similar strength isotropic reflectors. The noise calculated from pixels in the target area has been shown to fit a Weibull distribution too, but it also fit a log–nominal distribution. The ability to use two different approximations in the target region is due to the nonisotropic scattering mechanism, which are caused by aspect angle variation, or in other words, caused by unstable pixels in the target. The ability to use two different models for the noise distribution over target pixels explains why different statistical based approaches to SAR ATR yield approximately the same results.

The mathematical models for the noise can be written as

$$P\{I(m, n)\} = \frac{c}{b(m, n)} \left(\frac{I(m, n)}{b(m, n)}\right)^{c-1} \exp\left(\frac{I(m, n)}{b(m, n)}\right)^c u\left(I(m, n)\right) \tag{2.297}$$

using the Weibull probability distribution function where u is the unit step function, c is the shape parameter, and $b(m, n)$ is a scale parameter chosen so that the image has a unity mean. The Weibull probability distribution becomes a Rayleigh distribution when c is set to 2. The log–normal PDF is given by

$$P\{I(m, n)\} = \frac{1}{\sqrt{2\pi} \cdot \sigma I(m, n)} \exp\left[\frac{-1}{2\sigma^2} \ln^2\left(\frac{I(m, n)}{\nu(m, n)}\right)\right] u\left(I(m, n)\right) \tag{2.298}$$

where σ is a shape parameter and $\nu(m, n)$ is scale parameter that is equal to the template $S_{t.\theta}(m, n)$.

The knowledge of the mathematical model representing the noise in an image can be used to better the performance of SAR ATR algorithms. The advantage of modeling the multiplicative noise using a log–nominal distribution is that when the image is converted to the log–magnitude domain the noise becomes additive and Gaussian. For the noise in a Rayleigh distribution, the optimum technique is to apply a quarter power transformation on the image, which causes the noise to become approximately Gaussian but remain multiplicative.

2.2.7   Multi–look/Single look

Many platforms use radar antennas which poses very large beamwidth in the azimuth

direction. The large beamwidth allow targets to be illuminated in the collection cycle for a much longer period of time than is needed to obtain a desired azimuth resolution [46] . Although wider integration angles would increase resolution, the implementation of phase correction or focusing requires the storage of the phase histories of each range bin equal to the length of the synthetic aperture. Modern SAR systems often are limited by the amount of data that can be stored during a given collection cycle. The potential long collection times also allow the formation of several images using smaller sub–apertures of the same scene with a very small change in antenna look angle. In order to compress data collected and reduce speckle, several of the images at different "looks" are combined to form one image [25] . The process of combining the several looks to form one image can be done through a weighting matrix or a weighting vector.

The variation of the target signature using single and multiple looks seem to be absent in the literature. The consensus seems to be that multiple looks provide speckle reduction and more stable target scattering behavior than the one from single look with no real data or experiment to back up the conclusion. One of the few articles dealing with multiple look data and target and clutter behavior used multi–look fully polarimetric data [26] . The article focused on effects of various algorithms that combined the multi–look data into a single image on clutters and targets.

The first process to form multi-look data using a weighting matrix is called the multi-look polarimetric whitening filter (MPWF) in [25] . Consider the following multi–look polarimetric covariance matrix from the fully polarimetric radar measurements $Y = [HH \quad HV \quad VV]^T$

$$\Sigma_Y = \frac{1}{N} \sum_{j=1}^{N} Y_j Y_j' \qquad (2.299)$$

where Y_j is the jth look of sample Y. The speckle model in the multi–look covariance domain is $\Sigma_Y = g\Sigma_X$ due to the fact that the speckle appearing as multiplicative noise $Y = \sqrt{g}X$ (2.256) where X represents speckle. Since the polarimetric radar measurement Y contains energy from target and clutter, we have

$$\Sigma_Y = \begin{cases} \Sigma_{c+t} = \Sigma_c + \Sigma_t & \text{target–plus–clutter} \\ \Sigma_c & \text{clutter class} \\ \Sigma_t & \text{target class} \end{cases} \qquad (2.300)$$

where Σ_c and Σ_t are the covariance matrices of clutter class and target class respectively. However, the covariance matrix of clutter class Σ_c can be calculated from known clutter samples. Using the same process as before $W = \Sigma_c^{-\frac{1}{2}}Y$ (2.271) except the use of the multi-look covariance matrix Σ_Y instead of the individual image sample Y, we can have

$$E_W = \Sigma_c^{-1}\Sigma_Y = g\Sigma_c^{-1}\Sigma_X. \qquad (2.301)$$

If the multi–look data from a clutter area, $E_W = \Sigma_c^{-1}\Sigma_Y = \lambda \cdot I$ is whitened. If the data is from a clutter–plus–target area, $E_W = \Sigma_c^{-1}\Sigma_Y = \lambda \cdot I + \Sigma_c^{-1}\Sigma_t$. This information can be

used to classify targets and clutters by a detection threshold T

$$W = \frac{1}{N} \sum_{j=1}^{N} Y_j^{T*} \Sigma_c^{-1} Y_j = tr\left(\Sigma_c^{-1} \Sigma_Y\right) = \begin{cases} > T & \text{target} \\ < T & \text{clutter} \end{cases} . \tag{2.302}$$

W is a single image formed by the multi–look polarimetric data with clutter suppression..

The second process to form multi–look data using a weighting matrix is called the total Power (Span) detector [26] . The total Power detector process simply replaces the weighting matrix Σ_c^{-1} used in the MPWF with the matrix

$$A_s = \begin{pmatrix} 1 & 0 & 0 \\ 0 & 2 & 0 \\ 0 & 0 & 1 \end{pmatrix} \tag{2.303}$$

and the remainder of the process is the same as before.

Instead of using a weighting matrix to transform the multi-look covariance matrix Σ_Y into a single image, methods have been developed using a weighting vector. The weighting vector process can be represented by

$$W = e^{T*} \cdot \Sigma_Y \cdot e = \begin{cases} > T & \text{target} \\ < T & \text{clutter} \end{cases} \tag{2.304}$$

and it can even be transformed to matrix representation

$$W = tr(\Sigma_e \Sigma_Y) = \begin{cases} > T & \text{target} \\ < T & \text{clutter} \end{cases} \tag{2.305}$$

where $\Sigma_e = e \cdot e^{T*}$ [26] . The process using weighting vectors to develop the combined image from multi-look images is the polarization match detector which is represented by

$$W_0 = e_0^{T*} \cdot \Sigma_Y \cdot e_0 \tag{2.306}$$

where e_0 is chosen by maximizing the equation

$$r = \frac{e_0^{T*} \cdot \Sigma_t \cdot e_0}{e_0^{T*} \cdot \Sigma_c \cdot e_0} \tag{2.307}$$

The maximum value for r turns out to be equal the maximum eigenvalue of the matrix $\Sigma_c^{-1}\Sigma_t$ and e_0 is the corresponding eigenvector. After find e_0, $\Sigma_e = e_0 \cdot e_0^{T*}$ can be used as part of the weighting matrix to form the polarization match detector.

Another multi-look processing technique using weighting vectors is called the max and min power detector [26] . The max and min power detector relies on the assumption that the polarimetric covariance matrix is Hermitian and at least semi-definite positive. The diagonalization of such a matrix will always yield non-negative eigenvalues and orthogonal eigenvectors. The polarization synthesis theory states that the maximum and minimum eigenvalues of the covariance matrix corresponds to the maximum and minimum receptions.

The diagonalization of the polarimetric covariance matrix Σ (2.258) can be represented as

$$\Sigma = D^{T*} \left(\begin{array}{ccc} \alpha_1 & 0 & 0 \\ 0 & \alpha_2 & 0 \\ 0 & 0 & \alpha_3 \end{array} \right) D \tag{2.308}$$

where α_1, α_2, and α_3 correspond to the eigenvalues in the order of maximum to minimum and D consists of the eigenvectors e_1, e_2, e_3 of the matrix Σ. Now we can use

$$\Sigma_i = e_i \cdot e_i^{T*}, \qquad i = 1, 2, 3$$

as stated before the max and min power detector.

The last multi-look processing algorithm is called even and odd bounce [26] . The Algorithm begins by decomposing the polarimetric covariance matrix Σ (2.258) into three components or more precisely:

$$
\begin{aligned}
\Sigma \;=\; & \lambda_1 \frac{\sqrt{\eta}+\xi}{2\sqrt{\eta}} \left(\begin{array}{ccc} \frac{4|\rho|^2\gamma}{(\sqrt{\eta}+\xi)^2} & 0 & \frac{2\rho\sqrt{\gamma}}{\sqrt{\eta}+\xi} \\ 0 & 0 & 0 \\ \frac{2\rho^*\sqrt{\gamma}}{\sqrt{\eta}+\xi} & 0 & 1 \end{array} \right) \\[2mm]
& + \lambda_2 \frac{\sqrt{\eta}-\xi}{2\sqrt{\eta}} \left(\begin{array}{ccc} \frac{4|\rho|^2\gamma}{(\sqrt{\eta}+\xi)^2} & 0 & \frac{2\rho\sqrt{\gamma}}{\xi-\sqrt{\eta}} \\ 0 & 0 & 0 \\ \frac{2\rho^*\sqrt{\gamma}}{\sqrt{\eta}+\xi} & 0 & 1 \end{array} \right) + \lambda_3 \left(\begin{array}{ccc} 0 & 0 & 0 \\ 0 & 1 & 0 \\ 0 & 0 & 0 \end{array} \right)
\end{aligned}
\tag{2.309}
$$

where $\xi = \gamma - 1$ and $\eta = \xi^2 + 4|\rho|^2\gamma$.

The radar return from a complex scene can now be modeled as the non-coherent sum of the returns from three simple targets each having their own scattering matrix as represented above. The first two terms represent orthogonal scattering mechanism to each other and the third term represent diffuse scattering from randomly oriented scatters. The Scattering mechanisms can be determined using Van Zyl's approach which states if real part of ρ is positive then the first matrix appears as odd bounce scattering object with the maximum eigenvalue of this matrix representing the odd bounce power. The opposite is true (even bounce instead of odd), if real part of ρ is negative.

It was presented in [26] that real SAR data was used to derive polarimetric covariance matrix parameters of pure clutter as well as man made buildings. Then using these parameters along with the derived equations for probability of detection and of false alarm, the performance of each method was predicated. The methods of MPWF and the polarization match detector gave the most promising results.

2.2.8   Radar Waveform

Although by far most SAR systems employ chirp signals which have variations in frequency and bandwidth, we found a small amount of research into alternative radar waveforms. The most interesting research in this area deals with random noise waveforms. In the university

of Nebraska, there has been a development of a preliminary FOPEN Ultra-wideband SAR using a random noise waveform [13] , [52] and [53] .

The SAR system uses a random noise signal source that produces zero mean wide sense stationary Gaussian random process with variance σ_n^2. The signal can be represented by

$$S_n(t) = a(t)\cos(\omega_0 + \phi(t)) \tag{2.310}$$

where $a(t)$ is a Rayleigh density, $\phi(t)$ has a uniform density between $[-\pi, \pi]$, and ω_0 is the center angular frequency [53] . The response of the transmit and receive antennas can be represented by their impulse responses $A_t(t)$ and $A_r(t)$ respectively. The signal is then band passed

$$S_b(t) = B_p(t) * S_n(t) \tag{2.311}$$

where $B_p(t)$ is the impulse response of the band pass filter. And the transmitted signal becomes

$$S_t(t) = A_t(t) * S_b(t). \tag{2.312}$$

If the impulse response of the target is modeled with $h(t)$, then the received signal can be represented by

$$\begin{aligned} S_r(t) &= h(t) * A_r(t) * S_t(t) \\ &= h(t) * A_r(t) * A_t(t) * S_b(t). \end{aligned} \tag{2.313}$$

The received signal is then passed through a correlation receiver which does a cross correlation of the received signal with the delayed band pass limited version of the original random signal $S_b(t - \tau)$ which yields

$$\begin{aligned} R_{rt}(\tau) &= S_r(t) * S_b^*(-t) = \int_{-\infty}^{\infty} S_r(t) S_b^*(\tau + t) dt \\ &= h(t) * A_r(t) * A_t(t) * R_{bb}(\tau) \\ &= h(t) * P(\tau) \end{aligned} \tag{2.314}$$

where $P(\tau) = A_r(t) * A_t(t) * R_{bb}(\tau)$ is the point spread function of the system and

$$\begin{aligned} R_{bb}(\tau) &= S_b(t) * S_b^*(-t) = \int_{-\infty}^{\infty} S_b(t) S_b^*(\tau + t) dt \\ &= B_p(t) * S_n(t) * S_n^*(-t) * B_p^*(-t) \\ &= B_p(t) * R_{nn}(\tau) * B_p^*(-t) \end{aligned} \tag{2.315}$$

is the autocorrelation function of the bandpassed random noise. $R_{nn}(\tau)$ is the autocorrelation of the random noise signal before bandpass filtering. The random noise signal waveform provides the advantages of being harder to detect than the chirp signal and harder for third party to interfere and jamming. The system on the whole however is still very preliminary with some significant obstacles still needed to be overcome before wide spread use.

Chapter 3
SAR Parametric Variation Study: Experiment Paradigm and Data Sources

In the literature review, we have discovered that there are many SAR sensor operation conditions will affect the image appearance of targets. Due to the complexity and variations in SAR image formation algorithms, each SAR parameter will have different levels of influences on SAR image formation depending on the underline algorithm used. The performance of the image based ATR algorithms will be affected by the variations of SAR parameters. Due to the large number of radar sensor parameters and limited availability of SAR image data across the dynamics of sensor parametric variations, we could not find any systematic study on SAR sensor parameters and their influences on ATR performance. In order to evaluate the performances of ATR algorithms under various sensor OC's, we need to develop a test and evaluation platform. The test and evaluation platform shall include the basic components such as 1) a set of baseline ATR algorithms; 2) a collection of real or synthetic SAR data under various sensor OC's; 3) an evaluation and scoring system. In this study, we have searched for real experiment data under different sensor OC's. We have also established the capability to generate synthetic radar data for both simple or complicated target model under the prescribed sensor OC's. We also identified and implemented a set of baseline ATR algorithms for the SAR parametric study test and evaluation platform.

3.1   SAR Image Data Sources for Parametric Study

Due to the lack of research into the effects of sensor OC's on SAR ATR in the present literature, it seemed logical to carry out a preliminary experiment trying to quantify how the variation of certain sensor characteristics affects different types of SAR ATR algorithms. The experiment was designed to comply with the basic principles of evaluation of performance of SAR ATR algorithms using extended operating conditions (EOC) [37] . In accordance with EOC evaluation, the SAR imagery will be divided up into individual slots where each slot would represent an individual point in the dimension of the OC. The evaluation of ATR performance due to the variation of the OC's would be done by training the algorithm using one value for the OC and then testing using a data set of the same target imaged with different values for the tested OC.

In order to evaluate SAR ATR with respect to sensor OC's, the experiment first needed SAR imagery, which varied over the sensor operating conditions to be evaluated. For the experiment to be most useful, the SAR imagery should contain the same targets imaged at different depression angles, frequency, polarization, and other parameters chosen for the experiment. The SAR data should also ideally contain different vehicle versions than those used in testing, and even contain confusers.

In this section, we will identify various sources of SAR image data suitable for parametric

study. In general, SAR imagery data can be classified into two broad classes. The first is SAR imagery obtained from real objects, and the second is SAR imagery obtained from simulation. The real SAR imagery is much more desirable, but much more limited due to the cost of collection and the ability to alter the sensor parameters. In this section, we will also cover the methods for SAR data synthesis under various sensor OC's.

3.1.1   Real SAR Image Data Sources

The most common source of real SAR imagery is MSTAR data. The complete MSTAR database was obtained from three different collections done in September 95, November 96, and May 97 [37] . The public release MSTAR data is a subset of the September 95 collection. Sandia National Laboratory using a STARLOS sensor collected the MSTAR data set at Huntsville, Alabama. The MSTAR data was obtained at X band (9.6 GHz), HH polarization, and with a resolution of 1ft. by 1ft. The MSTAR data collected did vary over depression angles. One of the public data sets consisted of targets, which were imaged at depression angles of 15° and 17°. Another data set consists of different targets that were imaged at depression angles of 15° and 45°. The narrow depression angle bandwidth in the first set and the very large separation of depression angles in the second set does not allow to establish a nice quantitative relation between depression angle variation and SAR ATR performance.

SAR imagery has also been collected by the Lincoln Laboratory at MIT [30] . Lincoln Laboratory collected SAR imagery with a Millimeter wave SAR sensor. The SAR data was obtained at 33GHz, with a depression angle of 22.5°, fully polarimetric ka-band, and with a resolution of 1ft by 1ft. The data collected has images of multiple polarization of each target including HH, HV, VV polarizations, but unfortunately the collection contains only two different types of vehicles.

Another source of real SAR imagery is often referred to as the P–3 data [45] . The P-3 data was collected to understand the detection of stationary targets, which are obscured by foliage using SAR [49] . The P-3 data was collected in 1995 by a Navy P-3 aircraft for ERIOM and NAWC at Michigan, California, Maine, and North Carolina. The Navy P-3 radar collection was unique because it used a FOliage PENetrating SAR system. An FOPEN SAR system consists of an ultra wideband (UWB) radar operating at UHF/VHF frequencies. The P-3 radar used a chirp radar pulse with a frequency band of 215 to 730 MHz. The collection involved 33 military vehicles imaged with depression angles of 45°, 30°, and 20° and obtained a resolution of .33 M. The targets were imaged in the open and in foliage consisting of a mix of deciduous and coniferous trees. The SAR image was formed using the omega-K (or Range migration) technique to coherently process wide-band and wide integration angle raw data [49] .

A non-aerial source of SAR data has been collected by the Army Research lab using an ultra wide band (UWB) boom SAR [17] . The SAR radar was connected to a boom of a truck and the truck driven to take SAR measurement. The UWB boom SAR uses a radar pulse with a bandwidth of 40MHz to 1GHz, HH polarization, with a PRF of 750 Hz. The first collection using this radar was performed at the Aberdeen Proving grounds August of 1995.

The collection involved imaging canonical and tactical targets deployed in a deciduous forest of varying density. The second collection was performed at the Yuma Proving Grounds at the steel Crater site. The second collection involved imaging mines, mine simulants, wires of various gauges, pipes of various diameters, and 55 gallon drums to represent military targets, along with other environmental and commercial interests.

3.1.2   Simulated SAR Imagery

The lack of any real data meeting all of these requirements has forced us to use simulated data in the preliminary experiment. The most widely used general-purpose radar signature prediction code is XPATCH [50] . XPATCH calculates high frequency electromagnetic scattering from complex objects based on high frequency shooting and bouncing-ray technique. XPATCH allows the generation of SAR imagery while specifying many of the sensor characteristics of interest. The XPATCH code has been rigorously tested against actual radar measurements.

A second general radar signature prediction code has been developed by Surface Optics Corporation called RadBase [4] . RadBase is capable of generating accurate Radar Cross section and Amplitude and Phase data of complex objects using a PC. RadBase predicts radar signature using hybrid of geometrical/physical optics approach and includes advance interactions such as blocking, multibounce interactions, edge diffraction, and accounts for dielectric materials. The program has been fully validated XPATCH, but is very expensive.

After considering various options, we have set up a SAR ATR facility equipped with XPATCH and complex target CAD models at Russ Engineering Center, Wright State University. We are now capable of generating synthetic radar signals with various sensor parameters and OC's. The data set was produced using XPATCH and CAD models of vehicles obtained from the U.S. government. The radar signature prediction tool XPATCH was capable of producing images of the targets imaged using different radar frequency, polarization, and depression angle.

3.2   Baseline SAR ATR Algorithms and Implementation

The next decision to make is the selection of the particular SAR ATR algorithm to use in the experiment. The most logical choice of the SAR ATR algorithm to use would be what is commonly referred to as the baseline SAR ATR in literatures. However to date, there is no general agreement on what constitutes the baseline SAR ATR algorithms. In order to help generalize the results we will obtain on the performance of SAR ATR with variation of sensor OC's, we chose to implement several of the more popular SAR ATR algorithms, which represent the various approaches to tackle the ATR problems in our experiment. In the following sections, we will introduce some of the SAR ATR algorithms that we considered, selected and implemented.

3.2.1   MSATR ATR

The MSTAR program, under DARPA and the Wright Laboratory, has developed a model based vision (MBV) approach to SAR ATR [56] . The MBV ATR algorithm generates hypotheses of the possible identity of the unknown SAR image and then matches the features extracted from the unknown SAR image with features predicted from stored models. The scores from each hypothesis is accumulated, and the hypothesis with the greatest evidence is declared as the target [24] .

The MBV ATR algorithm posses several key advantages over other types of ATR algorithms. The MBV AR approach uses an on-line signature prediction module, which allows different sensor characteristics to be directly accounted into the generated signatures, and the number of possible signatures generated is only limited by the properties of the representation stored in the library. The MBV ATR algorithm uses a novel coarse to fine hypotheses strategy to identify targets, which allows a large number of real targets to be identified in a manner computationally traceable. The incremental approach allows the correct identification of targets with incomplete and imperfect knowledge of operating conditions.

3.2.1.1   Algorithm Description The MSTAR algorithm can be divided into two main stages. The first stage performs image and hypothesis reduction, and the second stage performs the hypotheses and testing of the SAR image chips.

The first stage can be subdivided into the Focus of Attention (FOA) and the indexing subunits. The FOA unit receives as input all of the SAR imagery collected from the sensor. The FOA unit scans the raw SAR imagery for areas with potential targets, and removes chips called Regions of Interest (ROI) that contain those potential targets. The actual method used to perform FOA processing remains to the best of our knowledge undocumented.

The ROI identified by the FOA module is passed to the indexing module. The indexing module attempts to generate possible target hypotheses which reduce the number of possible target types the MBV ATR algorithm must process to generate an identification. The hypothesis of the potential target must include an estimate of target type, pose, articulation, and even obscuring factors [24] . To perform indexing, the ROI is compared to a set of stored models in a template method based approach. The stored models in order to be useful in reducing the number of hypotheses must span the target space. The target space can be thought as of having two dimensions. The first dimension is target type, and the second dimension consists of all characteristics of the target except type including pose, articulation and variants. The models used for indexing span the target space by each being formed as a combination of target models [39] .

The second stage uses four sub modules to process the hypotheses generated by the index module for the correct identification of the ROI chip. The identification is done an iterative process using each hypothesis and ROI chip as input into the Predict, Extract, Match, and Search (PEMS) loop [24] . The PEMS loop is the foundation of the coarse to fine reasoning strategy.

The prediction function of the PEMS loop is performed by the MSTAR feature prediction

module. (MPM). The MPM can generate SAR image features and actual SAR images in an extremely flexible process that can take into account a great number of sensor and target parameters. The MPM can roughly be divided into on-line and off-line components.

The off-line component of the MPM has the job of representing the CAD model of each target in the form which allows easy, accurate, quick, and dynamic feature generation of the target with as little stored information as possible. The feature generation from the target must coincide with some type of uncertainty representation for each feature for analysis. The off-line representation of the target begins by breaking the target into the individual structures that cause specific features of the SAR image into dynamic and static phenomenology components. Dynamic phenomenology components are created or destroyed by configuration or articulation variation of the target. Static phenomenology are signature elements that do not change. Once each component of the SAR signature is identified, the phenomenology, which best characterizes each component of the SAR image is chosen for each structure. The phenomenology types include a) reflector primitives which are elementary primitives with closed form electromagnetic solutions; b) scattering centers which represent the object using the geometric theory of diffraction estimation implying the wavelength of the electromagnetic radiation of the radar wave is much smaller than the dimensions of the object; c) finally special phenomenology primitives which encompasses all other structures not represented by the first two or more specifically cavities. After the representation of each structure has been determined, the systematic data structure (SDS) of the target is determined. The SDS defines the spatial relationship between the primitives determined. The SDS consists of four different node types. The first node type is a two-way link between primitives such as between a windshield and the hood of a car. The second node type is a joint between two continuously articulating primitives such as between the turret and the body of a tank. The third node type is to link primitives that can move in a directed manner such as a car door being open or closed. The last type of node links the primitives for an alterative target configuration such as a T-72 tank with or without rear gas drums [24] .

The on-line component of the MPM has the job of generating the features of the target specified by the search module. The on-line MPM component uses the hypothesis, which includes target type, pose, configuration, and articulation to retrieve the correct primitives from the stored data in the off-line component of the MPM. The hypothesis of the configuration of the target is used by the SDS to assemble a 3-D representation of the hypnotized target. Then using sensor information, the hypothesis, and the Z-buffering algorithm, which determines how the phenomenology of the target is obstructed, features are predicted to coincide with the hypothesis from the search module [24] .

The search module guides and generates the hypotheses used in the identification of the ROI chip. The search module must be able to combine data acquired thought matches against different possible hypotheses into one complete statistical distribution. The search module uses the Bayesian score represented by a statistical likelihood generated from the match module to developed better possible hypotheses for the ROI chip, and at the end of the active search compute the posterior probability of each hypothesis given the accrual evidence for target identification [56] .

The search module must maximize both the likelihood and posterior probabilities. The

likelihood function determines the probability of extracting the observed features given the hypothesis, and can be formulated as:

$$P(Y = y|H = h) \tag{3.316}$$

where the capital letters denote random variables and lower case letters denote realization. The random variable H: Scene Hypothesis-target type, pose, articulation, background and Y: Vector of extracted features. The match module produces a single sample of this likelihood function. The target type is chosen by calculating the conditional probability of the possible target type given the extracted features. The posterior probabilities are calculated by weighting the likelihood function with prior probabilities and integrating over all hypothesis variables other than target type and can be represented as follows:

$$t = \arg \max_t P(T = t|H = h) \tag{3.317}$$

where T is target type [56] . The optimal solution would involve the complete calculation of the likelihood function, which for SAR applications is almost impossible.

The calculation of the likelihood function involves feature prediction, extraction of features from the SAR images and scoring which means simple brute force optimization taking a large number of samples of the likelihood function impracticable. The approach to optimization of the two probabilities is based on viewing the problem as a sequential sampling problem. In a classic sequential sampling problem, measurements are taken represented by

$$z_k = P(Y|h_k) \tag{3.318}$$

with an associated cost c_k for each measurement. The decision to take another sample and what sample to take (h_k) is based on the previous samples $z_1, \cdots, z_{k-1}$, and the total cost of measurement $\sum_{i=1}^{k-1} c_i$, as well as the total cost of making the final decision. The difficulty of this approach is the calculation of the cost function. The cost function assumes the knowledge of the probability distribution of the likelihood function $P(Y = y|H = h)$ and more specifically the knowledge of at all $P(Y = y|H = h)$ at all $h \neq h_k$. The formation of the optimization problem in the form of a quasi sequential sampling problem can be done by assuming the likelihood function is well behaved and decomposition of the search algorithm into two components. The first component will serve as an evidence accrual function that will calculate the conditional probability given the first k measurements or in other words

$$\pi_k(h) = P_r(H = h|z_1, \cdots, z_k). \tag{3.319}$$

The second function is a refinement function, which will use $\pi_k(h)$ as a guide to decide what the next hypothesis should be and whether to keep generating hypotheses.

The hypothesis generated by the search module can be divided into two categories. The first category of hypothesis is refinement hypothesis. Refinement hypothesis use the match score to improve the estimate of target type, or in other words, it uses the rough estimate of the target generated by the index module and gently refine the original guess more accurately.

The second category of hypothesis is generation hypothesis, which generate a new guess of what the target may be. Both types of hypothesis must be used in order to assure maximum performance.

Refinement hypothesis assume the score produced by the match module will increase as the hypothesis become closer to the ground truth. This assumption implies the likelihood function is well behaved with well-defined local maxima and the original hypotheses is close the correct maxima. The assumptions imposed on the likelihood function means that physically the system is using features that provide a clear distinguishing between target types, the index module consistently generates hypothesis near a local maximum, and the index routinely generates hypothesis that are close to the correct pose.

The search module then must use the hypotheses and the scores generated from the match module to determine the identity of the test image. The identification of the targets is accomplished by calculating the posterior probabilities based on the evidence acquired through the search. The posterior probabilities calculated are then passed through decision rules to generate a final decision. The decision rules are in the form of declaring type of the target as the type with the largest posterior probability that exceeds some threshold.

3.2.1.2   Implementation The MSTAR ATR algorithm was not implemented and hence not used in the experiment. Although the MSTAR ATR algorithm is as close to a baseline ATR algorithm that currently exits, the independent implementation of the algorithm would be virtually impossible. The public articles describing the implementation of the algorithm are too vague for any serious realization, and even without this barrier, the algorithm itself is too complicated for individual implementation. The only choice left if the algorithm was to be used, was to obtain a copy of the original code. The obtainment of a copy of the true algorithm from the government proved to be unworkable.

3.2.2   Template Based ATR Algorithm – Baseline Algorithm 1

The template method for SAR ATR is the most straight forward and perhaps the most reliable of all ATR algorithms [58] [37] . The process is little more than comparing known radar signatures collected at test ranges or from simulation with unknown radar signatures obtained from the field. The MSE is calculated between the received signal and all of the templates and the closest match chosen. Therefore, it is also known as the mean–square error (MSE) classifier.

3.2.2.1   Algorithm Description The template match algorithm has two parts: training part is to generate a template for each class of target at a particular pose angle $T_{(c_i, \theta_j)}$ and classification part is to calculate the distance (MSE) between an observation target chip to all the templates and classify the target chip to a specific target class and pose angle (c_i, θ_j). The training of the algorithm consists of simply generating templates of every target for an interval of azimuth angle. The template formation process consists of registering and estimating the mean target signature over a small azimuth angle. The assumption is made that over a small azimuth angle, the radar signature of the target remains constant. The templates ($N \times N$ dimension) are formed by averaging all of the training images in a given

small range of azimuth angles (commonly $5° \sim 10°$). Assuming there are N_{ij} training image chips within a prescribed window of azimuth angles for a target class c_i at pose angle θ_j, we can find the mean target signature using the running mean estimation as

$$M_k(x, y) = \frac{(k-1)M_{k-1}(x, y) + S_k(x - x_{\text{opt}}, y - y_{\text{opt}})}{k} \qquad (3.320)$$

for $k = 1, 2, \cdots, N_{ij}$ where the optimal spatial translation $(x_{\text{opt}}, y_{\text{opt}})$ between the next image chip $S_{k+1}(x, y)$ and the current running mean estimation $M_k(x, y)$ can be found according to the following alignment process

$$(x_{\text{opt}}, y_{\text{opt}}) = \arg\min_{x_s, y_s} \left\{ \sum_{x=1}^{N} \sum_{y=1}^{N} |M_k(x, y) - S_{k+1}(x - x_s, y - y_s)|^2 \right\}. \qquad (3.321)$$

The training process is iteratively progressed in between equations (3.321) and (3.320) with an initial value $M_1(x, y) = S_1(x, y)$ which is the first image in the training image set. The final trained template of class c_i at pose angle θ_j can be reached as

$$T_{(c_i, \theta_j)}(x, y) = M_k(x, y) \quad \text{when } k = N_{ij}. \qquad (3.322)$$

Classification is done by calculating the MSE between the unknown signal and all of the templates $T_{(c_i, \theta_j)}$ in the database. The MSE classification is performed for all (c_i, θ_j) according to

$$(c_i, \theta_j) = \arg\min_{i,j} \left\{ \sum_{x=1}^{N} \sum_{y=1}^{N} |T_{(c_i, \theta_j)}(x, y) - S(x - x_{\text{opt}}, y - y_{\text{opt}})|^2 \right\} \qquad (3.323)$$

where $(x_{\text{opt}}, y_{\text{opt}})$ are the optimal spatial translation indices for data alignment. The minimization processes are realized by comparing the maximum cross correlation between templates $T_{(c_i, \theta_j)}$ and image chip $S(x - x_{\text{opt}}, y - y_{\text{opt}})$ for all i and j. The data alignment is realized by searching for the local maximum cross correlation function within a small spatial window of translation indices $(x_{\text{opt}}, y_{\text{opt}})$. In the template matching algorithm, the amplitude of SAR image chip is often quarter powered to make the target and the shadow areas more visible while at the same time preventing the strongest scatter to dominate [21] .

3.2.2.2   Implementation The initial MATLAB code of the template matching algorithm was obtained from Mike Bryant [5] that approximated the template ATR algorithm given in the article [58] and [37] . The code was first verified and then changed to maximize the performance of the code.

For the following discussion please referee to figure (1) which provides a flow chart of MATLAB functions used in this algorithm. The MATLAB code for the template ATR algorithm obtained from Mike Bryant consists of 17 separate functions that could be subdivided into groups with four different purposes. The main groups of the program are 1). data base generation, 2). template formation, 3). calculation of the mean squared error, and 4). performance evaluation.

1.Template Matching ATR algorithm — Subroutine Flow Chart

The algorithm starts with the main program or the $MSE\_MAIN.m$ function. The main program begins with the user specified signal array size, template size, azimuth and depression uncertainty by way of variables. The template matching ATR implementation assumes that the target pose angle can be estimated within a small window of uncertainty by another means. It reduces number of templates to be tested because only the templates within an azimuth window specified by the azimuth uncertainty value around the real azimuth value is tested in the algorithm. Then structures are declared that allow the specification of the training and testing data sets. The user is able to specify by way of serial number and depression angle used for training and testing targets. Then the **create_database** function is called.

The **create_database** function is the key function in the group 1) of the algorithm that generates the database. The function begins with calling the function **find_filenames**. The **find_filenames** function goes through the entire directory specified by the user to develop a path directory to each of the files in the specified directory. A structure containing the file names is passed back to **create_database** function. All of the files with names specified by the new structure are then read into the new database. Then using the function **find_header_value** for each file, the Phoenix header is searched for important characteristics (such as target azimuth, size of target, etc.) and the values of each characteristics is copied to fields of structure with the same name making up the database. This process allows the new database to be more easily index. The last step in the creation of the database is a call to the function **create_index**. This function goes through each field of the structure, calls the **unique_token** function which finds all of the unique values of that field, and then creates an index of each unique field. Therefore the program is able to access all targets with a depression angle of $17°$ with a single presorted index. With the creation of the database the next step is the formation of the templates.

The **make_all_tmplts** function is the key function in the group 2) of the algorithm that forms the templates. The function goes through each azimuth and depression window of each target and generates a template. The function begins by determining the values of the azimuth and depression window for the present template. Then using the function **database_query** finds the indices of all the training images in the database which satisfy the given window intervals. The **make_all_tmplts** function then calls **get_sig** function, which calls the **read_sig** function, which reads the magnitude image into the program. The **get_sig** function quarter powers the image and then sends all of the images back to the **make_all_tmplts** function in the form of a structure. Then the **make_tmplt** function is called. This function removes each image off of the structure containing all of the images in the training window aligns the image with the present template with the function **sig_align** and then averages all of them together. The function **sig_align** aligns the template and the image by calculating the covariance between the two, and then shifting. The covariance is calculated using inverse Fourier transform on the template, and Fourier transform on the image and then multiplying the two together.

The **test_mse** function is the key function in the group 3) of the algorithm that calculates the mean squared error between the test image and the templates. The function begins by using **database_query** to find the indices of the test images, along with the functions **get_sig**

and **read_sig** to retrieve the test images from the database. The tested templates are aligned with the signal using **sig_align** and then the difference between the image and template is calculated and squared.

The performance of the algorithm is then calculated. The performance measures chosen were the confusion matrix calculated by the **score** function, and the receiver operating curves (ROC).

3.2.2.3   Verification The code was intended to be verified by performing two of the baseline classifications performed in article [58] . The templates in the article were constructed using three target types imaged at a depression angle of 17° and using azimuth interval of 17°. The targets used in the training set are given in (3.324). The first test was performed simply by resubstituting the same targets used in the training set but imaged at depression angle of 15°. The second test involves different variants of the training vehicles but also imaged at depression angle of 17°.

Training/Test set 1

Model	Vehicle	Serial No.	Depression angle
BMP–2	#1	9463	17°/15°
M–2	#1		17°/15°
T–72	#1	132	17°/15°

$$(3.324)$$

Test set 2

Model	Vehicle	Serial No.	Depression angle
BMP–2	#2	9566	17°
M–2	#3		17°
T–72	#4	812	17°

$$(3.325)$$

However, as of yet the data was not available to conduct the verification.

3.2.2.4   Optimization By varying the parameters of the template ATR algorithm and charting the performance of the code using new sets of training and test data, we performed the optimization of the algorithm. The same training and test data sets were used later on to optimize all three of the SAR ATR algorithms implemented.

The new data set evaluated the performance of the algorithms over several extended operating conditions. The training set consisted of two vehicle types (c21 and 132) both imaged at a depression angle of 17° (3.326). The test set consisted of not only the same two vehicles imaged at a different depression angle of 15°, but also involved two different versions of each of the training vehicles imaged at a depression angle of 15°. The test data set also contained a vehicle (c71) that was of a different class than the vehicles trained as a confuser object (3.327).

Train set for algorithm optimization

Model	Vehicle	Serial No.	Depression angle	No. of Images
BMP–2	#1	c21	17°	233
T–72	#1	132	17°	232

(3.326)

Test set for algorithm optimization

Model	Vehicle	Serial No.	Depression angle	No. of Images
BMP–2	#1	c21	15°	196
	#2	9563	15°	195
	#3	9566	15°	196
T–72	#1	132	15°	196
	#2	812	15°	195
	#3	s7	15°	191
BTR–70	#1	c71	15°	196

(3.327)

The first decision to be made regarding the performance of the algorithm was whether to shift or not shift the test image over the template. In the first run, the algorithm was tested without any kind of shifting to help correct for any centroid errors between the images.

Results without alignment

Template (80–by–80)	BMP–2	T–72	Unknown
BMP–2#1(196)	194	0	2
BMP–2#2(195)	179	3	13
BMP–2#3(196)	178	3	15
T–72#1(196)	1	193	2
T–72#2(195)	30	113	52
T–72#3(191)	41	118	32
BTR–70(196)	136	22	38

(3.328)

Then a second run was performed using the **sig_align** function, which allowed the test image to be shifted over the template.

Results with alignment

Template (80–by–80)	BMP–2	T–72	Unknown
BMP–2#1(196)	188	1	17
BMP–2#2(195)	170	10	15
BMP–2#3(196)	176	10	10
T–72#1(196)	0	194	2
T–72#2(195)	8	138	49
T–72#3(191)	9	149	33
BTR–70(196)	108	9	79

(3.329)

Comparing the results obtained shows that shifting (3.329) gave slightly diminished results when it came to identifying the BMP-2 vehicles but greatly increased the number of T-72 vehicles correctly identified. The large increase in performance of T-72 identification more than set off the slight decrease in performance of BMP-2 identification. The alignment of test images was adopted for all other tests.

The second measure taken to improve the performance of the template ATR algorithm was the removal of the mean of all images before template formation or testing. The algorithm was trained and tested with zero mean images and the results were recorded.

Results with alignment and mean removed

Template (80–by–80)	BMP–2	T–72	Unknown
BMP–2#1(196)	193	0	3
BMP–2#2(195)	178	0	17
BMP–2#3(196)	185	0	11
T–72#1(196)	0	193	3
T–72#2(195)	0	130	65
T–72#3(191)	0	174	17
BTR–70(196)	122	2	72

$$(3.330)$$

The zero mean images gave a very large increase in the performance of the algorithm. The algorithm failed to mis–identify any of the BMP-2 or T-72 vehicles. The zeroing the mean of all images was adopted for all other tests.

The last property that was varied in the algorithm was the size of the template. The size of the template determined how much of the original image would be used in identification. The first test run was done using a template size of 90X90.

Results with alignment and mean removed

Template (90–by–90)	BMP–2	T–72	Unknown
BMP–2#1(196)	192	0	4
BMP–2#2(195)	175	0	20
BMP–2#3(196)	184	0	12
T–72#1(196)	0	194	2
T–72#2(195)	1	132	63
T–72#3(191)	0	176	15
BTR–70(196)	121	1	74

$$(3.331)$$

The bigger template allowed slightly more of the T-72's to be properly identified, but slightly less of the BMP-2's were properly identified. The increase in size was inconsequential. The template size of 100X100 gave even worse results. A last run of was performed with a template size of 64X64.

Results with alignment and mean removed

78

Template (64–by–64)	BMP–2	T–72	Unknown
BMP–2#1(196)	188	1	7
BMP–2#2(195)	170	10	15
BMP–2#3(196)	176	10	10
T–72#1(196)	0	194	2
T–72#2(195)	8	138	49
T–72#3(191)	9	149	33
BTR–70(196)	108	9	79

(3.332)

The results were clearly worse than the bigger template, and the template size of 80X80 was chosen as the best for the data set.

Though out the performance evaluation, the confuser was mis–identified at an alarming rate. The confuser vehicle in hindsight should be extremely hard to separate because of its similarity to the training vehicles. Therefore making it a very useful confuser.

3.2.3   Lincoln Laboratory ATR System – Baseline Algorithm 2

The Lincoln Laboratory ATR system [30] consists of three separate stages with each designed to perform a specific task. The three stages are 1). detector, 2). discriminator, and 3). classifier.

3.2.3.1   Algorithm description The detector receives the raw SAR data and extracts potential regions of interest (ROI). The detector identifies candidate pixels of ROI based on its local brightness. This is done using a two-parameter CFAR detector defined as

$$\frac{X_t - \mu_c}{\sigma_c} > K_{\text{CFAR}}$$ (3.333)

where X_t is the amplitude of the pixel being tested, μ_c and σ_c are respectively the mean and standard deviation of the clutter inside of the boundary stencil, and K_{CFAR} is the threshold to control the false alarm rate. The boundary stencil is simply a user defined area chosen around each test pixel.

The discriminator stage process each ROI produced from the detector and rejects any ROI that does not contain man made objects. The discriminator stage can itself be broken into three parts. The first component uses a rectangular target size template to slide over the ROI in order to determine the location and orientation of the object by maximizing the energy inside the template. The second part of the discriminator computes the discrimination features of the ROI and the last component of the discriminator combines these features into a discrimination statistic that indicates how "target-like" the ROI is. The discriminator stage uses 12 discrimination features that can be divide into four groups. The four groups are textural features, size features, contrast features and finally polarimetric features. The textural features include a). the standard deviation which measures the fluctuation in

intensity of the image, b). a fractal dimension which is defined by

$$\text{dim} = \frac{\log M_1 - \log M_2}{\log 2}$$

where M_1 is equal to the number of 1 by 1 pixel boxes need to cover the target and M_2 is equal to the number of 2 by 2 pixel boxes needed to cover the target, and c). the weighted fill feature which measures the total energy contained in the brightest 5% of pixels in the ROI. The size features include a) the mass which is simply the number of pixels in the target, b). the diameter which is defined as the length of the diagonal of the smallest rectangle that encloses the target, and c). the normalized rotational inertia which is defined as "the second mechanical moment of the blob around its center of mass, normalized by the inertia of an equal mass square." The contrast features consist of a). the peak CFAR, which is simply the maximum value of the target in the CFAR image, b). the mean CFAR, which is the mean of the values of the target in the CFAR image, and c). the percent bright CFAR, which is the percentage of pixels in the target of the CFAR image greater than chosen empirically threshold. The polarimetric include a) the percent pure (odd or even) which is the percentage of pixels in the target which fall in either the even bounce or odd bounce channel, percent pure even which is percentage of pixels in the target which fall in the even bounce channel, and b) the percent bright even which is the percentage of pixels in the target which exceed the threshold in the CFAR image, and even bounce. The even and odd bounce images are calculated using the formulas

$$E_{odd} = \frac{|HH + VV|^2}{2} \quad \text{and} \quad E_{even} = \frac{|HH - VV|^2}{2} + 2|HV|^3. \tag{3.334}$$

The best discrimination features for a given system (Resolution, Polarization, etc.) are combined into a single discrimination statistic defined by the distance metric

$$d(X) = \frac{1}{n}(X - M)^T \Sigma^{-1}(X - M) \tag{3.335}$$

where n is the number of features used, M and Σ are estimates of the mean vector and covariance matrix of the features used obtained from the training data, and X is features measured from the test object.

The classifier stage consists of a mean-squared error template matching classifier design to reject man-made confuser false alarms and identify the remaining targets. The reference templates for the MSE classifier are constructed by first normalizing the training images. Normalization begins by converting the magnitude image pixel to a dB value. Then thresholds are determined to eliminate all but the brightest and dimmest 1.5% of the pixels. The resulting image consists only the bright target pixels and the dim shadow pixels. A binary mask is then generated for the image and is morphologically processed to group all of the target and shadow pixels together. The pixels in the original dB image not part of the binary mask are used to determine the mean dB clutter level μ_c. The training image is then

80

normalized by removing the average clutter level

$$R_i = U_i - \mu_c. \tag{3.336}$$

The normalized image has the average clutter level removed, but the energy of the target in relation to the clutter in the background is maintained. The images are then chopped with a window slightly larger than the target to remove the influence of clutter in the templates.

The pattern matching process begins with the normalization of the ROI chip by the same procedure outlined above. Then the MSE is calculated by

$$\varepsilon = \frac{\sum_{i=1}^{N} (R_i - T_i)^2}{N} \tag{3.337}$$

where N is the number of pixels in the reference template and R_i and T_i are the pixel values in the reference template and test image respectively. The reference template is also slid a small amount over the test image in the calculation of a minimum MSE to make up for any small centroid errors. The normalization scheme causes the error measured to equal the difference of total energy between the reference template and the test image.

3.2.3.2   Implementation MATLAB code was developed to approximate the classifier stage for the Lincoln Laboratory baseline ATR. The first two stages were not implemented due to the fact that they were unnecessary for the experiment. The detector stage is used to identify ROI and the discriminator stage is used to remove clutter false alarms. Since all tests were done using MSTAR target chips or Xpatch simulations of targets, all data were already formed into data chips and contained no clutter. The code was verified and then the parameters of the code changed to maximize performance.

The MATLAB code developed for this algorithm utilized many of the same functions that were used in the template ATR MATLAB code. All of the data handling functions were reused in this ATR implementation. The database generation, and performance evaluation were identical and the template formation and mean squared error subparts were identical except for a few small differences.

The largest difference between the two algorithms was the image normalization used in the template formation and mean squared error subunits. The normalization began with removing all but the brightest and dimmest 4% of the image pixels. The 4% value was used instead of 1.5% because the paper used images that were much larger. The selection of pixel values was performed by first using the **sort** command in MATLAB to organize the pixels from largest to smallest value. Then it was simple matter to remove the brightest and dimmest pixels using the **find** command. A binary mask was then created using these pixels. The binary masks for each image were plotted and it was determined that morphologically processing the mask gave very little increase in performance because the target and shadow pixels were extremely well grouped. The mean of the pixels not under the mask were calculated and subtracted from the original image.

The only other difference in the code was difference in the **get_sig** function. The image obtained was converted into a dB image in this function instead of quarter powering the image.

3.2.3.3   Verification The verification of the Lincoln Laboratory ATR system was intended to be done by re-performing the first experiment in the paper [30] . The classifier in the paper was constructed with 72 templates for each target spanning an azimuth angle of 5 degrees for each target in the training set. The training target set include 9 target types

Model	BMP–2	M2	T–72	BRT–60	BTR–70	M1	M109
Serial No.	9563		132		c71		

Model	M110	M113
Serial No.		

(3.338)

The algorithm was then tested using the 18 vehicles in the test set.

Model	BMP–2	BMP–2	BMP–2	BRT–60	BTR–70	M109
Vehicle	#1	#2	#3			
Serial No.	9563	9566	c21		c71	

Model	M110	M113	M1	M2	M2	M2
Vehicle			#1	#2	#3	
Serial No.						

(3.339)

Model	M548	T–72	T–72	T–72	HMMW	M35
Vehicle		#1	#2	#3		
Serial No.		132	812	s7		

Unfortunately, many of the data sets are restricted. As of now, the data was not available to conduct the verification.

3.2.3.4   Optimization To optimize the algorithm, a number of properties were varied in the algorithm to obtain the maximum performance of the algorithm using a test set that contained targets imaged at a different depression angle than the training set, along with confusers and different versions of vehicles. The same sets of training (3.326) and testing (3.327) data are used.

   The first parameter to be varied was the size of the template. The first step was to generate a baseline result using a template size of 80–by–80, which all other results could be compared.

Lincoln Laboratory ATR: 8% Pixels used

Template (80–by–80)	BMP–2	T–72	Unknown
BMP–2#1(196)	164	16	16
BMP–2#2(195)	144	30	21
BMP–2#3(196)	156	25	15
T–72#1(196)	18	166	12
T–72#2(195)	37	133	25
T–72#3(191)	25	139	27
BTR–70(196)	105	40	51

(3.340)

Then a run was performed using a template size of 48–by–48 and the results recorded.

Lincoln Laboratory ATR: 8% Pixels used

Template (48–by–48)	BMP–2	T–72	Unknown
BMP–2#1(196)	163	16	17
BMP–2#2(195)	155	19	21
BMP–2#3(196)	162	11	23
T–72#1(196)	16	171	12
T–72#2(195)	21	150	24
T–72#3(191)	21	148	22
BTR–70(196)	113	34	49

(3.341)

The decrease in template size allowed better identification for each target in the test set. The size of the template was then decreased to 32X32 and the best result was recorded.

Lincoln Laboratory ATR: 8% Pixels used

Template (32–by–32)	BMP–2	T–72	Unknown
BMP–2#1(196)	175	6	15
BMP–2#2(195)	165	7	23
BMP–2#3(196)	161	7	28
T–72#1(196)	7	182	7
T–72#2(195)	16	157	22
T–72#3(191)	13	157	21
BTR–70(196)	106	34	56

(3.342)

All following tests were conducted using a template size of 32X32.

The second parameter to be varied was the percentage of pixels used to generate the binary mask. The first experiment conducted was to increase the number of pixels used to 16%.

Lincoln Laboratory ATR: 16% Pixels used

Template (32–by–32)	BMP–2	T–72	Unknown
BMP–2#1(196)	176	5	15
BMP–2#2(195)	164	7	21
BMP–2#3(196)	161	8	27
T–72#1(196)	7	182	7
T–72#2(195)	16	157	22
T–72#3(191)	12	158	21
BTR–70(196)	108	32	56

(3.343)

The result was a very slight degradation of performance. Then a run was performed using only 1.5% of the pixels.

Lincoln Laboratory ATR: 1.5% Pixels used

83

Template (32–by–32)	BMP–2	T–72	Unknown
BMP–2#1(196)	163	17	16
BMP–2#2(195)	144	30	21
BMP–2#3(196)	156	25	15
T–72#1(196)	18	167	11
T–72#2(195)	37	133	25
T–72#3(191)	23	140	28
BTR–70(196)	105	40	51

$$(3.344)$$

This showed a large degradation in performance. The original value of 8% seemed to have the best performance and used for all other tests.

3.2.4   Conditionally Gaussian ATR Algorithm – Baseline Algorithm 3

The conditionally Gaussian approach to SAR ATR uses a stochastic signal to model the received radar signal [33] . The stochastic model attempts to model the target accurately while capturing the variability of SAR target imagery due to obstruction, orientation, or variation of vehicle type. Therefore in theory the conditionally Gaussian ATR approach should be able to accurately classify targets which show significant differences in range profile than those used in training the set.

3.2.4.1   Algorithm Description The radar return is modeled as a complex Gaussian random process, which can represented by:

$$r = s(\theta, a) + w. \qquad (3.345)$$

The signal part of the radar return $s(\theta, a)$ which represents the characteristics of the imaged scene is modeled as a complex Gaussian random vector that is dependent of target type a and target orientation θ. The conditional mean and covariance are denoted by $\mu(\theta, a)$ and $K(\theta, a)$ respectively. The last part of the radar return w represents the noise component of the received signal and is modeled as complex Gaussian noise having zero mean and a covariance matrix equal to $N_0 I$. The overall mean and covariance of the radar return can be easily calculated to give:

$$\begin{aligned} E\left\{r|\theta, a\right\} &= \mu(\theta, a) \qquad (3.346)\\ E\left\{(r - \mu)(r - \mu)^*|\theta, a\right\} &= K(\theta, a) + N_0 I. \end{aligned}$$

The stochastic model derived above can be simplified even further. First the noise component w is assumed to be independent of signal s and spatially invariant. Furthermore, the signal s is assumed spatially invariant and is the function of only for the given target type a and orientation angle θ as well as the variance of each pixel. From the work done by O'Sullivan using HHR and SAR data [33] , each pixel of the signal s of the target is well modeled as having zero mean $\mu(\theta, a) = 0$. These assumptions can be used to yield a diagonal covariance

matrix K which then leads to the log–likelihood function of

$$l(r|\theta, a) = \sum_i \left[-\ln\left(K_{i,i}(\theta, a) + N_0 I\right) - \frac{|r_i|^2}{K_{i,i}(\theta, a) + N_0 I} \right] \tag{3.347}$$

which is summed over all of the pixels.

The above derivation shows that the only unknown values and hence the values which need to be estimated from the training data are the variances of each pixel. First the assumption is made that the variance of each pixel is nearly constant within small intervals of orientation angle θ. Therefore the training database can be divided into N_w windows with each spanning an interval of azimuth angle d radians wide. The kth window is centered at $\theta_k = \frac{2\pi}{N_w} k$. The kth window interval of azimuth values that each pixel is trained is given by

$$W_k = \left[\frac{2\pi}{N_w} k - \frac{d}{2}, \frac{2\pi}{N_w} k + \frac{d}{2} \right]. \tag{3.348}$$

Now the variance of the ith pixel for target class a_l at pose angle θ_k can be found using

$$\sigma_i^2(\theta_k, a_l) = \frac{1}{N_k} \sum_{\theta \in W_k} |r_i(\theta, a_l)|^2 \quad \text{for } 1 \leq k \leq N_w, \tag{3.349}$$

where N_k is the number of training images within the window of interval W_k and $1 \leq l \leq t$ with t equal to the number of targets in the training data base. Because the estimated variance is unbiased due to the fact the mean is assumed to be zero. In other words, if every pixel is assumed to have zero mean, the variance of a pixel at a specified location is simply the mean of the squared magnitudes of all the pixels in that location of all the training images within the azimuth window interval W_k.

The classification of the ROI is performed using a Bayesian approach by selecting the target class $a(r)$, which maximizes

$$P(a|r) \propto P(r|a)P(a). \tag{3.350}$$

In our problem set up, we need to maximize

$$P(a|r) \propto P(r|\theta, \eta, a)P(\theta|a)P(\eta|a)P(a) \tag{3.351}$$

where θ is the orientation of the target and η is the location of the target. If we treat the orientation of the target θ and the location of the target η as nuisance variables, we can integrate over all possible orientations and locations to obtain the correct result. With the approximation of covariance function $\sigma_i^2(\theta_k, a_l)$ is a piecewise constant in $\theta \in W_k$, the probability density function $P(r|\theta_k, \eta_j, a)$ is approximated as piecewise constant in orientation θ_k and location η_j. The Bayesian estimate of target type over all possible orientation and location becomes

$$\hat{a}(r) = \arg\max_a \sum_k \sum_j P(r|\theta_k, \eta_j, a). \tag{3.352}$$

3.2.4.2   Implementation MATLAB code was generated to approximate the conditionally Gaussian ATR model presented in the article [33] . The code was verified, and then parameters of the code were changed to maximize the performance of the code.

The MATLAB code developed for this algorithm utilized many of the same functions that were used in the template ATR code. All of the data handling functions were reused in this ATR implementation. The database generation was identical.

The training algorithm was performed using the function **train_gauss**. The first step of the training was to convert the matrix form of image into a column vector. Using all of the column vectors that represent the training images in the given azimuth window W_k, the variance of each pixel is calculated by the simplification that the variance is equal to the mean of the squared pixels in the training group. The variance at each pixel location is then stored in a variance vector identified by $V(\theta_k, a_l)$ from which will be used as the dictionary for identification.

The testing part of the algorithm is performed by the **test_gauss** function. The **test_gauss** function first converts the test image into a single column vector. The test and training vectors were assumed to be well registered with each other and no shifting was performed. This assumption was well founded since only MSTAR and XPACTH data was used. Then using the **normpdf** MATLAB function calculates the probability values of each test pixel value using the zero mean Gaussian distribution function with the variances from the variance vector $V(\theta_k, a_l)$ in the training set. For each given variance vector in the training set, the probability of each pixel in the test image is calculated and all of the probability values of the test image are summed and normalized. The process yields one summed and normalized probability value for each variance vector in the training set (for all $k's$ and $l's$). The identification of the target is performed by the **score_gauss** function, which assigns the test image the identification a_l of the variance vector in the training set with the maximum summed and normalized probability value.

3.2.4.3   Verification The verification of the conditionally Gaussian ATR method was done by reperforming the author's baseline experiment under what was called standard operating conditions [33] . The baseline experiment used image size of 80–by–80 with $N_w = 72$ orientation windows trained with an overlapped azimuth spanning interval of $d = 10°$. The training data set consisted of four target types obtained from the publicly released MSTAR data set with two the target types consisting of multiple vehicle types all imaged at a depression angle of $17°$.

Training Set

Model	Vehicle	Serial No.	Depression angle	No. of Images	
BMP–2	#1	9563	17°	233	
	#2	9566	17°	231	
	#3	c21	17°	233	
T–72	#1	132	17°	232	(3.353)
	#2	812	17°	231	
	#3	s7	17°	228	
BRDM–2	#1	E–71	17°	298	
BTR–70	#1	c71	17°	233	

The testing set consisted of the same vehicles imaged at a depression angle of 15°.

Testing Set

Model	Vehicle	Serial No.	Depression angle	No. of Images	
BMP–2	#1	9563	15°	195	
	#2	9566	15°	196	
	#3	c21	15°	196	
T–72	#1	132	15°	196	(3.354)
	#2	812	15°	195	
	#3	s7	15°	191	
BRDM–2	#1	E–71	15°	263	
BTR–70	#1	c71	15°	196	

The algorithm was tested and compared to the author's result.

Author's result [33]

	BMP–2	BRDM–2	BTR–70	T–72	
BMP–2(587)	581	0	0	6	
BRDM–2(263)	6	243	0	14	(3.355)
BTR–70(196)	7	0	186	3	
T–72(582)	0	0	0	582	

Our result

	BMP–2	BRDM–2	BTR–70	T–72	
BMP–2(587)	578	0	2	7	
BRDM–2(263)	6	243	1	15	(3.356)
BTR–70(196)	8	0	185	3	
T–72(582)	2	0	0	580	

The verification shows that our algorithm is in good agreement with the one presented in the paper.

3.2.4.4   Optimization To optimize the algorithm, a number of properties were varied

in the algorithm to obtain the maximum performance of the algorithm using same test set (3.327) that contained targets imaged at different a different depression angle than the training set (3.326) along with confusers and different vehicle versions.

The first parameter to be varied is the size of the image used. The first step was to generate a baseline result which all other results could be compared. In this run, the data was assumed to have zero mean, and used an image size of 48–by–48 which was the image size the author reported having the best results [33] .

Conditionally Gaussian ATR: 48–by–48

Zero Mean	BMP–2	T–72	Unknown
BMP–2#1(196)	180	0	16
BMP–2#2(195)	169	9	17
BMP–2#3(196)	159	20	17
T–72#1(196)	1	172	23
T–72#2(195)	13	152	31
T–72#3(191)	10	169	12
BTR–70(196)	107	84	5

$$(3.357)$$

A run was first performed using a template size of 32–by–32 and the results recorded.

Conditionally Gaussian ATR: 32–by–32

Zero Mean	BMP–2	T–72	Unknown
BMP–2#1(196)	184	0	12
BMP–2#2(195)	169	13	13
BMP–2#3(196)	185	6	5
T–72#1(196)	1	170	25
T–72#2(195)	13	140	42
T–72#3(191)	18	154	19
BTR–70(196)	143	52	1

$$(3.358)$$

The results from a decrease in template size obviously gave worse results. A run of the data was then performed using an image size of 64–by–64, and the results recorded.

Conditionally Gaussian ATR: 64–by–64

Zero Mean	BMP–2	T–72	Unknown
BMP–2#1(196)	192	0	4
BMP–2#2(195)	157	12	26
BMP–2#3(196)	169	10	17
T–72#1(196)	1	192	3
T–72#2(195)	52	93	50
T–72#3(191)	50	125	16
BTR–70(196)	97	70	29

$$(3.359)$$

88

The results of the experiment clearly show that image size of 48–by–48 is optimal.

The last parameter varied in the optimization was the assumption that the SAR imagery data is well modeled having zero mean. A run of the data was conducted where the mean the pixel values were calculated.

Conditionally Gaussian ATR: 48–by–48

Calculated Mean	BMP–2	T–72	Unknown
BMP–2#1(196)	192	1	3
BMP–2#2(195)	162	10	23
BMP–2#3(196)	148	27	21
T–72#1(196)	2	192	2
T–72#2(195)	18	136	41
T–72#3(191)	19	146	26
BTR–70(196)	77	69	50

(3.360)

The zero mean assumption gave surprisingly good results and better than actually calculating the mean. This result is still puzzling.

3.3   Experimental Paradigm and Preliminary Test — A Road Map for Future Study

Even though, the literature search turned out very little work having been done in SAR parametric study for ATR, every ATR work showed good performance only under fixed set of SAR image parameters. The ATR algorithms were always trained and tested under the same or very similar sensor OC's. Their performance has the tendency being degraded severely as soon as the SAR image sources from different sensor or sensor OC's are applied. As you go through the SAR image formation algorithms and various assumptions made on the sensor parameters in the Brief section, you can realize the significant effects of SAR parameters and imaging algorithms on the appearance (pixel values) of SAR images. Independent of the underline ATR techniques such as model based, template matching, stochastic, etc., all ATR algorithms will be affected by the variations in sensor OC's as long as they are image based (using SAR images as the observation data source). Inconsistency in the data observation under various sensor OC's will unavoidably cause degradation in target classification.

In order to understand the level of significance of the effects of the sensor OC's on ATR performance, we need to set up an experimental paradigm to test various sensor OC's and their combinations. Now we have established a limited baseline ATR algorithms and surveyed the availability of existing data sources for parametric study. The next component of the experimental paradigm is to decide the choice of which sensor OC's should be investigated in the experiment. Although the lack of any real research into the effects of sensor OC would imply any group of sensor OC's would suffice, we chose to study a few of the sensor OC's that seem more likely to produce the largest effects on SAR ATR performance and likely to be properly modeled. Plus, the combinations of those sensor OC's

will create a larger dimensional problem to study.

3.3.1   SAR Sensor Parameters for Further Study

The **depression angle** that the sensor forms with the imaging plane will be evaluated in the preliminary experiment. The depression angle is the sensor OC that determines how the projection of the real 3-D object to the 2-D SAR image plane will be formed. Although the effects of depression angle is the only sensor OC to be investigated in most SAR ATR algorithms, the evaluations of depression angle is done using MSTAR data where the depression angle is only varied a few degrees. The depression angle is a relatively independent sensor OC which has very little interaction with other sensor OC's. In most of SAR image algorithms, depression angle is dealt with at the beginning of the process to form a slant plane. Therefore, it is easy to model and simulate. The depression angle has great effects on SAR image appearance and so as the performance of ATR.

The **frequencies** of the radar pulse used by the sensor to collect SAR imagery will be evaluated in the preliminary experiment. The choice of frequency and bandwidth of a radar pulse is one of the most important characteristics of the sensor. Although the use of simulated data will not allow an investigation of the effects of foliage obstruction and FOPEN radar, the effects of frequency and resolution of complex objects can be investigated. The frequency and bandwidth of radar pulse is relatively simple to model. The simulation using Xpatch can generate radar response signals with wide frequency range. However, frequency and bandwidth have complicated interactions with the assumptions made in the SAR image formation algorithms. Some cares have to be taken in SAR image formation algorithms to handle the frequency and bandwidth variations.

The **polarization** of the radar pulse used by the sensor to collect SAR imagery will also be evaluated in the preliminary experiment. The polarization of the radar wave will determine some of the scattering characteristics of the incident waves on the complex object and hence extremely important in the formation of the SAR image. The effects of polarization on SAR ATR algorithms have not been covered in depth in any previous study. Polarization is easy to model and relatively independent of other sensor OC's.

The **noise level** in the received SAR image will also be evaluated in our preliminary experiment. Noise level in our SAR imagery can be easily manufactured in our simulated data by randomly changing pixel values in our image to a random number obtained from a Rayleigh distribution which models speckle. The experiment should provide valuable information for future development of ATR algorithms.

The sensor OC's of **squint angle**, **type of antenna** (beamwidth, resolution, footprint) and **synthetic aperture length** are closely related in SAR image formation algorithms. Any change on one parameter will affect the selection of others in the image formation algorithms. Many assumptions and approximations of parameters in the image formation algorithms have to be changed to reflect the sensor OC's. The type of antenna which will affect the radar beamwidth, resolution and footprint is a very hard to model sensor OC and very expensive to come up with real data to cover the variation of radar antenna types. The variations of radar beamwidth, resolution and footprint can not be simulated in Xpatch.

Therefore, we will leave the antenna out of the parametric study. This is usually not a big issue, due to the ATR is almost never performed cross the data from different kinds or radar. Squint angle and synthetic aperture length can be modeled in the Xpatch simulation and SAR image formation algorithms. They are connected with SAR operation modes like **stripmap vs. spot** and **single vs. multi-look**. All of these sensor OC's can be modeled in simulation however they all have close association with each other in SAR image formation algorithms. They are required to be studied together with a limited sets realistic OC constrains that can be derived from real SAR sensor systems or from prior publications of those subjects.

3.3.2   Preliminary Experiments on Available Public Data

Although public SAR imagery is limited, there existed only enough data to perform one preliminary experiment on the variations of depression angle sensor OC. A subset of the MSTAR data contained targets imaged at depression angles of 15° and 45°. The targets consisted of T72_A64, BRDM-2, ZSU_23_4 and 251. Each baseline ATR algorithm was trained using the all targets imaged at 15° (no confusers) and then tested using the images formed using the depression angle of 45°. All the baseline algorithms ran on their optimized parameter settings.

Template Matching Algorithm

303 Chips	251	T72_A64	BRDM-2	ZSU_23_4	Unknown
251	53	143	52	1	54
T72_A64	0	234	69	0	0
BRDM-2	0	172	131	0	0
ZSU_23_4	155	58	10	13	67

$$(3.361)$$

Lincoln Lab. ATR Algorithm

303 Chips	251	T72_A64	BRDM-2	ZSU_23_4	Unknown
251	26	121	108	0	48
T72_A64	0	184	100	0	19
BRDM-2	0	181	98	0	24
ZSU_23_4	57	90	98	28	30

$$(3.362)$$

Conditional Gaussian Algorithm

303 Chips	251	T72_A64	BRDM-2	ZSU_23_4	Unknown
251	234	13	0	3	53
T72_A64	28	271	0	0	4
BRDM-2	21	281	0	0	1
ZSU_23_4	130	29	0	71	63

$$(3.363)$$

As expected, none of the baseline ATR algorithms perform satisfactorily on the data sets imaged at such large difference in depression angles.

3.3.3   Simulated Data Generation using Xpatch

The lack of available data across the sensor OC dimension combined with the expense of generating real data has lead us to the generation of simulated data using Xpatch. For the experiment we will need data consisting of several targets with variation in frequency, polarization, depression angle, and artificially with noise level. The target set consists of three high definition CAD models which were obtained from the USAF. The cad models consist of a BMP, T-72, and a BTR-70.

The parameters for the Xpatch simulation were set up to provide results which provide the most "raw" information possible while trying to mirror the MSTAR data collection. Each simulation was set up to collect a series of individual range profiles over the synthetic aperture in the frequency domain rather than allowing Xpatch to automatically generate the SAR image. Although this action had the effect of increasing the simulation time from 10 hours to generate one image to over 100 hours, it provides more accurate information, and allows us to use different image formation and weighting algorithms with different parameter such as synthetic aperture length. In order to decrease the amount of simulated data generated, it was decided that only a few azimuth angles were needed for each target over each sensor dimension. The data set will contain each target imagined at center azimuth angles of 0°, 30°, 60°, 90°, 120°, 150°, and 180°. This will allow images of the target from the front to back while eliminating essentially the same images because of the symmetry of the target.

The depression angle data will be collected from 20° to 45° in 5° increments. The data will be simulated trying to mirror the MSTAR collection. The simulation will be done using a center frequency of 9.6 GHz (X-band) with a bandwidth of 0.5 GHz providing 11.8 inches of resolution. The synthetic aperture has an integration angle of 2.9842° which provides a resolution of 11.8 inches in cross range which gives square resolution pixels.

The frequency data will be simulated from 1 GHz to 10 GHz in 1 GHz increments. Although originally the frequency bandwidth was intended to be much larger, the longer simulation time which would be required because of the necessity to use exact solvers at low frequencies instead of the high frequency approximations constrained the frequency range and kept it in the GHz range. The simulation will be set up to keep the keep the square 11.8 inch resolution pixels for each frequency range. This implies integration angle will increase from 2.9842° at 10 GHz to 29.842° at 1 GHz. The bandwidth of the signal will remain at 0.5 GHz for each data collection.
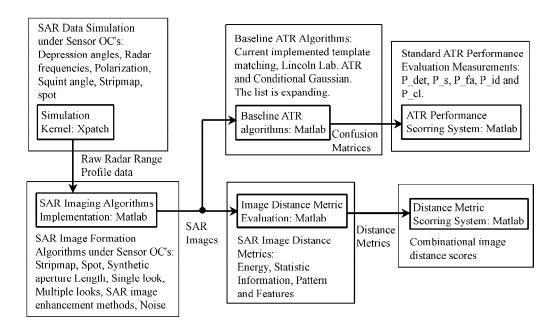
The data simulated so far consists of the T-72 and BMP at azimuth angles of 0°, 30°, 60°, 90°, 120°, 150°, and 180° at the depression angles of 30°, and 35° at 9.6 GHz. There was also a collection of the BMP at 30° depression angle at 1GHz for azimuth angles from 0° to 360°. The data simulation is continuing as planned. We expected to finish the initial data simulation in May 2003 and some experiments will be conducted after that.

3.3.4   SAR ATR Parametric Experimental Platform

This section provides an explanation of proposed SAR ATR parametric experimental

platform shown in figure (2). In this platform, we have already invested a SUN workstation equipped with Xpatch and the detailed target CAD models obtained from the Air force. This investment is located at an ITAR facility, 023 of Russ Engineering Center at Wright State University. This facility provides us the capability of generating simulated raw radar range profile data or SAR images under various sensor parameters such as depression angles, radar frequencies, polarization, squint angle, stripmap and spot mode, etc. To generate raw radar range profile data gives us some flexibility to vary some of the sensor OC's in SAR image formation algorithms or vary the image formation algorithm itself. The next piece in the platform is the image distance metric to quantify the image differences for the SAR images generated under different sensor OC's. SAR Image is an information source with multiple characteristics and those characteristics will have different impacts on the performance of ATR algorithms. For example, the statistic information of the image pixels of the SAR image will play an important role in the baseline ATR algorithms using conditional Gaussian method. And the patterns of the SAR image may have greater effects on the template matching ATR algorithm. Therefore, a number of image distance metrics will be used in the platform: Energy, Statistic Information, Pattern and other Features. We have already established three baseline ATR algorithms. The list can be expanded if some other significant ATR algorithms with sufficient implementation information would be available. The standard ATR summary performance measures [38] such as: **Detection Probability** (P_{det})**, Probability of False Alarm** (P_{fa})**, Identification Probability** (P_{id}), and **Correct Label Probability** (P_{cl})**,** etc. will be used to compare the performance of the ATR algorithms under various sensor OC's. At the same time, the SAR images generated under different sensor OC's are compared with the combinational scores using the distance metrics. Some correlation between the scores from these two scoring systems can be established for all the SAR image based ATR algorithms. We believe this SAR ATR parametric experimental platform can greatly aid the study of effects of SAR sensor OC's on the performance of SAR image based ATR algorithms.

| SAR Data Simulation under Sensor OC's: Depression angles, Radar frequencies, Polarization, Squint angle, Stripmap, spot

┌─────────────────┐
│ Simulation
│ Kernel: Xpatch
└─────────────────┘ |

SAR Data Simulation under Sensor OC's: Depression angles, Radar frequencies, Polarization, Squint angle, Stripmap, spot

Simulation Kernel: Xpatch

Raw Radar Range Profile data

Baseline ATR Algorithms: Current implemented template matching, Lincoln Lab. ATR and Conditional Gaussian. The list is expanding.

Baseline ATR algorithms: Matlab

Confusion Matrices

Standard ATR Performance Evaluation Measurements: P_det, P_s, P_fa, P_id and P_cl.

ATR Performance Scorring System: Matlab

SAR Imaging Algorithms Implementation: Matlab

SAR Image Formation Algorithms under Sensor OC's: Stripmap, Spot, Synthetic aperture Length, Single look, Multiple looks, SAR image enhancement methods, Noise

SAR Images

Image Distance Metric Evaluation: Matlab

SAR Image Distance Metrics: Energy, Statistic Information, Pattern and Features

Distance Metrics

Distance Metric Scorring System: Matlab

Combinational image distance scores

2.SAR ATR Parametric Experimental Platform

94

Chapter 4
Conclusion

In this document, we first provided a brief introduction to the SAR sensor parameters and their functions in the SAR image formation algorithms. We have also discussed various assumptions and approximations made inside the SAR image formation algorithms. In this study, we have performed a complete literature survey on the prior works in SAR ATR parametric study. We concluded that though there were some studies on the SAR parameters and their behavior in the SAR image formation algorithms. Little has been done towards the ATR algorithm performance. The one of the most important reasons for the lack of study in this area is the lack of proper SAR image data with a complete spectrum of the sensor OC's variations. Also in the course of study, we found there were no agreeable baseline ATR algorithms for the ATR performance evaluation study. In order to establish a set of baseline ATR algorithms, we discovered three existing ATR algorithms with different target classification techniques. In this project, we have implemented, verified and optimized the ATR algorithms using Matlab with the data from MSTAR database. The established baseline ATR algorithms are documented in this report for future ATR performance evaluation. In the searching for the available real SAR image data with variations in sensor OC's, we found, as expected, nothing significant. Due to the lack of real experimental data, it leads us to explore the possibility of generate simulated SAR data with various assumed sensor OC's. We have set up an ITAR facility at our location for this purpose with the investment from Wright State University. The facility has the capability of generating SAR range profile or image data under various sensor OC's using Xpatch. The initial data simulation is planned in this study and currently the first phase of data simulation is being carried out. The first phase of data simulation is intended to cover sensor OC's in depression angle, frequency, polarization, noise, synthetic aperture length, and SAR image formation algorithms. In carrying out data simulation, we found that the simulation on a complex target under one set of sensor OC took very long time (hundreds hours) to run. And we need multiple set of sensor OC's to evaluate any ATR algorithm. Therefore, the data simulation is an on–going process and the results will be reported to Air force engineers in the future (this part is not a task in the original proposal anyway). To point out the roadmap for the future study in this area, we also developed a SAR ATR parametric experimental platform which has all the components for conducting SAR ATR parametric study. We conducted a preliminary experiment for the depression angle variation on the baseline ATR algorithms using the only real SAR data available from MSTAR database. The preliminary experiment is to illustrate the evaluation process. As we expected, the experiment showed that all the baseline ATR algorithms failed to yield usable confusion matrix at such large depression angle variations. As conclusion, we have fulfilled the objectives of this study only to discover more research needs to be done for the future studies in this area.

Appendix A
References

[1] R. Abrahamsson, J. Li, P. Stocia, and G. Thordason, "Sensitivity of two Autofocus Algorithms to Spatially Variant Phase Errors." In E.G. Zelnio, editor, Algorithms for Synthetic Aperture Radar Imagery VIII, Proc. Of SPIE, volume 4382, pages 29-40, 2001.

[2] M.R. Allen, "An Efficient Approach to Physics Based FOPEN SAR ATD/R." In E.G. Zelnio, editor, Algorithms for Synthetic Aperture Radar Imagery III, Proc. Of SPIE, volume 2757, pages 163-172, 1996.

[3] S. Ayasli, and L. Bessette, "UHF and VHF SAR Phenomenology." Proceedings of the PIERS Workshop on Advances in Radar Methods 1998. 45-47, 1998.

[4] C. Blasband, and J. Jafolla, "RadBase^{TM}: A Physics-Based Radar Database Generation Toolkit." Internet:http://www.surfaceoptics.com/data/pdf/RadBase2_tech_paper.PDF, 2001.

[5] M. Bryant, "Matlab code for the implementation of template matching SAR ATR algorithm using images from MSTAR data collection," private communication, 2002.

[6] M. Burl, G.J. Owirka, and L.M. Novak, "Texture Discrimination in Synthetic Aperture Radar Imagery." R.R. Conference Record. Twenty-Third Asilomar Conference on Signals, Systems, and Computers (IEEE Cat. No. 89-CH2836-5), volume 1, pages 399-404, 1989.

[7] L. Carin, N. Geng, M. McClure, J. Sichina, and L. Nguyen, "Ultra–wide–Band Synthetic Aperture Radar for Mine–Field Detection," IEEE Antennas and Propagation Magazine, Vol. 41, No. 1, 18-33, Feb. 1999.

[8] W. Carrara, S. Tummala, and R. Goodman, "Motion Compensation Algorithms for Widebeam Stripmap SAR," SPIE Vol. 2487, 13-23, 1995.

[9] S. Dai and S. Huang, "A Comparison of Algorithms for Squint Side–looking Strip Imaging mode SAR," SPIE Vol. 3070, 356-363, 1997.

[10] P.H. Eichel, D.C. Ghigla, and C.V. Jakowatz, "Speckle Processing For Synthetic Aperture Radar Phase Correction." Optics Letters, 14(1):1-3, Jan. 1989.

[11] G. Fornaro, "Trajectory Deviations in Airborne SAR: Analysis and Compensation." IEEE Transactions on Aerospace and Electronic systems, 35(3): 997-1009, July 1999.

[12] G. Farnaro, E. Sansosti, R. Lanari, and M. Tesauro, "Role of Processing Geometry in SAR Raw Data Focusing," IEEE Transactions on Aerospace and Electronics Systems, Vol. 38, No. 2, 441-453, Apr. 2002.

[13] D. S. Garmatyuk and R. M. Narayanan, "SAR Imaging Using a Coherent Ultrawideband Random Noise Radar," SPIE Conf. on Radar Processing, Technology, and Applications IV, SPIE Proc. Vol. 3810, 223-230, July 1999.

[14] N. Geng, M. Ressler, and L. Carin, "Wide-band VHF Scattering from Trihedral Reflector Situated above a Lossy Dispersive Halfspace." IEEE Transactions on Geoscience and Remote Sensing, 37(5): 2609-2617, Sept. 1999.

[15] M. Gerry, L. Potter, I. Gupta, and A. Merwe, "A Parametric Model for Synthetic Aperture Radar Measurement." IEEE Transactions on Antenna Propagation, vol. 47, 1179-18, July 1999.

[16] E. Hanle, "Polarimetric Antenna Influences with Synthetic Aperture Radar Off-boardside."

Appendix A **References**

EURSAR'96 European Conference on Synthetic Aperture Radar, pages 121-124, 1996.

[17] L. Happ, F. Le, M. Ressler, and K. Kappra, "Low-Frequency ultra-wideband Synthetic Aperture Radar: frequency subbandind for targets obscured by the Ground." In E.G. Zelnio, editor, Algorithms for Synthetic Aperture Radar Imagery III, Proc. Of SPIE, volume 2747, pages 194-201, 1996.

[18] K. Ikeuchi, M.D. Wheeler, T. Yamazaki, and T. Shakunaga, "Model Based SAR AR System." In E.G. Zelnio, editor, Algorithms for Synthetic Aperture Radar Imagery III, Proc. Of SPIE, volume 2757, pages 376-387, 1996.

[19] T.Isernia, V. Pascazio, R. Pierri, and G. Schirinzi, "Synthetic Aperture Radar Imaging with Corrupted Data." IEE Proceedings on Radar, Sonar, and Navigation, 143(4): 268-274, Aug. 1996.

[20] R. James and C. Hendrickson, "Efficacy of Frequency on Detecting Targets in Foliage using Incoherent Change Detection." In E.G. Zelnio, editor, Algorithms for Synthetic Aperture Radar Imagery, Proc. Of SPIE, volume 2236, pages 220-229, 1994.

[21] L.M. Kaplan, R. Murenzi, E. Asika, and K. Namuduri, "Effect of signal to clutter Ratio on Template Based ATR." In E.G. Zelnio, editor, Algorithms for Synthetic Aperture Radar Imagery V, Proc. Of SPIE, volume 3370, pages 408-419, 1998.

[22] L.M. Kaplan, "Analysis of Multiplicative Speckle Models for template based SAR ATR." IEEE Transactions on Aerospace and Electronic systems, 37(4): 1421-1431, Oct. 2001.

[23] B. Kapoor, A. Banerjee, G. A. Tsihrintzis, and N. Nandhakumar, "UWB Radar Detection of Targets in Foliage Using Alpha–Stable Clutter Models," IEEE Transactions of Aerospace and Electronic Systems, Vol. 35, No. 3, 819-834.

[24] E.R. Keydel, and S.W. Lee, "Signature Prediction For model-Based Automatic Target Recognition." In E.G. Zelnio, editor, Algorithms for Synthetic Aperture Radar Imagery III, Proc. Of SPIE, volume 2757, pages 306-317, 1996.

[25] G. Q. Liu, S.J. Huang, A Torre, and F. Rubertone, "Multi-Look Polarimetric SAR Target Detection Performance Analysis and Frequency Selection." 1996 CIE International Conference on Radar Proceedings, pages 305-308, 1996.

[26] G. Liu, H. Xiong, and S. Huang. "Multi-look Polarimetric Processing Algorithms and their Applications in SAR Target Detection." EURSAR'98 European Conference on Synthetic Aperture Radar: Proceedings of EURSAR'98: European Conference on Synthetic Aperture Radar. Pages 431-434, 1998

[27] J. Mittermayer, A. Moreira, and O. Loffeld, "Spotlight SAR Data Processing Using the Frequency Scalling Algorithm," IEEE Transactions on Geoscience and Remote Sensing, 37(5): 2198–2214, Sep. 1999.

[28] J.C. Mossing, and T.D. Ross, "An Evaluation of SAR ATR Algorithm performance Sensitivity to MSTAR Extended Operating Conditions." In E.G. Zelnio, editor, Algorithms for Synthetic Aperture Radar Imagery V, Proc. Of SPIE, volume 3370, pages 554-565, 1998.

[29] L.M. Novak, M.C. Burl, and W.W. Irving, "Optimal Polarimetric Processing for Enhanced Target Detection." IEEE Transactions on Aerospace and Electronic systems, 29(1): 234-243, Jan. 1993.

[30] L.M. Novak, S.D. Halverson, G.J. Owirka, and M. Hiet. "Effects of Polarization and Resolution on the Performance of a SAR Automatic Target Recognition System." The

Lincoln Laboratory Journal, 6(1): 49-67, 1995.

[31] L.M. Novak, G.J. Owirka, and A.L. Weaver, "Automatic target Recognition Using Enhanced Resolution SAR Data." IEEE Transactions on Aerospace and Electronic systems, 35(1): 157-174, Jan. 1999.

[32] Leslie Novak, "Effects of Various Image Enhancement Techniques on FOPEN Data," Proceedings of the 2001 IEEE Radar Conference (Cat. No.01CH37200), 87-92, 2001.

[33] J.A. O'Sullvan, M.D. DeVore, V. Kedia, and M.I. Miller, "SAR ATR Performance Using conditionally Gaussian Model." IEEE Transactions on Aerospace and Electronic systems, 37(1): 91-106, Jan. 2001.

[34] Kenneth Ranny, Hiralal Khatri, and Lam Nguyen,"An Alternative Procedure for Detecting Stationary Targets with Ultra–Wideband Foliage Penetration Radar," In E.G. Zelnio, editor, Algorithms for Synthetic Aperture Radar Imagery VIII, Proc. Of SPIE, volume 4382, pages 195-204, 2001.

[35] R. Rau and J. H. McClellan, "Analytic Models and Post Processing Techniques for UWB SAR," IEEE Transactions on Aerospace and Electronic Systems, Vol. 36, No.4, 1058-1074, Oct. 2000.

[36] T.D. Ross, J.J. Bradley, L.J. Hudson, and M.P. O'Conner, "SAR ATR-So What's the Problem?" In E.G. Zelnio, editor, Algorithms for Synthetic Aperture Radar Imagery VI, Proc. Of SPIE, volume 3721, pages 566-573, 1999.

[37] T.D. Ross, S.W. Worrel, V. Velten, J. Mossing, and M. Bryant, "Standard SAR ATR Evaluation Experiments using the MSATR Public release Data Set." In E.G. Zelnio, editor, Algorithms for Synthetic Aperture Radar Imagery V, Proc. Of SPIE, volume 3370, pages 566-573, 1998.

[38] T.D. Ross, L. Westerkamp, R. Dilsalor, and J. Mossing, "Performance Measures for Summarizing Confusion Matrices — The AFRL COMPHSE Approach." In E.G. Zelnio, editor, Algorithms for Synthetic Aperture Radar Imagery, Proc. Of SPIE, volume 4727, 4727-4731, April 2002.

[39] T. Ryan, and B. Egaas, "SAR Transform indexing with Hierarchical Distance Transform." In E.G. Zelnio, editor, Algorithms for Synthetic Aperture Radar Imagery, Proc. Of SPIE, volume 2757, pages 243-252, 1996.

[40] F. Sadjadi, "Improved Classification using Optimum Polarimetric SAR Signatures." IEEE Transactions on Aerospace and Electronic systems, 38(1): 38-49, Jan. 2002.

[41] M. Sciotti, D. Pastina, and P. Lombardo, "Polarimetric Detection of extended Targets for Ship Detection in SAR Images." IGARSS 2001. Scanning the Present and Resolving the Future Proceedings. IEEE 2001 International Geoscience and Remote Sensing Symposium (Cat. No. 01CH37217), volume 7, pages 3132-3134, 2001.

[42] J. Sichina, and L. Nguyen, "Using Models and Measurements to Describe Ultra Wide-band radar Scattering Phenomena." In E.G. Zelnio, editor, Algorithms for Synthetic Aperture Radar Imagery, Proc. Of SPIE, volume 4053, pages 220-228, 2001.

[43] W. Smith, D. Filiberti, A. Bennett, and A. Currie, "Calibration of Polarimetric SAR and Sensitivity to Calibration Error." In E.G. Zelnio, editor, Algorithms for Synthetic Aperture Radar Imagery VIII, Proc. Of SPIE, volume 4382, pages 264-275, 2001.

[44] M. Soumekh, "Synthetic Aperture Radar Signal Processing with MATLAB Algorithms."

New York: John Wiley & Sons, inc., 1999.

[45] M. Soumekh, D. Nobles, M. Wicks, and G. Genello, "Signal Processing of Wide Bandwidth and Wide Beamwidth P-3 SAR Data." IEEE Transactions on Aerospace and Electronic systems, 37(4): 1122-1141, Oct. 2001.

[46] G. W. Stimson, "Introduction to Airborne Radar," 2nd edition, SciTech Publishing, Inc. Mendham, Ner Jersey, 1998.

[47] A. Sullivan, R. Damarla, N., Geng, Y. Dong, and L. Carin, "Ultrawide–Band Synthetic Aperture Radar for Detection of Unexploded Ordnance: Modeling and Measurements," IEEE Transactions on Antennas and Propagation, Vol. 48, No. 9, Sep. 2000.

[48] X. Sun, T.S. Yeo, C. Zhang, Y. Lu, and P.S. Kooi, "Time-Varying Step-Transform algorithm For High Squint SAR Imaging." IEEE Transactions on Geoscience and Remote Sensing, 37(6): 2668-2677, Nov. 1999.

[49] Toups M.F., Bessette L.A., and Binder B.T., "Foilage Penetration data Collections and Investigations Utilizing the P-3 UWB SAR." In E.G. Zelnio, editor, Algorithms for Synthetic Aperture Radar Imagery III, Proc. Of SPIE, volume 2757, pages 136-144, 1996.

[50] J. Volakis, "XPATCH: A High Frequency Electromagnetic Scattering Prediction Code and Environment for Complex Three Dimensional Objects." IEEE Antennas and Propagation Magazine, 36(1): 65-69, 1994.

[51] H. Xiong, and S. Huang, "Multi-Look Polarimetric Processing Algorithms and Their Applications in SAR Target Detection." EURSAR'98 European Conference on Synthetic Aperture Radar, pages 431-434, 1996.

[52] X. Xu, and R.M. Narayanan, "FOPEN SAR Imaging Using UWB Step Frequency and Random Noise Waveforms." IEEE Transactions on Aerospace and Electronic systems, 37(4): 1287-1299, Oct. 2001.

[53] X. Xu, and R.M. Narayanan, "Range Sidelobe Suppression Technique for Coherent Ultra wide-band Random Noise Radar Imaging" IEEE Transactions on Antennas and Propagation, 49(12): 1836-1842, Dec. 2001.

[54] D.E. Wahl, P.H. Eichel, D.C. Ghiglia, and C.V. Jakowatz, "Phase Gradient Autofocus-A Robust tool for high Resolution SAR Phase Correction." IEEE Transactions on Aerospace and Electronic systems, 30(3): 827-834, July. 1994.

[55] D. W. Warner, D. C. Ghiglia, A. FitzGerrell, and J. Beaver, "Two–Dimensional Phase Gradient Autofocus," In Image Reconstruction from Incomplete Data, M. A. Fiddy and R. P. Millane, Editor, Proc. of SPIE Vol. 4123, 162-173, 2000.

[56] J. Wissinger, R.Washburn, D. Morgan, C. Chong, N. Friedland, A. Nowicki, and R. Fung, "Search Algorithms for Model-based SAR ATR." In E.G. Zelnio, editor, Algorithms for Synthetic Aperture Radar Imagery III, Proc. Of SPIE, volume 2757, pages 279-293, 1996.

[57] J. Wissinger, R. Ristroph, J. Diemunsch, W. Severson, and E. freudenthal, "MSTAR Extensible Search Engine and Model Based Toolkit." In E.G. Zelnio, editor, Algorithms for Synthetic Aperture Radar Imagery, Proc. Of SPIE, volume 3721, pages 554-570, 1999.

[58] S.W. Worrel, M. Bryant and S. Parker, "Class Separability Assessments and MSE Algorithm robustness." In E.G. Zelnio, editor, Algorithms for Synthetic Aperture Radar Imagery IV, Proc. Of SPIE, volume 3070, pages 294-304, 1997.

[59] Y. Yu, A. Torre, F. Xu, and S. Haung, "Optimal Frequencies and Polarizations for Radar

Detection of Targets." In E.G. Zelnio, editor, Algorithms for Synthetic Aperture Radar Imagery II, Proc. Of SPIE, volume 2567, pages 21-30, 1995.

Appendix B
The Sources Consulted But Not
Used

[1] G. Benitz, "High-Definition Imaging." In E.G. Zelnio, editor, Algorithms for Synthetic Aperture Radar Imagery, Proc. Of SPIE, volume 2230, pages 106-119, 1994.

[2] M. Chiang, R. Moses, L. Potter, "Model Based Classification of Radar Images." IEEE Transactions on Information Theory, 46(5):1842-1854, Aug. 2001.

[3] K. Conradsen, A. Nielsen, J. Schou, and H. Skriver, "Change Detection in Polarimetric SAR Data and the Complex Wishart Distribution." IGARSS 2001. Scanning the Present and Resolving the Future Proceedings. IEEE 2001 International Geoscience and Remote Sensing Symposium (Cat. No.01CH37217), volume 6, pages 2628-30, 2001.

[4] H.D. Griffiths, and P. Mancini, "Extraction of Textural Information in Polarimetric SAR." IEE Seminar on Texture Analysis in Radar and Sonar, volume 7, pages 7/1-7/7, 1996.

[5] S. Jin-Ping, M. Shi-Yi, L. Zhong-Kan, and H. Wen, "Using Frequency Scaling Approach to Process Squint Spotlight SAR Data" In E.G. Zelnio, editor, Algorithms for Synthetic Aperture Radar Imagery VIII, Proc. Of SPIE, volume 4382, pages 22-28, 2001.

[6] R. Lanari, and G. Fornaro, "A Short Discussion on the exact Compensation of the SAR Range Dependent Range Cell Migration Effect." IEEE Transactions on Geoscience and Remote Sensing, 35(6):1446-1452, Nov. 1997.

[7] E. Larsson, J. Li, P. Stochia, G. Liu, and R. Williams, "Spectral Estimation Of Gapped Data and SAR Imaging with Angular Diversity." In E.G. Zelnio, editor, Algorithms for Synthetic Aperture Radar Imagery VII, Proc. Of SPIE, volume 4382, pages 60-7, 2001.

[8] J. Lee, K. Hoppel, S.A. Mango, and A.R. Miller, "Intensity and Phase Statistics of Multi-look Polarimetric SAR Imagery." IGARSS'93. 1993 International Geoscience and Remote Sensing Symposium (IGARSS'93) Better Understanding of Earth Environment (Cat. No.93CH3294-6), volume 2, pages 813-16, 1993.

[9] J. Lee, M. Gieunes, and E. Potter, "Quantitative Comparison of Classification Capability: Fully Polarimetric Versus Dual and Single Polarization SAR." IEEE transactions on Geoscience and Remote Sensing, 39(11):2343-2350, Nov. 2001.

[10] J. Li, G. Liu, K. Zhang, and P. Stoica, "Polarimetric SAR Target Feature Extraction and Image Formation Via a Semi-Parametric Method." In E.G. Zelnio, editor, Algorithms for Synthetic Aperture Radar Imagery, Proc. Of SPIE, volume 4053, pages 164-175, 2000.

[11] Z. S.Liu, and J.Li, "Feature Extraction of SAR Targets Consisting of Trihedral and Dihedral Corner Reflectors." IEE Proceedings on Radar, Sonar, and Navigation, 145(3):161-171, June 1998.

[12] A. Marinelli, L. Kaplan, and N. Nasrabad, "SAR ATR Using Learning Vector Quantization." IS&T/SPIE Conference on Applications of Artificial Neural Networks in Image Processing IV, Proc. Of SPIE, volume 3647, pages14-25, 1999.

[13] D.H. Nguyen, J.H. Kay, B.J. Orchard, G.K. Bentiz, and R.H. Whiting, "Improving HRR ATR Performance at Low SNR by Multi-Look Adaptive Weighting." In E.G. Zelnio, editor,

Algorithms for Synthetic Aperture Radar Imagery, Proc. Of SPIE, volume 4379, pages 216-228, 2001.

[14] L. Potter, and R. Mosses, "Attributed Scattering Centers for SAR ATR." IEEE Transactions on Imaging Processing, 6(1):79-91, Jan, 1997.

[15] P. Runkle, L. Nguyen, J. McClellan, and L. Carin, "Multi-Aspect Target Detection for SAR Imagery Using Hidden Markov Models." IEEE Transactions on Geoscience and Remote Sensing, 39(1):46-55, Jan. 2001.

[16] V. Santalla, Y.M.M. Antar, "Comparison Between Different Polarimetric Measurement Schemes." IEEE Transactions on Geoscience and Remote Sensing, 40(5):1007-1017, May 2002.

[17] W. Smith, D. Filiberti, A. Bennett, and A. Currie, "Calibration of Polarimetric SAR and Sensitivity to Calibration Error." In E.G. Zelnio, editor, Algorithms for Synthetic Aperture Radar Imagery VIII, Proc. Of SPIE, volume 4382, pages 264-275, 2001.

[18] D. Trizan, C. Bachman, M. Seletten, N. Allen, J. Toporkov, and R. Harris, "Projection Pursuit Classification of Multiband Polarimetric SAR Land Images." IEEE Transactions on Geoscience and Remote Sensing, 39(11):2380-2385, Nov. 2001.

[19] Vincent Velten, "Geometric Invariance for Synthetic Aperture Radar (SAR) Images." Internet:http://www.mbvlab.wpafb.af.mil/papers/Gifsars/geoinv.htm.